Challenge Journal of STRUCTURAL MECHANICS

Vol.2 No.4 (2016)

ISSN 2149-8024

TULPAR ACADEMIC PUBLISHING

Challenge Journal of Structural Mechanics

E-mail: *cjsmec@challengejournal.com*

Web page: *cjsmec.challengejournal.com*

TULPAR Academic Publishing
www.tulparpublishing.com

Challenge Journal of Structural Mechanics

CONTENTS

TULPAR ACADEMIC PUBLISHING

Challenge Journal of Structural Mechanics

Assessment of aerodynamic response of the Nissibi cable-stayed bridge using three-dimensional computational fluid dynamics

Savaş Erdem *, İrem Yağmuroğlu, Khalid Saifullah

Department of Civil Engineering, İstanbul University, 34320 Istanbul, Turkey

ABSTRACT

Aerodynamic behavior has the greatest impact on long-span bridges and is the most important factor in the design of cable stayed bridges, which should not be overlooked. CFD (Computational Fluid Dynamics) is the most widely used technique, among bridge engineers, to predict wind speed, direction and vortex-shedding form before conducting wind tunnel tests. In this study, a bi-directional CFD analysis with the wind flow parallel and perpendicular to Nissibi Bridge's, which has a main span of 400 m and claimed the spot of Turkey's 3rd largest bridge, deck cross-section has been performed by approximate modelling of the bridge and the surrounding structures. The study is done by using CFD++ software/computer program. The results showed that the effect of wind acting on *x* direction of impact with 30 m/s has caused turbulence and vortex on conjugation area of the tower and it is observed that the upside down Y shape of the tower breaks down the balance of wind flow. However, bridge deck is not exposed to serious amount of vortex influence due to the wind on *y* direction. In addition, the analysis revealed that maximum pressure distribution occurred on vertical surface of the tower and it increases in direct proportion to the height of the tower.

ARTICLE INFO

Article history:
Received 8 November 2016
Accepted 17 December 2016

Keywords:
Aerodynamic behaviour
CFD
Cable-stayed bridge
Wind

1. Introduction

Nissibi Bridge, a part of Adiyaman-Kahta-Siverek-Diyarbakır highway/motorway, got drowned due to the lake formed as a result of the construction of Ataturk Dam which came into operation in 1992, thus resulting in the disconnection of highway link between Adıyaman and Diyarbakır. At that time, the government divided the highway into two as a consequence of which the distance between Adıyaman and Diyarbakır increased by 150 km. To rectify this problem, construction of a new bridge between Kahta and Siverek came into consideration. The materialization of the project in question started in 2012 with the commencement of work on cable stayed Nissibi Bridge that was later inaugurated in the first half of 2015.

The cable stayed bridge has a main span of 400 m and claimed the spot of Turkey's 3rd largest bridge. Due to the complications and cost involved in positioning the bridge pier inside the reservoir/lake of the dam, it was deemed necessary to cross the reservoir/lake with a long span bridge. All types of bridges are subjected to wind effects but the long span bridges are the ones which are more sensitive to dynamic responses/effects as compared to others. Dynamic wind load/force, despite of not being very influential from loading viewpoint, is important due to the vibrations it brings about. Tacoma Narrows Bridge is the most important example of aerodynamic properties' influence/effect on the design. The bridge got demolished due to the aeroelastic flutter arising from the wind flowing at a velocity of only 64 m/s. This incident brought to light the importance of aerodynamic effects over bridge (Arioli and Gazzalo, 2013).

Bridge design should be conducted in such a way that it would not encounter any kind of instability and sudden wind impulses/excitations would remain within the acceptable limits. An example of it is Messina Strait Bridge, which would have overtaken Akashi Kaikyo

* *Corresponding author*. Tel.: +90-212-4737070 ; Fax: +90-212-4737180 ; E-mail address: savas.erdem@istanbul.edu.tr (S. Erdem)
ISSN: 2149-8024 / DOI: http://dx.doi.org/10.20528/cjsmec.2016.12.037

Bridge as the longest suspension bridge, with the central span length of 60% more than the Akashi Kaikyo Bridge's. To check the aerodynamic design properties of the bridge, a comprehensive study involving wind tunnel test simulations has been carried out (Diana et al., 2013).

Aerodynamic behavior has the greatest impact on long-span bridges and is the most important factor in the design of cable stayed bridges, which should not be overlooked. In previous studies, analysis of bridges to wind-induced motions were performed by various researchers (Ge and Tanaka, 2000; Xu et al., 2004; Yongle et al., 2004; Matsumoto et al., 2001 and Ren et al., 2005). However, previous studies have been limited to analysing two dimensional sections only, and three dimensional analyses of the bridges have not yet been studies.

All these studies underline that the high level of flexibility associated with the cable stayed bridges make them more sensitive to wind flow as compared to other structures. The reasons for this susceptibility/sensitivity are:

- Aerodynamic instability; incompatibility of dynamic effect with static effect or vibrations in the bridge deck arising from the dynamic effects may be sufficient to cause destruction of the bridge.
- Buffeting; the effect arising from the turbulences generated by the wind flow. The bridge deck, when subjected to these turbulences for a long time, may experience fatigue effect depending upon the movement of the deck.
- Vortex-shedding realization results in periodic vortex vibrations; bridge deck may experience forced vibrations (ICE Manual of Bridge Engineering, 2008).

Investigating wind-structure interaction with wind tunnel tests is a quite compelling and comprehensive engineering problem/study. With the developments in wind engineering after the tragedy of Tacoma Narrows Bridge, wind tunnel testing has been made compulsory for the design of long span bridges (Diana et al., 2013). However, wind tunnel test calculations become very difficult/complex due to different profiles/cross-sections involved in the test and are very costly, indeed. Due to the aforementioned reasons, Numerical simulations became the center of attention for aerodynamic and aeroelastic analyses. CFD (Computational Fluid Dynamics) is a computer modeling technique to simulate fluids flow. CFD is the most widely used technique, among bridge engineers, to predict wind speed, direction and vortex-shedding form before conducting wind tunnel tests. 2D numerical simulations, related to aerodynamic of bridge deck, performed over Great Belt East Bridge in Denmark showed very close results to the ones obtained from wind tunnel tests and progress was recorded in the vortex formation (Bruno and Chris, 2003). In a study, on U-shaped Bridge, involving 2D and 3D CFD models, a comparison of results of 2D and 3D CFD with the wind tunnel test results showed that 3D CFD simulations presented more close results to wind tunnel test results as compared to 2D CFD simulations. For 3D turbulent incompressible viscous flow, 3D numerical methods alongside Detached-Eddy simulations have been effectively used for bridges (Bai et al., 2010).

In this study, a bi-directional CFD analysis with the wind flow parallel and perpendicular to the bridge deck cross-section has been performed by approximate modeling of the bridge and the surrounding structures. The goal of the study is to determine the wind load effects on the bridge and its elements, by considering the wind flow characteristics of the region where the bridge is situated. The study is done by using CFD++ software/computer program. CFD++ is an advanced level general purpose computational fluid dynamics software, based on integrated element modeling, integrated physics and integrated calculation methodology, within advanced numerical discretization and solution system.

2. Methodology

2.1. Construction stages of the Nissibi Bridge

Nissibi Bridge is a single span bridge with the main central span of 400m and total span of 610m (Fig. 1). The height of each pylon is approximately one-fourth of the main span length i.e. 96.8 m and is in λ form/type. The cross-sections of pylons are in the form of reinforced concrete box sections. Despite having a self-weight much more than their steel counterparts, they support a variety of cable configurations. Box sections are preferred to provide safety against buckling with the minimum amount of material. Limestone type rock units related to Gaziantep formation, the idealized soil type which is observed from the surface, are generated/created. The bridge foundation has been designed as shallow foundation/spread footing to sit on the limestone formations at the base. For the static load case, the allowable bearing capacity of the soil has been calculated as 1000 kPa. The foundation of pylon is designed to have dimensions of 40m x 7.3m x 5m as shown in Fig. 2.

In cable-stayed bridges, straight cables radiating from the pylon are connected to the deck. In case of multiple cable arrangements the system can be fan type (i.e. cables radiating from the top) or harp type (i.e. cables are positioned parallel and are connected to pylon at different heights). A combination of these two types is often used, known as modified fan system, and has been used in Nissibi Bridge. Construction/erection of hollow pylon shaft, in the design, provides access for supervision or for new placements. The horizontal component of the forces in the cables will be withstood by the vertical and transverse prestressing of the concrete pylon.

The main span of Nissibi Bridge is made up of structural steel sections incorporating an orthotropic road deck while prestressed reinforced concrete box sections have been used in the edge spans. Box section has been preferred to provide a substantial amount of torsional stiffness. In box girders, top flange/cap not only serves as pavement deck but also transfer loads to vertical or inclined web elements. Moreover, box section bridges are known to be more resilient towards vibration effects as compared to classic bridges. In practice, single or multi cell box girders with rectangular or trapezoidal cross-sections may be employed. In the case of Nissibi Bridge, Trapezoidal box girders have been used (Fig. 3).

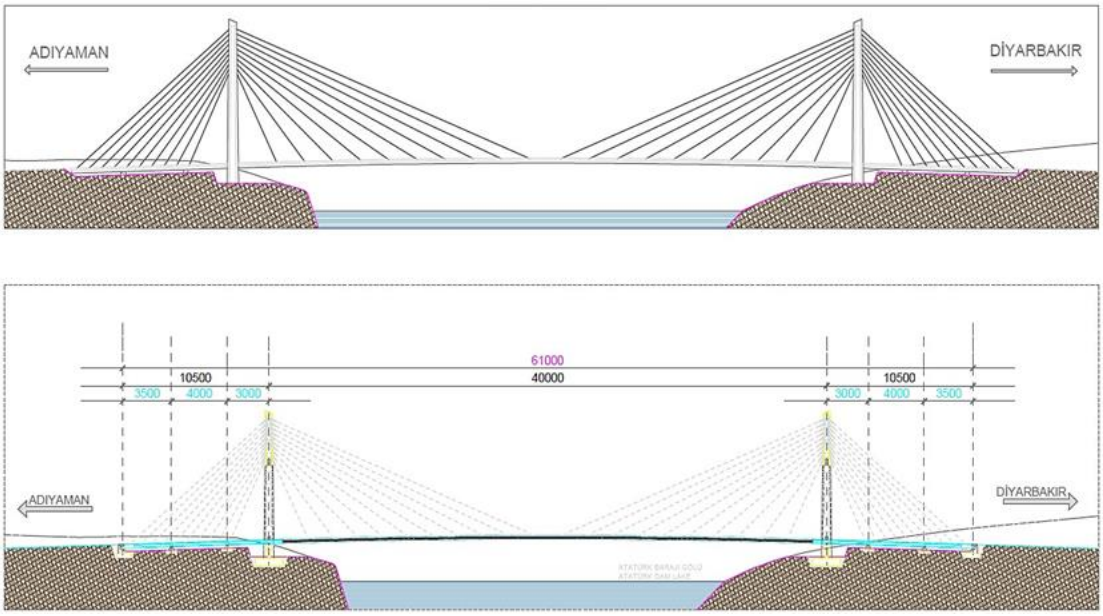

Fig. 1. General view of Nissibi cable-stayed bridge.

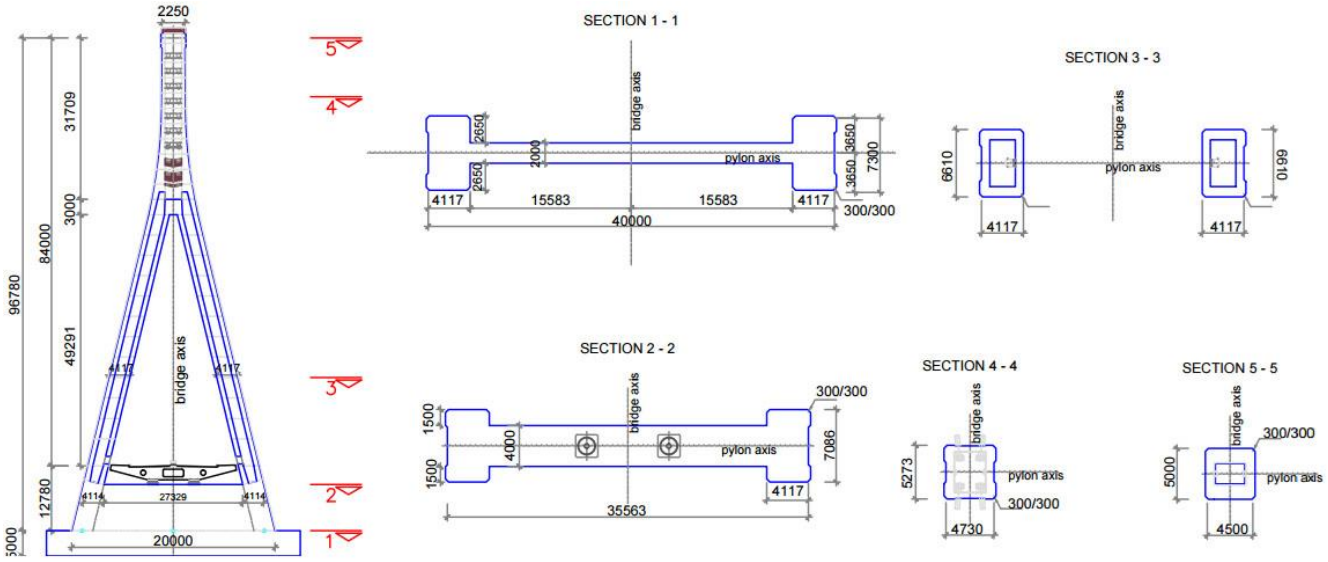

Fig. 2. Cross-section of the pylon.

2.2. Finite element modelling of Nissibi Bridge

Geometric modelling was done in CFD++ by using/importing 3D CAD DWG drawings (Fig. 4) of Nissibi Bridge. In the modelling, especially the main elements of the bridge have been taken into consideration. Due to Nissibi Bridge being cable stayed bridge with inclined cables, the effect of wind, on the structure, to which the cables are subjected, will not be critical and has been neglected.

To get CFD analysis results very close to the real, the surrounding structures with which the wind interacts before reaching the bridge model, have also been included in the analysis work. The modelling of surroundings of the bridge has been done on the basis of height difference from the topographic map/plan of Diyarbakır – Adıyaman cities.

2 grids are created for CFD analysis. An element grid consisting of 5 million hybrid (hexagonal and tetragonal) elements is built. Domain size of 2 km x 2 km is taken to provide atmospheric boundary conditions. The height is selected as 900 m, approximately 5 times the maximum height within the domain. Nissibi Bridge and surroundings are placed within the square domain with the required wind flow provided as bi-directional through surfaces/faces related to this square domain. In the flow domain, wall boundary conditions for bridge and the surrounding are modelled in different element sizes. Inside the domain, there are total 4 wall boundary conditions (as can be seen in Fig. 5); Bridge Pylons/Piers (in yellow), Pavement over bridge (in green), terrain over which the bridge rests (in red) and lake region around the bridge (in blue/cyan). The elements of the Nissibi Bridge have been modelled smaller, as compared to the surrounding elements, as can be seen in Table 1.

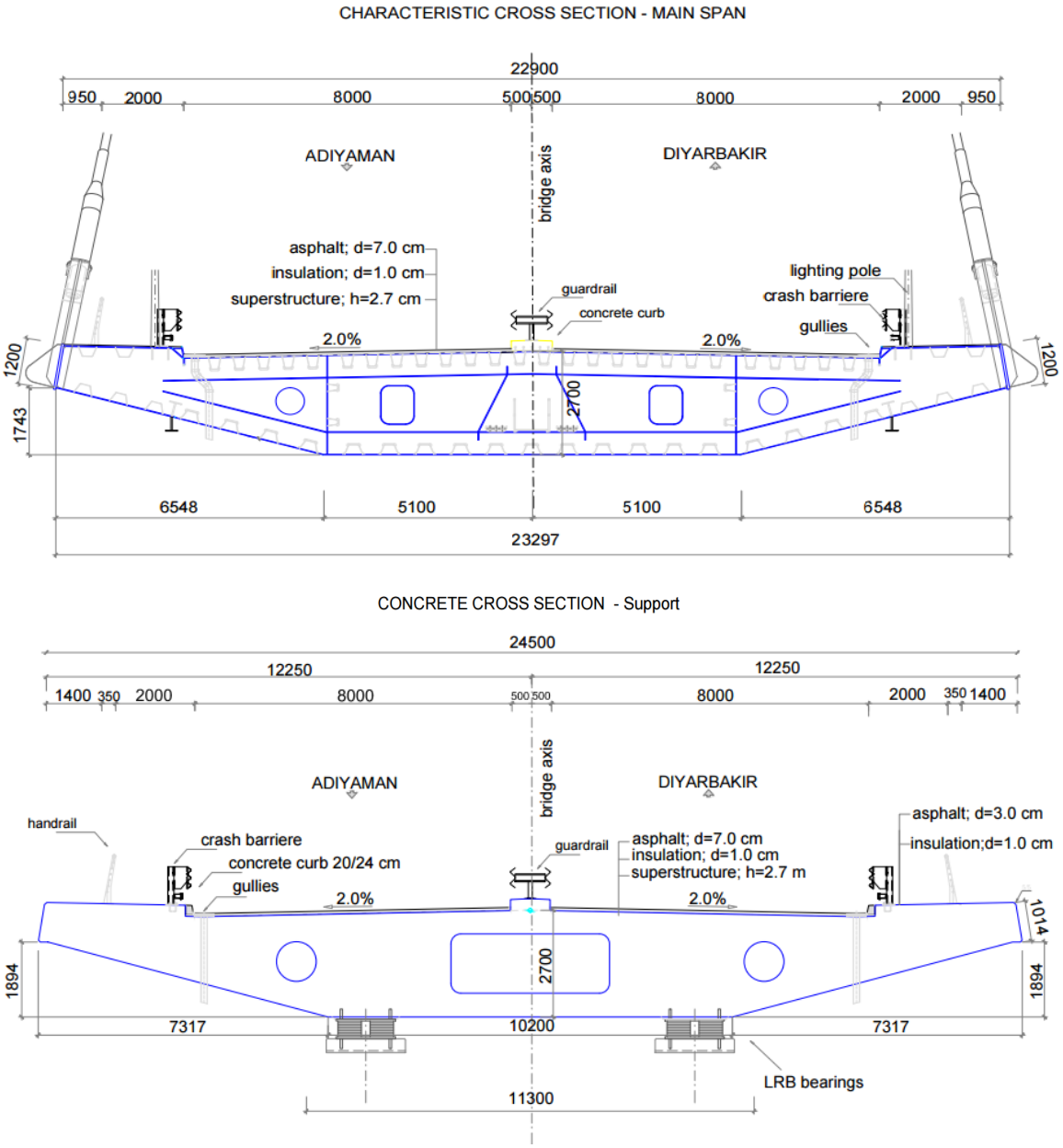

Fig. 3. Cross-section of the main span and support structural sections.

Fig. 4. The CAD view of the geometrical modelling.

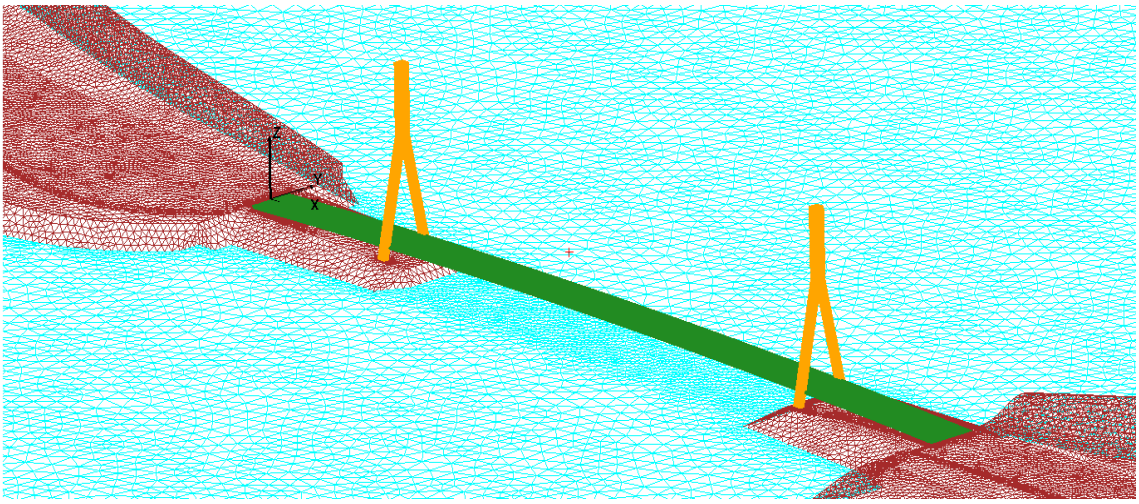

Fig. 5. The wall boundary conditions for the bridge and the surrounding.

Table 1. Maximum element size based on boundary conditions.

Boundary Surface/Face	Maximum Element Size (m)
Pylon/Tower	0.01
Deck	0.01
Terrain Area/Region	0.10
Lake Region	0.10

2.3. Flow characteristics

In the analysis conducted for wind coming parallel to the bridge, velocity of value 30 m/s, from navy-blue face/surface towards yellow face/surface (+x direction), is given. On the other hand, for the wind flow perpendicular to the bridge way, velocity of value 30 m/s, from pink face/surface towards green face/surface (+y direction), is considered (Fig. 6). 'Cubic k- ε' turbulence model has been used for turbulence modelling. Initial and end boundary condition values for k and ε values are automatically calculated, by software itself, while also considering geometric characteristic lengths.

3. Results and Discussion

Acting on x and y-direction (Figs. 7-8) of impact with effect of 30 m/s wind, maximum pressure distribution occurred on vertical surface of the tower and it increases in direct proportion to the height of the tower. This pressure, ruling on horizontal section, has caused large shear forces on the tower. Then, due to the stress on the pylon, where the pylon and bridge deck is fixed, a serious amount of pressure distribution is noticed.

However, the wind load on y direction did not create large amount of pressure on bridge deck (Fig. 9). There will be a sediment dislodging force on the bridge deck however the long distance of bridge and inclined hangered cables blocked it.

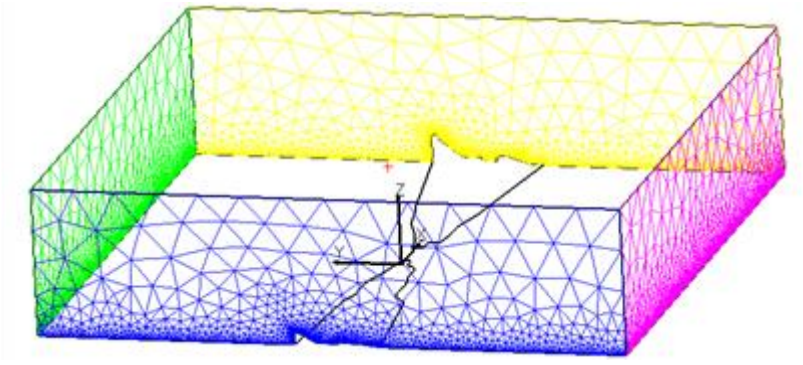

Fig. 6. Flow characteristics for the analysis.

The effect of wind acting on x direction of impact with 30 m/s has caused turbulence and vortex (Fig. 10) on conjugation area of the tower. In the figure, it is observed that the upside down Y shape of the tower breaks down the balance of wind flow. In the wind flow, when the vortexes arrived second pylon, linear flow was broken down. Thus, the second (right) pylon is exposed to more vortex oscillations compared to the first one (Fig. 11).

However, bridge deck is not exposed to serious amount of vortex influence due to the wind on x direction. Flow transistorizes that the wind created by crashing to the pylons did occur high pressure effect on the bridge deck.

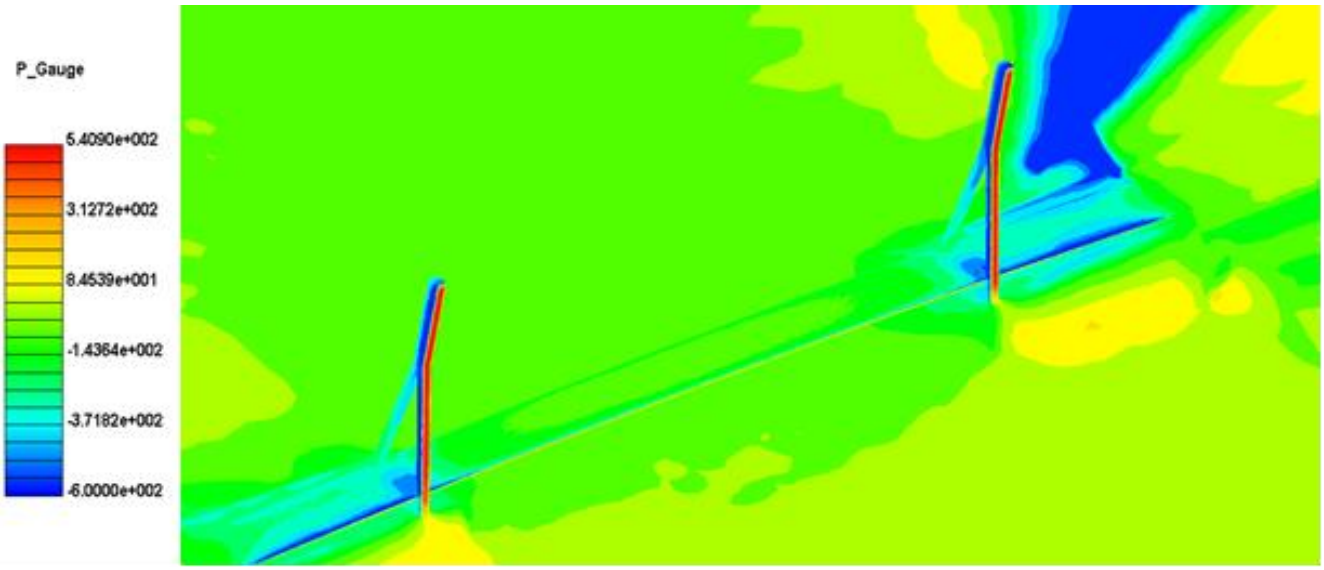

Fig. 7. Measured pressure results perpendicular to bridge.

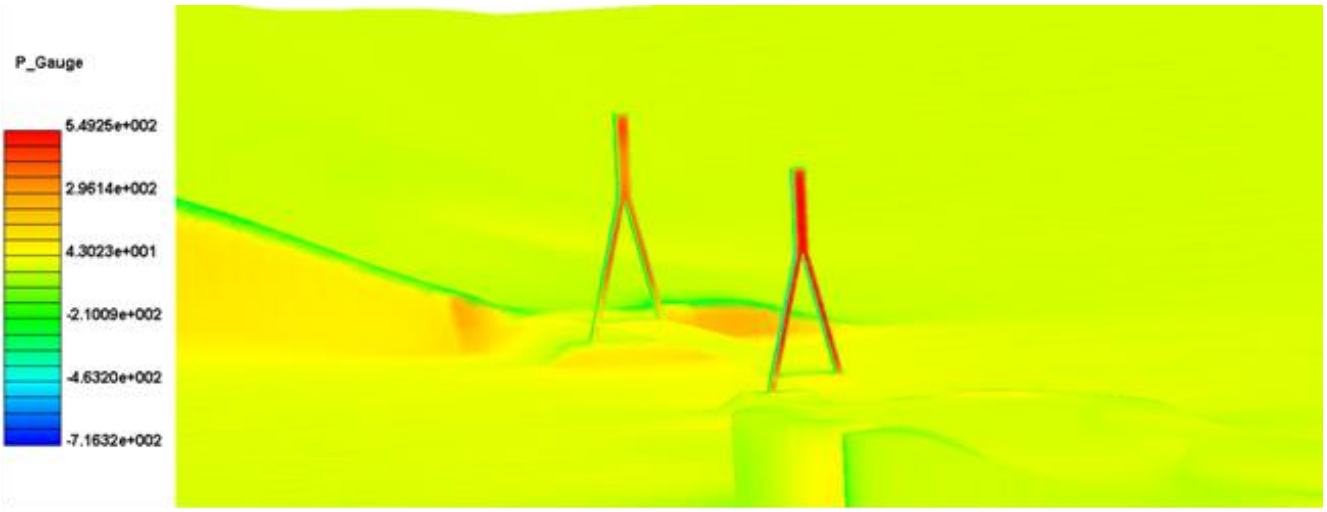

Fig. 8. Measured pressure results parallel to bridge.

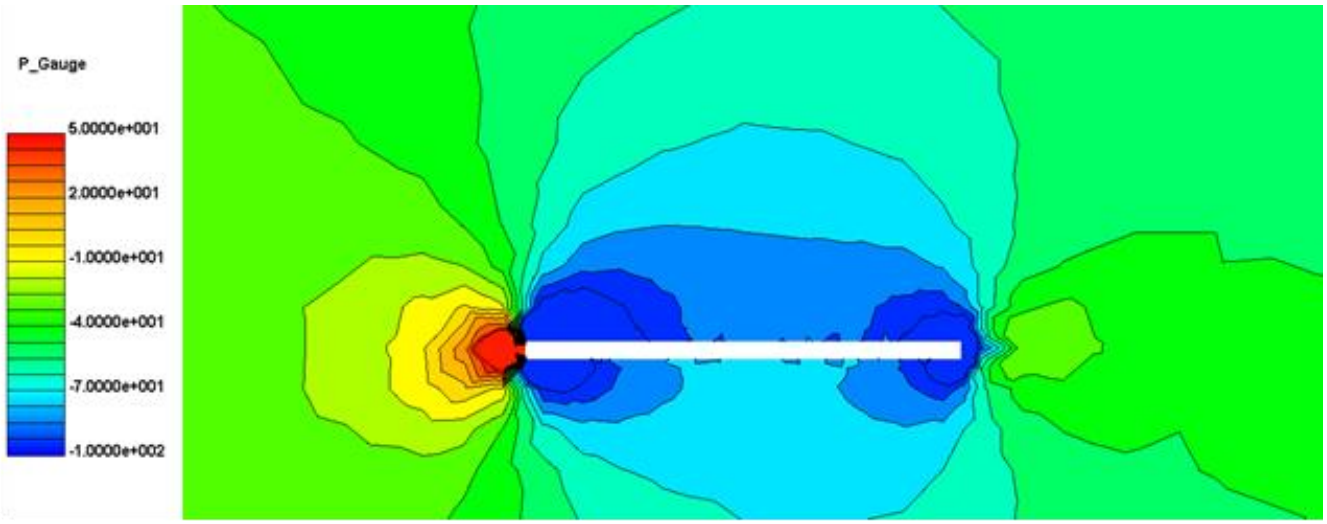

Fig. 9. Measured pressure results on the bridge deck in *y*-direction.

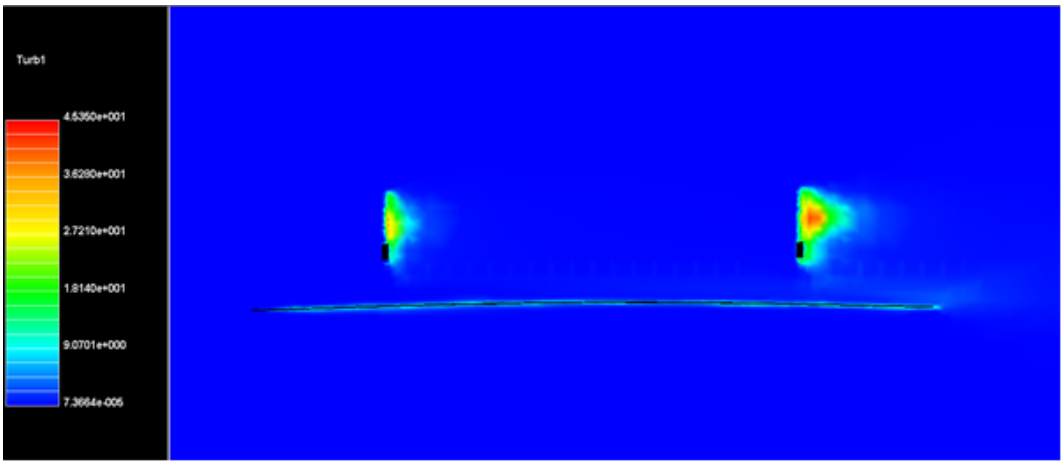

Fig. 10. Kinetic energy with turbulence in the parallel direction.

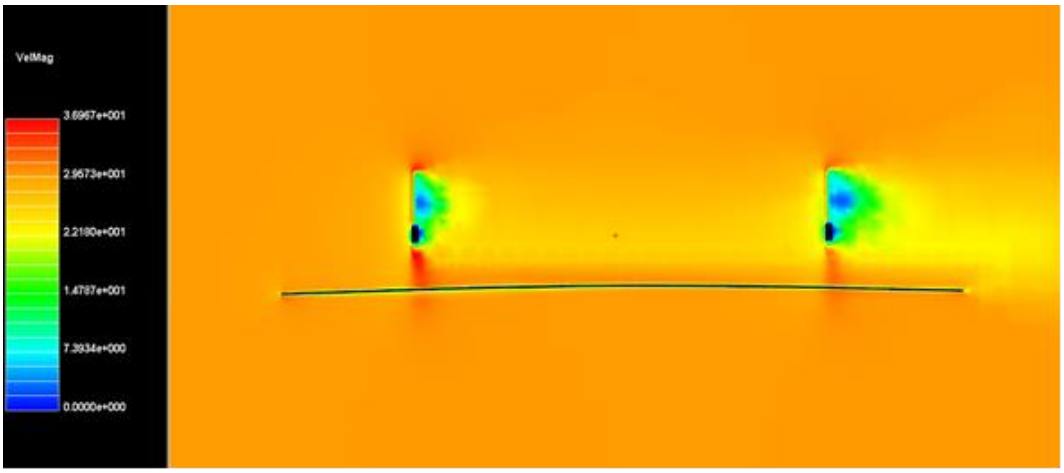

Fig. 11. Wind flow velocity on the pylons in the *x*-direction.

For the total velocity area result shown in the Fig. 12, the wind which has 30 m/s on the *x*-direction arrived the first pylon by gaining velocity. The wind flow, which goes forward by hitting the first pylon, went forward by forming vortex streets. Therefore, the wind flow has taken the second pylon by losing its velocity. In the figure, the *x*-component of velocity field shows that the vortexes, which occurred by the wind hitting to the first pylon, scattered and went forward to the second pylon. The *x*-component of the negative direction resultant of vortex streets' starts are on the merging on peak points. At these points, periodic vortex formations might be seen. The increase of vortex depth can be understood from the scattering of the wind flow velocity.

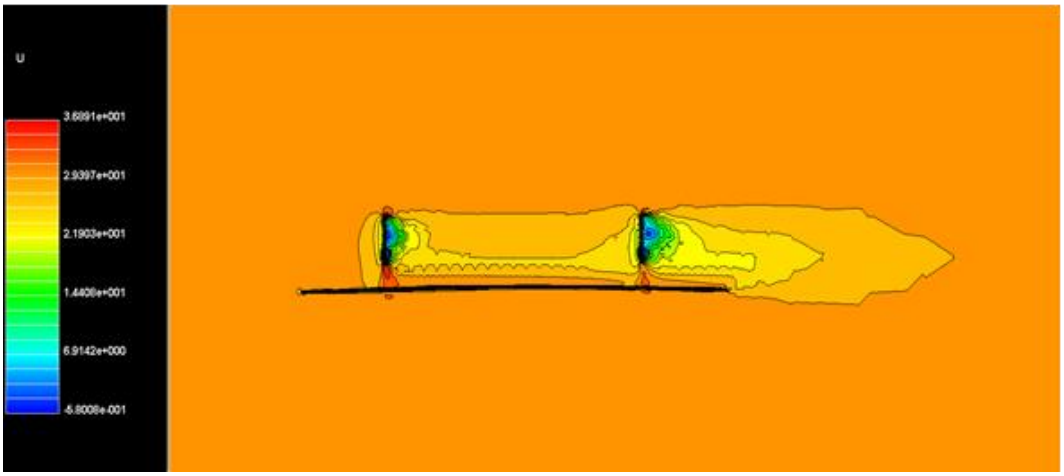

Fig. 12. Total velocity area results in the *x*-direction.

The velocity result perpendicular to the bridge way was shown in the Fig. 13. The figure indicates the wind flow velocity was not so high on the bridge deck section. This could be attributed to a larger torsional and buckling rigidity of the steel box deck on that direction.

Measurement pressure results, which affect perpendicularly to bridge tower surfaces have been nondimensionalized with dynamic pressure and served below the graphics (Figs. 14-15) with details. Pressure distribution graphics with 30m/s velocity has been interpreted by multiplying with normalized coefficients for different velocities for same graphics.

4. Conclusions

Aerodynamic behavior is the most important factor in the design of cable stayed bridges as these bridges can suffer from a high-level of vibration due to wind.

In general, maximum pressure distribution occurred on vertical surface of the tower and it goes up in direct proportion to the height of the tower. This pressure, ruling on horizontal section, has led to large shear forces on the tower. In addition, the wind flow, which goes forward by hitting the first pylon, went forward by forming vortex streets. Therefore, the wind flow has taken the second pylon by losing its velocity. However, at the effect of wind acting on *x* direction, when the vortexes which are occurred from the first pylon arrived second pylon, linear flow was broken down. Thus, the second pylon was exposed to more vortex oscillations compared to the first one. Finally, it was observed that the critical wind direction was perpendicular to the longitudinal axis of the bridge.

In a future research study, the wind-cable interaction or different wind flow velocities on the aerodynamic response of cable-stayed bridges would be studied.

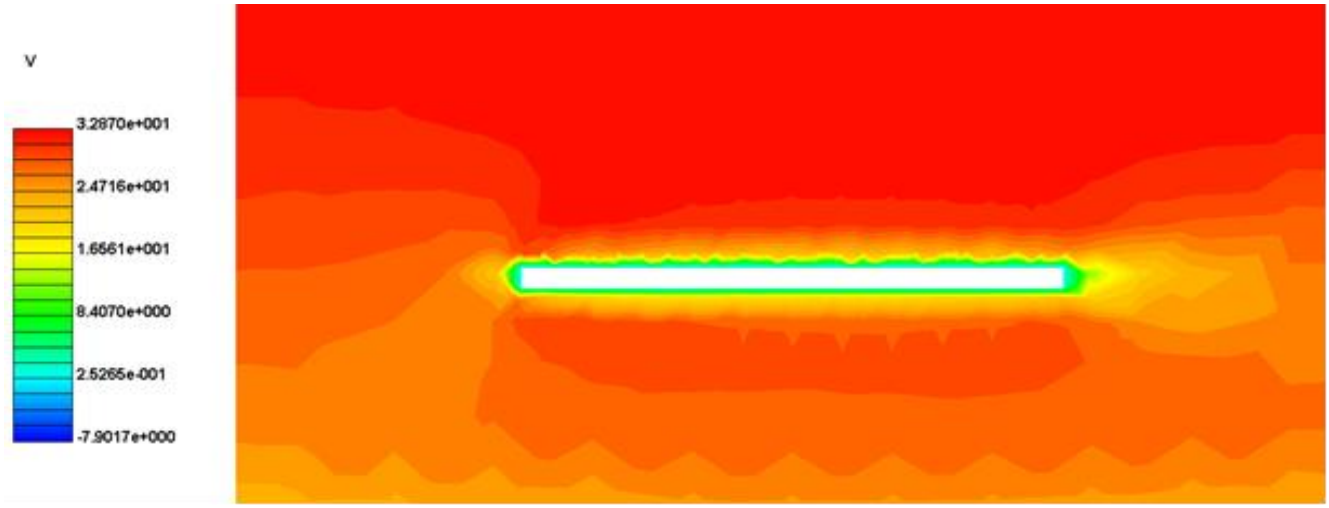

Fig. 13. Wind flow velocity on the bridge deck section in *y*-direction.

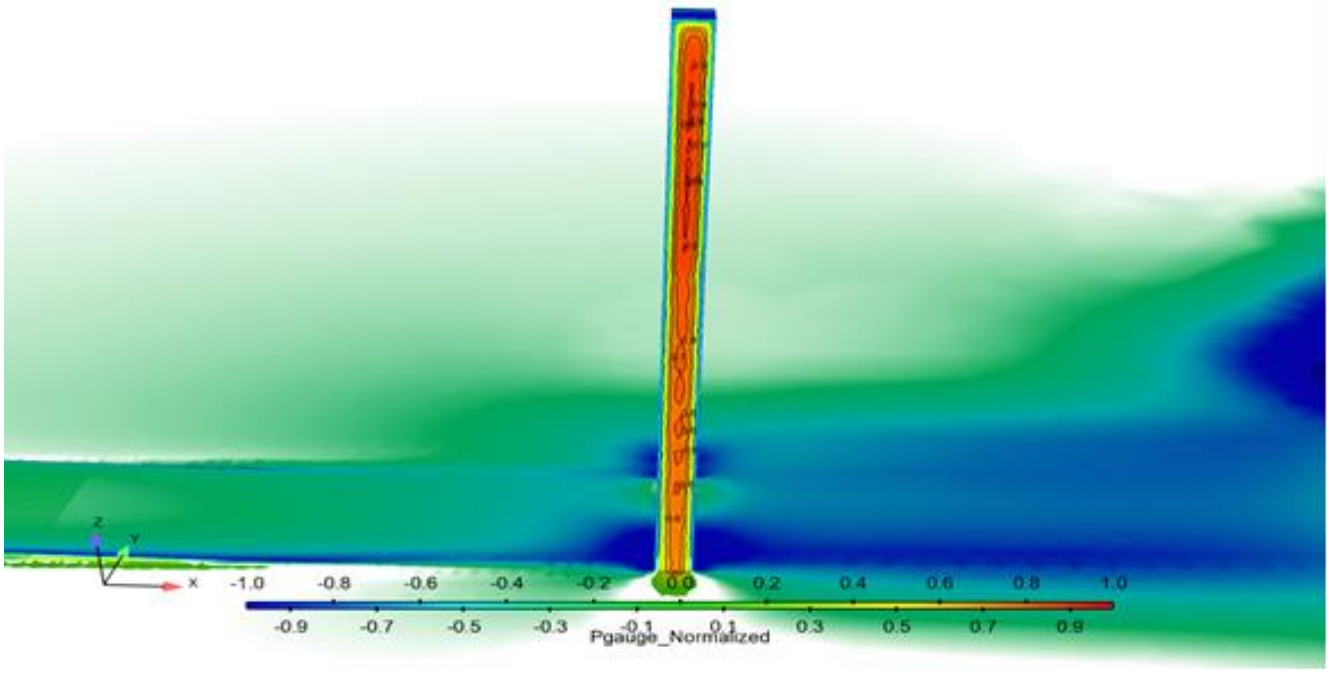

Fig. 14. Nondimensionalized pressure results of right bridge tower (wind from *y*-direction).

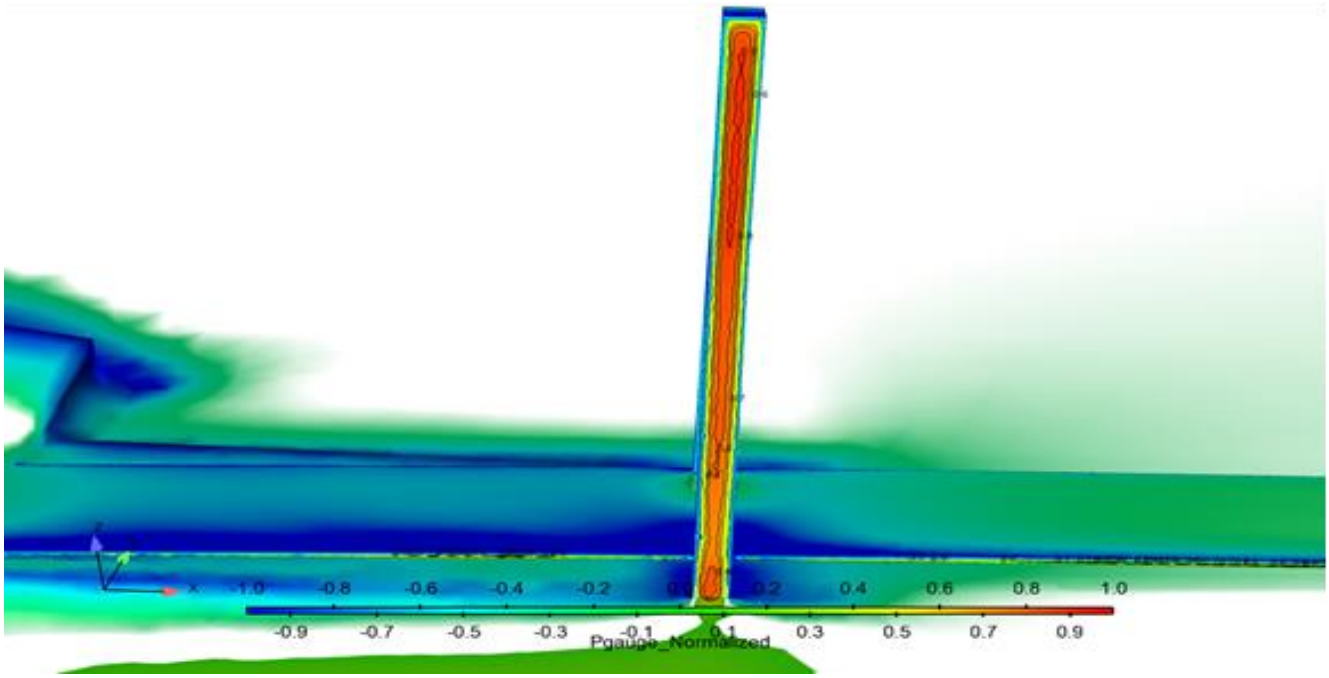

Fig. 15. Nondimensionalized pressure results of left bridge tower (wind from *y*-direction).

REFERENCES

Arioli G, Gazzola F (2013). Old and new explanations of the Tacoma Narrows Bridge collapse. *Atti XXI Congresso AIMETA*, Torino, p. 10.

Bai Y, Sun D, Lin J (2010). Three dimensional numerical simulations of long-span bridge aerodynamics, using block-iterative coupling and DES. *Computers and Fluids*, 39, 1549-1561.

Bruno L, Khris S (2003). The validity of 2D numerical simulations of vortical structures around a bridge deck. *Mathematical and Computer Modelling*, 37, 795-828.

Diana G, Fiammenghi G, Belloli M, Rocchi D (2013). Wind tunnel tests and numerical approach for long span bridges: The Messina Bridge. *Journal of Wind Engineering and Industrial Aerodynamics*, 122, 38-49.

Diana G, Yamasaki Y, Larsen A, Rocchi D, Giappino S, Argentini T, Pagani A, Villani M, Somaschini C, Portentoso M (2013). Construction stages of the long span suspension Izmit Bay Bridge: Wind tunnel test assessment. *Journal of Wind Engineering and Industrial Aerodynamics*, 123, Part B, 300-310.

Ge YJ, Tanaka H (2000). Aerodynamic flutter analysis of cable-supported bridges by multi-mode and full-mode approaches. *Journal of Wind Engineering and Industrial Aerodynamics*, 86(2–3), 123-153.

Matsumoto M, Yagi T, Shigemura Y, Tsushima D (2001). Vortex-induced cable vibration of cable-stayed bridges at high reduced wind velocity. *Journal of Wind Engineering and Industrial Aerodynamics*, 89, 633-647.

Park G, Hewson N (2008) (Eds.). ICE Manual of Bridge Engineering (2nd ed.). Thomas Telford.

Ren W, Peng X, Lin Y (2005). Experimental and analytical studies on dynamic characteristics of a large span cable-stayed bridge. *Engineering Structures*, 27, 535-548.

Xu YL, Zhang N, Xia H (2004). Vibration of coupled train and cable-stayed bridge systems in cross winds. *Engineering Structures*, 26, 1389-1406.

Yongle L, Liao H, Qiang S (2004). Simplifying the simulation of stochastic wind velocity fields for long cable-stayed bridges. *Computers and Structures*, 82, 1591-1598.

Challenge Journal of Structural Mechanics

Bonded particles models of rock plates with circular cavities in uniaxial and biaxial compression

Michail A. Lotidis *, Pavlos P. Nomikos, Alexandros I. Sofianos

Tunnelling Laboratory, School of Mining and Metallurgical Engineering, National Technical University, GR-157 80 Athens, Greece

ABSTRACT

In this paper, a distinct elements code is used to perform a numerical investigation for the size and stress gradient effects on the fracture initiation and propagation around single or pairs of pre-existing cavities in brittle rock. To investigate the rock fracture around cavities and to assess the potential of the numerical model to simulate this behavior, published laboratory physical model on granite is simulated numerically with a Bonded Particles Model (BPM). The numerical model is presented and the calibration of the BPM micro-parameters is described. Then, the calibrated BPMs are used to investigate the effect of the size of the cavity on the primary, secondary and side wall fracturing, as well as on the fracturing modes. Moreover, BPMs with two circular cavities were used to study the interaction of these holes of the same diameter and to investigate the importance of their relative distance. Finally, the simulated material was studied by biaxial tests on BPMs with a pre-existing hole.

ARTICLE INFO

Article history:
Received 26 August 2016
Accepted 1 November 2016

Keywords:
Bonded particles model
Numerical simulation
Granite
Rock fracture

1. Introduction

Over the past decade, the Bonded Particles Model (BPM) (Potyondy and Cundal, 2004) has extensively been used in order to simulate the mechanical behavior and fracture of rock under a variety of loading configurations. In the BPM, the intact rock is represented by a dense packing of rigid spheres (in 3D) or disks (in 2D) bonded together at their contacts. The model is implemented in the Particle Flow Code (PFC) (Itasca, 2014). With the recent addition of the flat-joint contact logic in the BPM (Potyondy, 2012) particle interlocking and friction resistance at the contact are imposed, restricting the relative movement of particles, and thus attaining the advantages of simulating the rock structure.

In this study, the BPM is used to model the fracture initiation and damage around cylindrical openings in compression. Published laboratory physical model on granite (Carter et al., 1991) is simulated numerically with the PFC2D by using flat-joint contact model.

2. Calibration of the Numerical Models

The mechanical properties of the granite used for the physical model experiments (Carter et al., 1991) are shown in column 3 of Table 1. The Flat-Joint Model (Itasca, 2014) was used on the BPMs for the simulation of granite's specimens. The relevant micro-parameters are presented in Table 2. Column 5 of Table 1 shows the simulation results by using the micro-parameters of Table 2. A very good match of the numerically evaluated macro-properties with the experimental ones is observed.

Carter et al. (1991) performed unconfined uniaxial compression experiments on prismatic granite specimens with a circular hole of 3.6 mm. In order to reduce friction, two granite plates of 3cm thickness were placed by the researches between the platens of the compression machine and the specimen. According to their observations, primary tensile fractures originating from the top and bottom of the cavity were initially formed at an axial stress of 16 MPa. Stable propagation of these

* *Corresponding author*. Tel.: +30-210-7721671 ; E-mail address: mlotidis@metal.ntua.gr (M. A. Lotidis)
ISSN: 2149-8024 / DOI: http://dx.doi.org/10.20528/cjsmec.2016.11.026

cracks was the only phenomenon observed until the formation of remote fractures, away from the opening, at an axial stress of 119 MPa. These were followed by slabbing at the sides of the hole when the axial stress was about 126 MPa. These observations are summarized in column 2 of Table 3. The test described by Carter et al. (1991) was completed at 157MPa, without reaching the maximum strength, in order not to destruct the specimen completely. The investigators report that cracks are not readily apparent due to the nature of the rock.

Table 1. Mechanical properties of granite (Carter et al., 1991) and simulation results.

Mechanical Property	Value	Standard deviation	Simulation results
Tensile strength (Brazilian)	14 MPa	1.2 MPa	14.3 MPa
Uniaxial compressive strength	226 MPa	15 MPa	226 MPa
Young's modulus	71.3 GPa	4.7 GPa	70 GPa

Table 2. Micro-parameters of BPM for granite.

Micro-parameter	Value	Micro-parameter	Value
Disk radius (mm)	0.36 – 0.6	Tensile strength (MPa)	14.2
Contact modulus (GPa)	65	Cohesion (MPa)	98
Stiffness ratio	2.5	Friction coefficient	0.685

Table 3. Fracture initiation stress levels in prismatic granite specimens with a cylindrical hole subjected to uniaxial compression, as observed by Carter et al. (1991) and by the BPM of this study.

Fracture type	Stress (MPa)	Standard deviation (MPa)	Simulation results (MPa)
Primary	16	2.7	17
Remote	119	10	-
Slabbing	126	12	120

In the BPMs prepared with PFC2D, the aforementioned friction angle between the platens and the specimen was set zero as the implementation of such 3cm thick plates didn't result in any substantial differences (Lotidis, 2014; Lotidis et al., 2015). The UCS simulation results of the prismatic BPM with a 3.6cm diameter hole are shown in column 4 of Table 3.

During the simulation of the physical test, primary cracks initially formed above and below the hole, initiating from the top and bottom boundary and extending towards the upper and lower surfaces of the BPM, respectively. After the initiation of the two primary fractures, a micro-cracking observed away from the hole. In the course of the UCS test, the micro-cracking becomes more widespread but scattered within the model. The slabbing at the sides of the hole starts as soon as shear cracks occur on the area of high stress concentration (AHSC) of the boundary. Finally, there is a strong presence of shear macroscopic fracture surfaces (MFSs) joining the AHSCs of the bases of the model.

It may be observed from Table 3, that the axial stress of primary fractures appearance at the top and bottom of the hole and the slabbing axial stress of physical models and BPM are in very close agreement. Any difference arising from the BPMs with those of physical models is within the respective standard deviation referred to physical specimens. Also, in Fig. 1, the similarity of the fracture pattern of the BPM with the physical model of granite may be observed. Note that Fig. 1 illustrates the two models (physical and numerical respectively) during the same applied stress level, i.e. 157 MPa. Concerning the applied axial stress of remote fractures a safe parallelism of the BPM with the physical model may not be performed.

Afterwards, five BPMs were prepared with the parameters shown in Table 2 and dimensions 20 cm x 20 cm, each containing a single circular hole at the center with varying diameter (D) 1.0, 2.0, 3.0, 3.6 and 5.0 cm. The BPMs were subjected numerically to unconfined uniaxial compression and the applied axial stress where the first tensile and shear cracks appeared at the top/bottom and at the sides of the hole's boundary respectively, were measured. In addition, the applied axial stress during the initiation of slabbing and the maximum stress attained by each BPM were recorded. These results are plotted in Fig. 2, where the variation of the abovementioned stress levels with the hole's diameter is shown. BPM with 3.6cm hole's diameter was compared with Carter's physical model (red markers) which had the same dimensions.

The effect of the hole's diameter on the fracturing stress levels is observed from Fig. 2. The numerical models have similar behavior and cracking and failure mechanisms. Specifically, primary fractures initially formed above and below the hole, which initiate from the periphery of the hole and extending towards the upper and

lower surfaces of the model, respectively. After initiation of the two primary fractures, a micro-cracking observed away from the hole. In the course of the UCS test, the micro-cracking becomes more widespread but scattered within the model. Then, the micro-cracks coalescence and one may observe an increasing curvature on the mean axial stress-axial strain curves σ_α-ε_α (Fig. 1(b)). Slabbing starts as soon as shear cracks occur on the AHSCs of the boundaries. Finally, there is a strong presence of shear MFSs joining the AHSCs with the bases of the models. Moreover, the diagram of Fig. 2 shows that the compared values reduce as the diameter of the hole increases. In addition, axial stresses at which the 1st tensile cracks are observed are similar. Finally, common for the five BPMs is the fact that the first shear cracks occurred on the boundary of the hole, either from the left or from the right, with the slabbing of the holes lie in their presence.

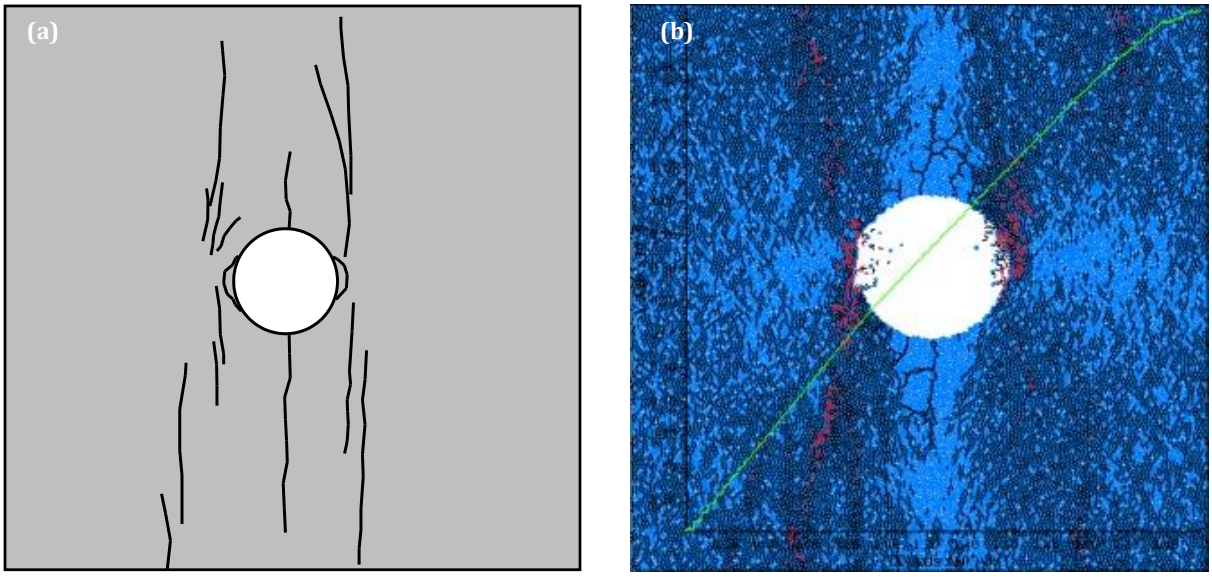

Fig. 1. Fracture pattern of: (a) granite specimen after UCS test (Carter et al. 1991) and (b) BPM micro-cracking (tensile cracks=black color, shear cracks=red color, stress-strain curve=green color, D=3.6 cm).

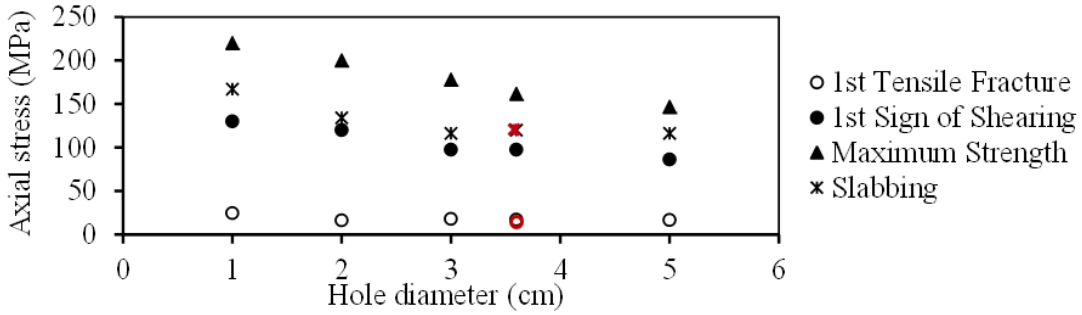

Fig. 2. Axial stress levels for 1st tensile crack/1st sign of shearing/slabbing/strength with respect to the hole's diameter, as measured from the BPMs of granite. Red markers represent the results of the physical models of Carter et al. (1991).

3. Pair of Circular Holes

The realistic results of the simulations of the previous paragraph encouraged the design of a new series of numerical models, using the micro-parameters of Table 2.

Five (5) BPMs were designed with dimensions 20 cm x 20 cm, each containing a pair of circular holes of 3cm diameter, with varying distance (X) between their centers and symmetrical relative to the center of the BPM, i.e. 4, 5, 7, 8 and 10 cm. The results of the aforementioned simulations are presented in Table 4, where the respective values of the BPM with a single circular hole of 3cm diameter are also shown. The comparative graph of Fig. 3 contains the simulation results on PFC2D for the granite BPMs with a pair of circular holes (D=3 cm). Vertical axis represents the applied axial stress (MPa) which was responsible for each phenomenon. Horizontal axis represents the distance (cm) between the holes' centers. L and R stand for "left" and "right" hole respectively.

The purpose of this test series was to study the interaction of two circular holes of equal diameter (D=3 cm) and the importance of the relative distance between them.

The UCS testing on the BPMs with a pair of holes shows similar cracking mechanism for all the numerical samples. Initially, tensile cracks are formed above and below the holes, which start from the boundary of each hole and extend to the upper and lower surfaces of the

model respectively. After the initiation of these cracks, there is some mixed-mode micro-cracking, i.e. appearance of tensile and shear cracks, away from the holes. During the progress of the UCS testing, this micro-cracking extends at an angle of 45° (with respect to the center of each hole) to four directions, tending to join the AHSCs. The MFSs with direction from the left opening to the right and from the right hole to the left extend to meet each other in the vertical axis of symmetry of the BPM, and as a result the numerical specimen tends to fail on the symmetry axis.

For the distance of 4 cm, the pillar between the two holes was collapsed, while the surfaces of cracks reached the underside of the model, in combination with the MFS on the vertical axis of symmetry at the top of the model, and as a result they separate the numerical model into three large pieces. The numerical model with 5 cm distance has a similar to the previous BPM failure mechanism, except that the pillar between the two holes didn't collapse. Finally, the holes of the three other numerical models with distances 7 cm, 8 cm and 10 cm tend to behave as independent.

Table 4. Comparative table of the simulation results on PFC2D for Lac du Bonnet granite BPMs with a single and pair of circular holes (D=3 cm).

D=3 cm	UCS (MPa)	Primary fracture (left hole) (MPa)	Primary fracture (right hole) (MPa)	Slabbing (left hole) (MPa)	Slabbing (right hole) (MPa)
Single	178	18	18	116	116
Pair X=4 cm	148	18	17.8	75.4 (right)	90 (left)
Pair X=5 cm	152	16	20	110 (right)	112 (right)
Pair X=7 cm	138	22	14.4	109 (right)	107 (right)
Pair X=8 cm	147.5	16.8	17.8	110 (right)	105 (left)
Pair X=10 cm	133	13.9	15.2	97 (left)	102 (right)

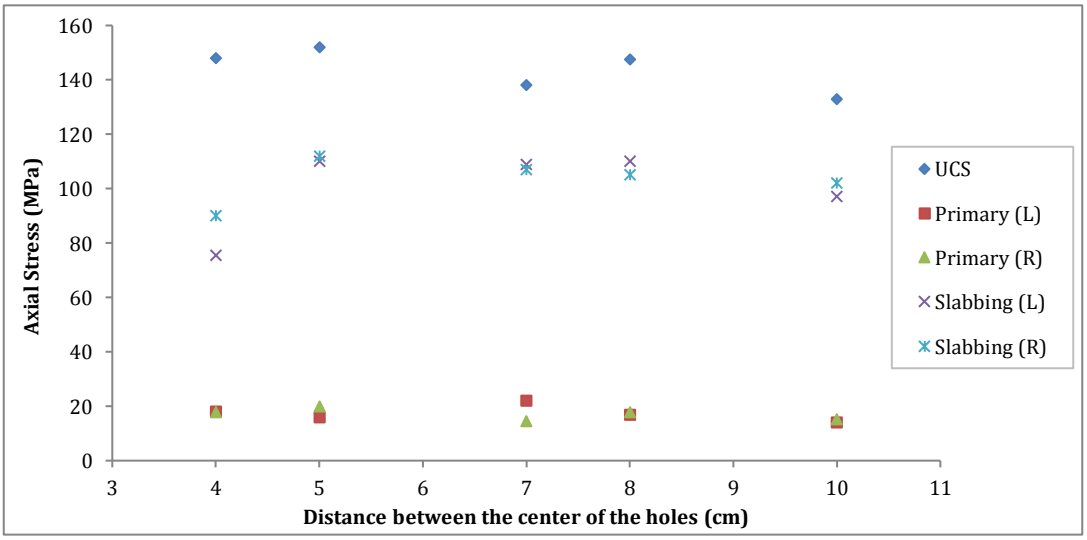

Fig. 3. Comparative graph of the simulation results on PFC2D for granite BPMs with a pair of circular holes (D=3 cm). Vertical axis represents the applied axial stress (MPa) which was responsible for each phenomenon. Horizontal axis represents the distance (cm) between the holes' centers. L and R stand for "left" and "right" hole respectively.

Observing the values (maximum strength/primary fracture on the left and right hole/slabbing of the left and right hole) of Table 4, it seems that the maximum strength of the numerical model decreases with the increasing distance between the two holes, while the initiation of the primary crack at the upper or lower boundary of the holes is observed at similar level of mean axial stress on the six BPMs. Moreover, on the first BPM (X=3 cm) as expected, the slabbing begins from the right of the left hole and from the left of the right hole due to the high stress concentration stress distribution through the pillar.

The fracture patterns obtained from UCS testing on PFC2D of granite BPMs with a pair of circular holes (D=3 cm) are given below in Fig. 4. The green curves represent the applied axial stress vs the axial strain (σ_α-$E_{\varepsilon\alpha}$). Disks with different color than blue represent fragments.

4. Biaxial Test

The last simulation series of this study contains biaxial compressive tests on PFC2D, by using the BPM that was designed for the simulation of the physical experiment of Carter et al. (1991), i.e. 20cm x 20cm and D=3 cm. Four (4) biaxial tests took place with different lateral stress p, i.e. 2, 5, 10 and 20 MPa, following the same methodology: first, the BPM is submitted into increasing hydrostatic stress field beginning from 0 MPa until $\sigma_1 = \sigma_3 = p$. Then, the lateral stress remains constant ($\sigma_3 = p$) within an approximate error equal to 0.05%, and the applied axial stress (σ_1) increases until the collapse of the BPM.

The concept of the fracture process and mechanism for the biaxial tests stays the same as for the UCS test of paragraph No 2. Noteworthy is the micro-cracking initiation when $p \geq 5$ MPa, as the first micro-cracks are nucleated either at the left or the right of the boundary of the hole, instead of the upper or lower, i.e. primary fractures. In addition, during the biaxial tests, shear micro-cracking becomes more intense than the UCS test, leading on the creation of small fragments along the MFSs. The size of these fragments decreases as the lateral stress increases. They start from the four (4) MFSs and they pullulate as the axial stress σ_1 increases.

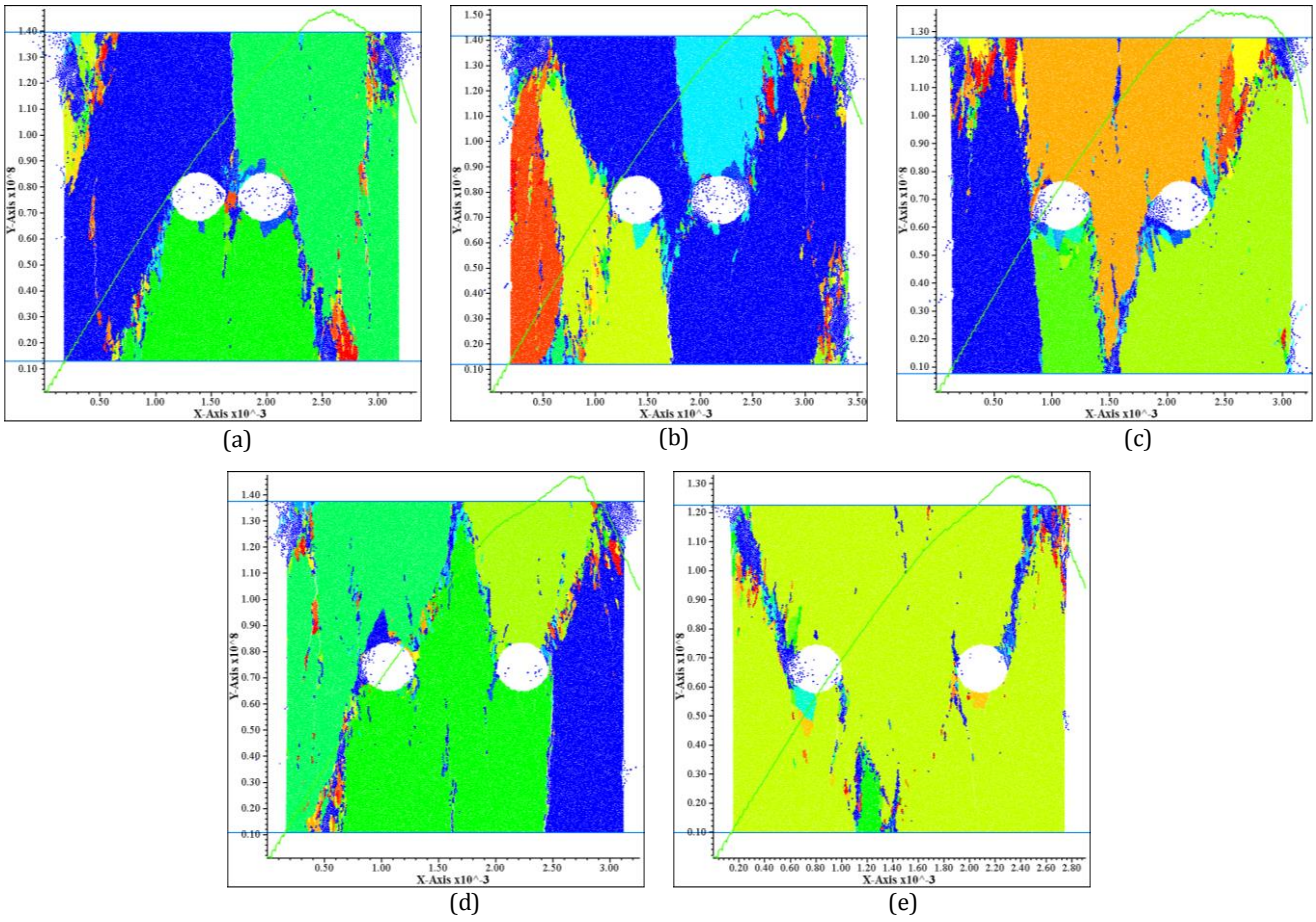

Fig. 4. BPMs of granite with a pair of holes (D=3 cm) after the UCS testing on PFC2D. Disks with different color than blue represent fragments. (a) X=4 cm; (b) X=5 cm; (c) X=7 cm; (d) X=8 cm; (e) X=10 cm.

Fig. 5 presents the simulation results in comparison with the UCS values of the same BPM. Blue, red, green, purple and light blue markers represent the maximum strength of the BPM, the primary fracture initiation, the slabbing initiation and the total length of the upper and the lower primary fracture respectively. As one may observe, the total length of the primary fractures decreases as the lateral stress increases. On the other hand, the maximum strength and the applied axial stress for the primary fracture initiation increase. In this series, slabbing initiation occurs on higher stress levels than the UCS test, but it remains on the same magnitude for each biaxial test.

The fracture patterns obtained from biaxial testing on PFC2D of granite BPM with a circular hole (D=3.6 cm) are given in Fig. 6. The green curves represent the applied axial stress vs the volumetric strain (σ_α-ε_{vol}). Disks with different color than blue represent fragments.

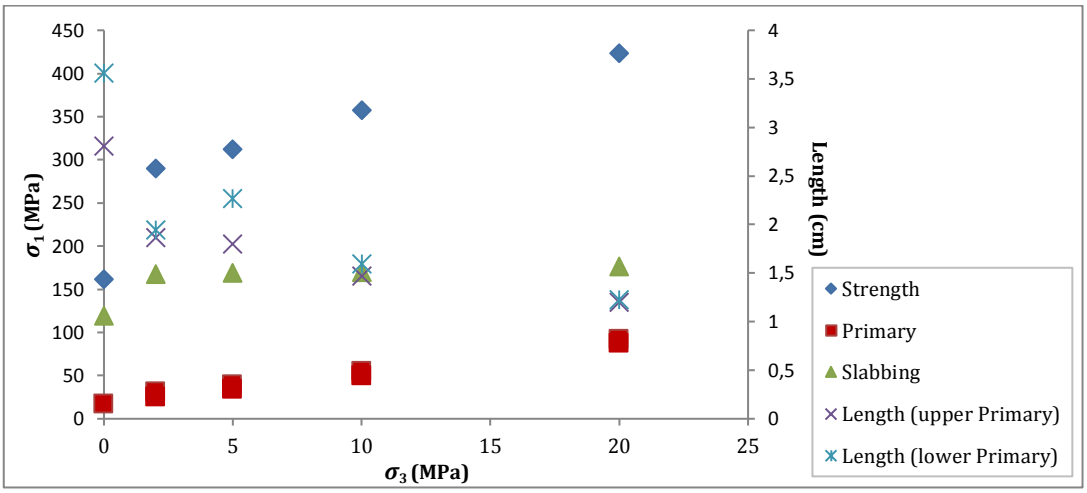

Fig. 5. Simulation results of biaxial tests on PFC2D for BPM of granite. Blue, red, green, purple and light blue values represent the maximum strength of the BPM, the primary fracture initiation, the slabbing initiation and the total length of the upper and the lower primary fracture respectively.

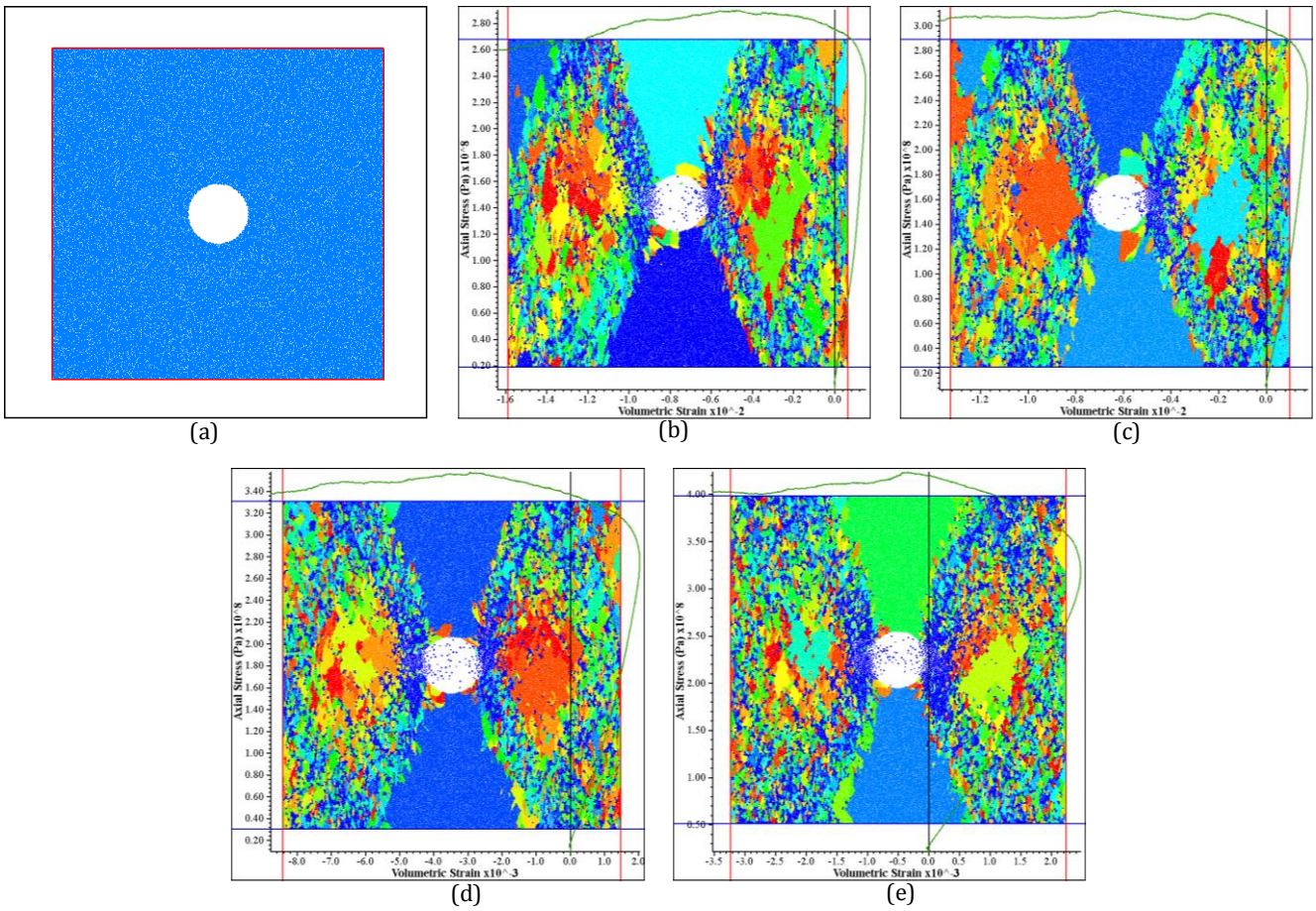

Fig. 6. BPM of granite with a single hole (D= 3.6 cm) after the biaxial testing on PFC2D. Disks with different color than blue represent fragments. (a) Intact; (b) σ_3 = 2 MPa; (c) σ_3 = 5 MPa; (d) σ_3 = 10 MPa; (e) σ_3 = 20 MPa.

5. Conclusions

Laboratory physical model of granite with a circular hole is simulated numerically with the PFC2D code. The macroscopic fracture propagation and failure pattern of the BPM are in close agreement with laboratory observations. The different diameters of the hole revealed the importance of size for the underground openings. BPMs with two pre-existing holes have relative fracture propagation and failure patterns. Biaxial tests revealed differences in fracture mechanisms observed in comparison with UCS tests, and these differences become more significant as the lateral stress is augmented. Further investigation is required for the micro-mechanisms leading to damage accumulation and fracture around large-scale openings in compression.

REFERENCES

Carter BJ, Lajtai EZ, Petukhov A (1991). Primary and remote fracture around underground cavities. *International Journal for Numerical and Analytical Methods in Geomechanics*, 15(1), 21-40.

Itasca Consulting Group Inc (2014). PFC 5.0 Documentation.

Lajtai EZ (1971). A theoretical and experimental evaluation of the Griffith theory of brittle fracture. *Tectonophysics*, 11, 129-156.

Lotidis MA (2014). The Approach of Synthetic Rock Mass for the Numerical Simulation of the Brittle Rocks' Failure around Underground Openings. *Diploma Thesis*, School of Mining and Metallurgical Engineering NTUA, Athens, Greece.

Lotidis MA, Nomikos PP, Sofianos AI (2015). A numerical investigation of rock fracture around cavities in compression. *Proceedings of Eurock 2015: Future Development of Rock Mechanics*, Salzburg, Austria, 719-724.

Potyondy DO, Cundall PA (2004). A bonded-particle model for rock. *International Journal of Rock Mechanics and Mining Sciences*, 41, 1329-1364.

Potyondy DO (2012). A flat-jointed bonded-particle material for hard rock. *Proceedings of the 46th US Rock Mechanics Symposium*, Chicago, USA, paper ARMA 12-501.

Challenge Journal of Structural Mechanics

High strain rate and quasi-static compression behavior and energy absorption characteristic of PVC foam

Zhang Wei *, Ye Nan

Hypervelocity Impact Research Center, Harbin Institute of Technology, 150001 Harbin, PR China

ABSTRACT

The mechanical properties at room temperature of two densities PVC foams have been experimentally evaluated in both quasi-static and dynamic compression loading conditions. The strain rate effect have been evaluated by comparing the constant strength during plateau region. Energy absorption efficiency of PVC foam is investigated, and it shows that in certain density range, the efficiency of lighter PVC foam is larger than that of heavier PVC foam, but the efficiency stress of lighter PVC foam is smaller than that of heavier PVC foam. While the lighter PVC foam has been compressed more than heavier PVC foam when they reach their peak efficiency. Therefore, for a certain density of PVC foam itself, when the loading rates increase, the PVC foam will absorb more energy more efficiently.

ARTICLE INFO

Article history:
Received 13 September 2016
Accepted 11 November 2016

Keywords:
PVC foam
Mechanical properties
Strain rates effect
Energy absorption

1. Introduction

Foam materials have been extensively used in civil and military field such as energy absorbers to resist external loads (Zhu et al., 2010; Kabir et al.,2014). For example aluminum foam, it has already been widely investigated Deshpande and Fleck (2005); Lu et al. (2009). PVC, which stands for polyvinyl chloride, is a new type of structural functional materials, and it could be produced into PVC foam with high porosity, low density and low cost, which offers similar but higher performance ability of remaining a constant nominal stress in large plastic deformation than normal foam materials. And it is often used in Sandwich plates as core materials to make full use of advantages of the capability of dissipating considerable energy by large plastic deformation under static or dynamic loading. Avachat and Zhou (2015) investigate planar composites with PVC foam cores and E-glass/vinylester face sheets subjected to underwater shock. It is proposed that Low density PVC foams cores exhibiting better capabilities for compression than that of higher density cores. A major aim of this study is to provide a simple but reliable description of the compression behavior and energy absorption characteristic of PVC foams with the effect of strain rates of different densities.

2. Experimental Program

Density of polyvinyl chloride foam, short for PVC foam, is easily controllable, because of the porous property. While two different densities of PVC foams materials are considered in this test, which are 80 kg/m^3 (short for P80) and 160 kg/m^3 (short for P160). And each density of PVC foam specimens is cut into cylinder with nominal dimension of Φ30×10 mm from PVC foam layers with 10 mm thickness (Fig. 1).

Two densities of PVC foams specimens are compressed under quasi-static and dynamic loading, to determine their stress-strain relationship and strain-rate effect of them. Quasi-static tests are conducted on a micro-controlled electronic universal testing machine in room temperature. While PVC foams are compressed at constant given velocity between two steel plates. The given speeds are 1 mm/min and 100 mm/min in this test, which means that the strain rates were 0.167/s and 0.0016/s respectively.

Strain-rate effect is an important consideration to evaluate the mechanical characteristics of materials. And it is widely recognized as a crucial factor that influences the mechanical properties of materials. Because of the matrix material, entrapped air, as well as micro-inertia effect, foam material often exhibits very deep strain rate effect.

* *Corresponding author*. E-mail address: zhdawei@hit.edu.cn (Z. Wei)
ISSN: 2149-8024 / DOI: http://dx.doi.org/10.20528/cjsmec.2016.11.028

Therefore, accurate dynamic behavior is important in researching mechanical property of PVC foam. SHPB, which is short for split Hopkinson pressure bar, is a commonly used experimental technique to study constitutive laws of materials at high strain rates. In this test, a Φ40 mm split Hopkinson pressure bar is employed in the dynamic compressive tests for high strain rates. As shown in Fig. 2, strain gauges are glued on incident bar, transmitted bar as well as the Φ30×10 mm specimens. Dynamic tests were performed in room temperature till strain rate up to 3000/s.

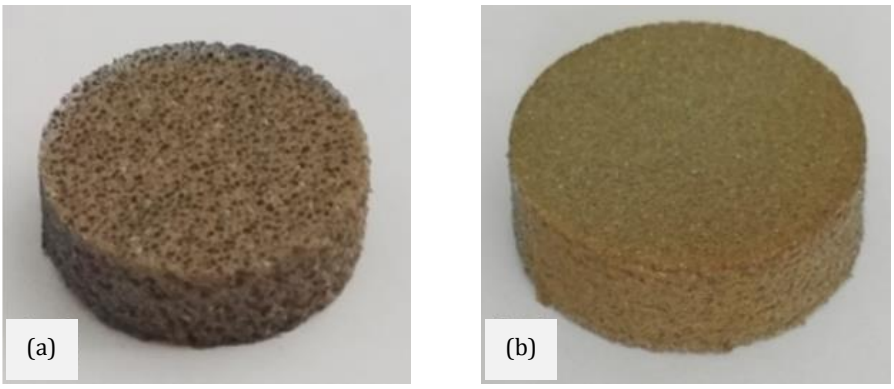

Fig. 1. Cylinder specimen (Φ30×10 mm) of the two densities PVC foams: (a) P80; (b) P160.

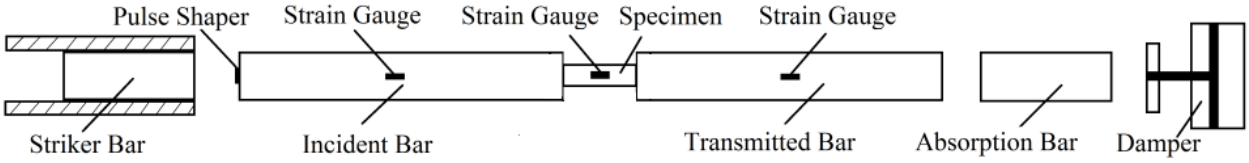

Fig. 2. Schematic of modified SHPB apparatus and specimen.

3. Results and Discussion

The ability of energy absorption and the accuracy of the finite element analyze are highly dependent on the accurate material parameters of PVC. In this test, uniaxial compression tests were performed at different strain rates in order to determine the sensitivity of the mechanical response to the loading rate. Fig. 3(a, b) shows the strain-stress curves of the two densities of PVC foams, 80 kg/m^3 and 160 kg/m^3 respectively, and it shows the strain rates effect between 10^{-3}/s and 3×10^3/s of the two densities of PVC foams. It has been indicated that the compression curves of PVC foams experience the typical deformation process of the metallic foams, and the strain-stress curves comprise of three apparently stages. At first it is elastic stage, the material and structure start to be compressed elastically, while in this stage a sharp linear increase in stress is observed with the strain increasing a little. Then it comes along with plateau stage, in which the stress keep almost stable or the slope of the curve is very small for a large range of strain, and the structure collapse occurred mostly in this stage, while the second stage is the main contributor to the large energy absorption capacity of foam materials. At last it is densification stage, and the cell wall itself have been pressed together, however it is seems that the stress increase exponentially.

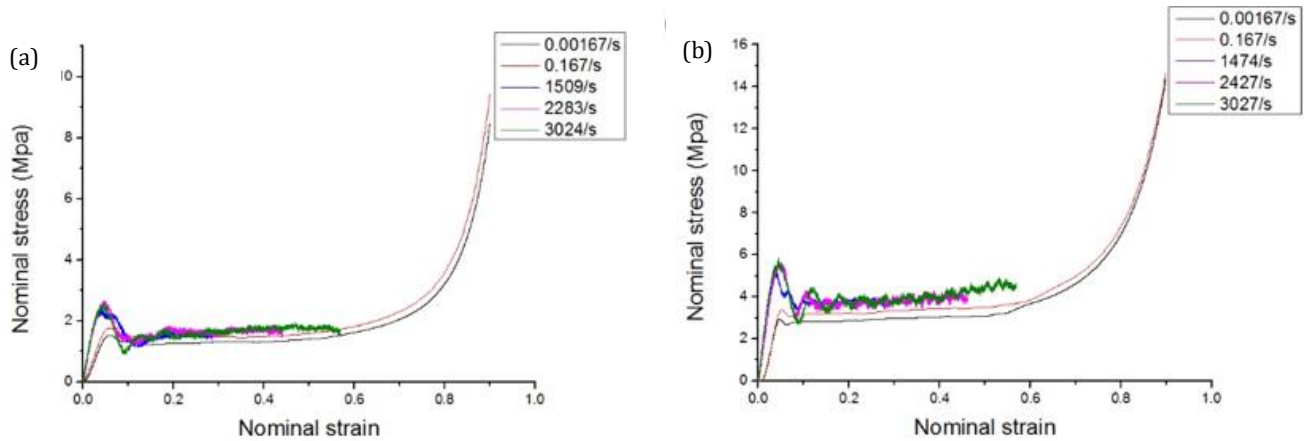

Fig. 3. Nominal strain-stress curve of the two relative densities of PVC foam: (a) P80; (b) P160.

Constant plateau stress in large plastic deformation is the most important factor of PVC foams in blast resistance. Table 1 shows the plateau stresses of the two densities of PVC foams under same or close strain rates. It is found that the plateau stresses increase with increasing strain rate in quasi static and dynamic compression conditions. And in quasi-static region, the plateau stress of strain rates 0.167/s of the two PVC foams increase nearly the same time as it is of strain rates 0.00167/s. Therefore in the dynamic region, the plateau stress of PVC foam with higher density increase faster than that with lower density. And as the two densities PVC foams themselves, the plateau stress increase faster than the density increasing, while it is indicated that when the PVC foams are applied as shield, heavier PVC foam may performed well within certain range even weight being considered.

Table 1. σ_n of the two density PVC of different strain rates.

Strain rates	σ_p (MPa)			
	P80	Difference	P160	Difference
0.00167	1.30	/	2.93	/
0.167	1.48	13.8%	3.32	13.3%
3025±2	1.65	26.9%	3.99	36.2%

The light PVC foams own the excellent energy absorption capability because of the ability of remaining nearly constant plateau stress in large plastic deformation. And the energy absorbed during compression, which is equals to the area under the strain-stress curve, is defined as:

$$W = \int_0^{\varepsilon} \sigma(e)\, de\,. \tag{1}$$

By doing the research on energy absorption characteristic of foam materials, an energy absorption efficiency parameter was presented Miltz and Ramon, (1990); Avalle et al. (2001). And the efficiency parameter was defined as a ratio between the absorbed energy up to a certain strain and the stress of the strain itself, as following:

$$E = \frac{1}{\sigma}\int_0^{\varepsilon} \sigma(e)\, de\,. \tag{2}$$

Energy absorption efficiency-stress curves under quasi-static loading of the two densities of PVC foams are shown in Fig. 4(a), and the peak efficiency of P80 foam is 48.1%, while the efficiency stress is 1.72 MPa, and the efficiency strain is 0.63; however the peak efficiency of P160 is 47.7%, while the efficiency stress is 3.25 MPa and the efficiency strain is 0.55. And it indicated that the efficiency stress of P160 is higher than that of P80. And the efficiency of lighter PVC foam is larger than that of heavier PVC foam, however the difference is very small. While the lighter PVC foams compressed more than that of heavier PVC foam when they reach their peak efficiency.

Energy absorption efficiency-stress curves under different strain rates of P160 foams are shown in Fig. 4(b). The curve of P160 foam in dynamic compression condition is not complete, because of the lack of loading intensity, but it is already indicated that as the loading rates increasing, the energy absorption efficiency, the efficiency stress and efficiency strain are all increasing. It means that when the strain rates increase, the PVC foam will absorb more energy in more efficient way.

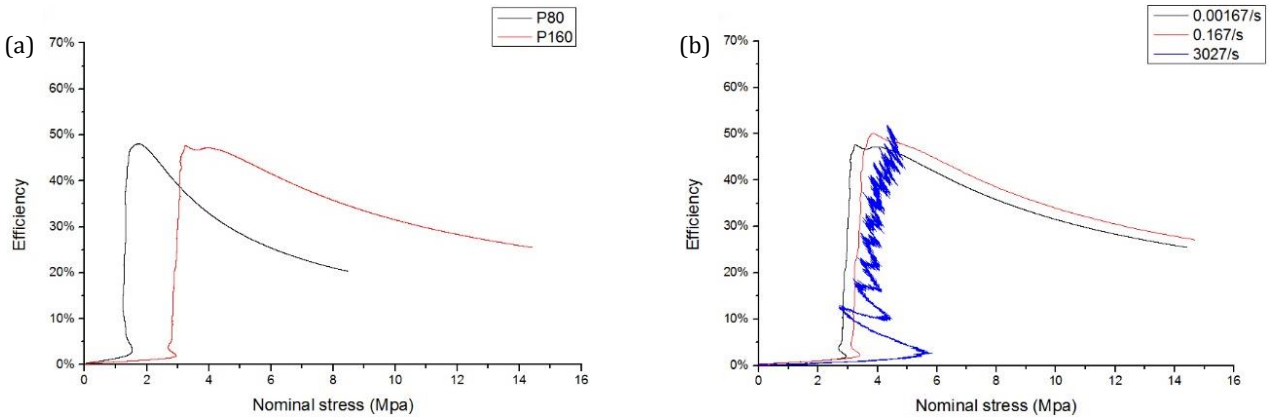

Fig. 4. Energy absorption efficiency-stress curves:
(a) two different densities of PVC foams; (b) three different strain rates of P160.

4. Conclusions

In this study, the high strain rates and quasi–static compression behaviors of two low densities of PVC foams, 80 kg/m^3 and 160 kg/m^3, are obtained by using split Hopkinson pressure bar and micro-controlled electronic universal testing machine. The results show that the strain-stress curves of PVC foams conclude three apparently stages, which are elastic stage, plateau stage and densification stage respectively. In certain density range, the PVC foams are strain rate sensitive materials. While in quasi-static loading conditions, the plateau stress of the two PVC foams increase in nearly same speed. Therefore in dynamic loading conditions, the plateau stress of PVC foam with higher density increase faster than that with lower density.

Energy absorption efficiency is also investigated in this study. And it shows that for different densities of PVC foams, the energy absorption efficiency of lighter PVC foam is larger but in small difference than that of heavier PVC foam, and the lighter PVC foams compressed more than that of heavier PVC foam when they reach their peak efficiency. While the efficiency stress of P160 is higher than that of P80. Therefore by comparing the energy absorption efficiency of different strain rates, it shows that the energy absorption efficiency, the efficiency stress and efficiency strain all increase as the strain rates increasing.

Acknowledgements

The authors would like to thank the National Natural Science Foundation of China (No. 11372088) for supporting the present work.

References

Avachat S, Zhou M (2015). High-speed digital imaging and computational modeling of dynamic failure in compo site structures subjected to underwater impulsive loads. *International Journal of Impact Engineering*, 77, 147-165.

Avalle M, Belingardi G, Montanini R (2001). Characterization of polymeric structural foams under compressive impact loading by means of energy-absorption diagram. *International Journal of Impact Engineering*, 25, 455-472.

Deshpande VS, Fleck NA (2005). One-dimensional response of sandwich plates to underwater shock loading. *Journal of the Mechanics and Physics of Solids*, 53, 2347–2383.

Fleck NA, Deshpande VS (2004). The resistance of clamped sandwich beams to shock loading. *Journal of Applied Mechanics*, 71(3), 386-401.

Miltz J, Ramon O (1990). Energy absorption characteristics of polymeric foams used as cushioning materials. *Polymer Engineering and Science*, 30(2), 129–133.

Qiu X, Deshpande VS, Fleck NA (2004). Dynamic response of a clamped circular sandwich plate subject to shock loading. *Journal of Applied Mechanics*, 71(5), 637-645.

Radford DD, McShane GJ, Deshpande VS et al. (2006). The response of clamped sandwich plates with metallic foam cores to simulated blast loading. *International Journal of Solids and Structures*, 43, 2243–2259.

Xu A, Vodenitcharova T, Kabir K (2014). Finite element analysis of indentation of aluminum foam and sandwich panels with aluminum foam core. *Materials Science and Engineering: A*, 599, 125-133.

Yuan JY, Chen X, Zhou WW (2015). Study on quasi-static compressive properties of aluminum foam-epoxy resin compo site structures. *Composites Part B: Engineering*, 79, 301-310.

Zhu F, Wang Z, Lu G (2009). Analytical investigation and optimal design of sandwich panels subjected to shock loading. *Materials and Design*, 30, 91-100.

Zhu F, Wang ZHH, Lu GX (2010). Some theoretical considerations on the dynamic response of sandwich structures under impulsive loading. *International Journal of Impact Engineering*, 37, 625–637.

Challenge Journal of Structural Mechanics

Optimum design of reinforced concrete columns employing teaching-learning based optimization

Gebrail Bekdaş *, Sinan Melih Niğdeli

Department of Civil Engineering, İstanbul University, 34320 İstanbul, Turkey

ABSTRACT

In structural engineering, the design of reinforced concrete (RC) structures needs an initial de-sign for cross sectional dimensions. After these dimensions are defined, the design constraints and the required reinforcement bars are calculated. But the required reinforcement area is not exactly provided since the size of rebars are fixed. At the end of the design, the security measures are provided, but the designer has no idea for the optimization of the design in mean of economy. For that reason, a powerful search methodology can be programed by using metaheuristic algorithms. In this study, optimum design of reinforced concrete columns was investigated by using an education based metaheuristic algorithm called teaching-learning based optimization (TLBO). In the methodology, the slenderness of the columns is also taken into consideration by using a simple approach given in the ACI 318 design code. In this approach, the factored design flexural moments are defined according to the buckling load and axial load of columns. The design variables of the problem include cross section dimension of the column and the detailed reinforcement design and the optimization objective is the minimization the maximum material cost of the column. Differently from the other metaheuristic algorithms, the decision of the optimization type (global or local search) is not defined by using a probability parameter in TLBO. In optimization, two phases of TLBO; teacher (global search) and learner (local search) phases are consequently applied in search of best design variables. The proposed approach is effective for the structural optimization problem.

ARTICLE INFO

Article history:
Received 29 September 2016
Accepted 14 November 2016

Keywords:
Optimization
Metaheuristic algorithms
Teaching-learning based optimization
Reinforced concrete
Columns

1. Introduction

In the design of reinforced concrete (RC) members, a design engineer decides several initial element dimensions and these dimensions are used in the detailed design of the reinforcements. The experience of engineer effects the economic design of RC member. The only way is to find a better design is to try several member sizes if a design software is used. These trials may be several times, but it cannot be thousand times. For that reason, optimization is needed to carry out iterations. Thus, an optimum design ensuring all design constraints can be found. The optimum design methods are proposed for several RC members such as frames (Balling and Yao, 1997; Guerra and Kiousis, 2006), beams (Barros et al., 2005; Barros et al., 2012; Ferreira et al., 2003), prestressed concrete bridges (Sirca and Adeli, 2005), columns (Gil-Martin et al., 2010) and slabs (Ahmadkhanlou and Adeli, 2005).

By using mathematical methods, it is only possible to find optimum results with some assumptions. In order to carry out a practical optimization, metaheuristic methods are suitable. The one of the metaheuristic methods used in the optimum design of RC members is genetic algorithm (GA). GA is used in the design of beams (Coello et al., 1997; Govindaraj and Ramasamy, 2005; Fedghouche and Tiliouine, 2012), columns (Rafiq and Southcombe, 1998), frames (Rajeev and Krishnamoorthy, 1998; Camp et al., 2003; Lee and Ahn, 2003; Govindaraj and Ramasamy, 2007). In order to provide effective optimum

* *Corresponding author*. Tel.: +90-212-4737070 ; Fax: +90-212-4737180 ; E-mail address: bekdas@istanbul.edu.tr (G. Bekdaş)
ISSN: 2149-8024 / DOI: http://dx.doi.org/10.20528/cjsmec.2016.11.030

results, several algorithms can be combined in a single method. Rath et al. (1999) combined GA with sequential quadratic programming (SQP) for optimum design of RC members. Similarly, simulated annealing (SA) and Hook-Jeeves method are used with GA by Leps and Sejnoha, (2003) and Sahab et al. (2005), respectively.

In several studies (Paya et al., 2008; Paya-Zaforteza et al., 2009; Ceranic et al., 2001; Yepes et al., 2008), SA is employed in the optimization of RC members. Perea et al. (2008) optimized RC frames of bridges by using a methodology employing SA, the threshold accepting, random walk and the descent local search. Fiber-reinforced composite plates are optimized by Rama Mohan Rao and Shyju, (2010). SA and tabu search (TS) are combined in the method.

Another metaheuristic algorithm used in the optimum design of RC members is big bang big crunch algorithm (Camp and Akin, 2012; Camp and Farah Huq, 2013; Kaveh and Sabzi, 2012). The music inspired harmony search (HS) algorithm developed by Geem et al. (2001) is used in the optimization of RC retaining walls (Kaveh and Abadi, 2011), RC continuous beams (Akin and Saka, 2010), RC frames (Akin and Saka, 2012) and RC beams (Bekdaş and Nigdeli, 2012) and columns (Bekdaş and Nigdeli, 2014; Nigdeli et al., 2015). Also, bat algorithm (BA) is employed for optimum design of RC columns (Bekdaş and Nigdeli, 2016).

In this paper, teaching-learning based optimization developed by Rao et al. (2011) is employed for the detailed optimum design of RC columns and results are compared with the results obtained by employing HS (Bekdaş and Nigdeli, 2014) and BA (Bekdaş and Nigdeli, 2016). In the methodology, the slenderness effect is considered by using moment magnification factor and the design of RC column is carried out according to ACI318 regulation. The methodology is coded in Matlab and the result is obtained for different heights of the column in order to see the effect of the slenderest.

2. Methodology

The teaching and learning process of a class is the inspiration of teaching-learning based optimization (TLBO) method. In a class, two phases of education are used. These phases are teacher and learner phases which are consequently applied.

As all numerical optimization algorithms, the problem must be defined. The problem data contain possible ranges of design variables, design constraints and algorithm parameters. The design variables of the RC column optimization are breadth (b_w), height (h), number and size of bars in face (web or essential reinforcement), size of shear reinforcements and distance of shear reinforcements.

The design constants are shown in Table 1 with the values used in numerical example. TLBO is lucky in algorithm parameters because the population of class is only defined by a user. Since two phases of the algorithm are consequently applied, a probability to choose the type of the optimization is not needed. In generation of new design variables, a teaching factor (TF) is used but it is not a user defined value. TF is randomly assigned and may be 1 or 2.

Table 1. Design constant and ranges of design variables.

Definition	Value
Range of web width, b_w	250 mm-400 mm
Range of height, h	300 mm-600mm
Longitudinal reinforcement (ϕ)	16 mm-30 mm
Shear reinforcement (ϕ_v)	8 mm-14 mm
Effective length factor in buckling, k	1.2
Clear cover, c_c	30mm
Max. aggregate diameter, D_{max}	16 mm
Yield strength of steel, f_y	420 MPa
Comp. strength of concrete, f'_c	25 MPa
Elasticity modulus of steel, E_s	200000 MPa
Specific gravity of steel, γ_s	7.86 t/m^3
Specific gravity of concrete (γ_c)	2.5 t/m^3
Cost of the concrete per m^3	40 $
Cost of the steel per ton	400$

After the required values are defined, an initial solution matrix is generated. These matrix contains vectors assigned with randomly generated design variables and the number of these vectors are equal to population number of the class.

Also, the objective functions of all possible designs in the vectors are calculated by controlling ACI 318 requirements and if a constraint violation is observed, the objective function defined as Eq. (1) is penalized with a huge cost.

$$min\, f(x) = C_c V_c + C_s W_s\,, \quad (1)$$

In the objective function, the cost of the column is calculated and C_c, C_s, V_c and W_s are cost of concrete per m^3, cost of the steel per ton, total concrete volume and total weight of steel, respectively.

After generation of the initial solution matrix, the best solution ($X_{teacher}$) (solution with minimum objective function) is chosen as a teacher. Thus, a new solution ($X_{new,i}$) is found according to Eq. (2) in teacher phase by modifying old solution ($X_{old,i}$) of the i^{th} vector in the class. rnd(0,1) is a random number between 0 and 1 while X_{mean} is the mean of the class.

$$X_{new,i} = X_{old,i} + rand(0,1) \cdot (X_{teacher} - T_F \cdot X_{mean})\,. \quad (2)$$

Then, student phase starts and Eq. (3) is used in generation.

$$X_{new,i} = \begin{cases} X_{old,i} + rnd(0,1) \cdot (X_i - X_j);\ f(X_i) > f(X_j) \\ X_{old,i} + rnd(0,1) \cdot (X_j - X_i);\ f(X_i) < f(X_j) \end{cases}. \quad (3)$$

In this generation, j^{th} and k^{th} solutions are the existing solution matrix and these vectors are randomly chosen. The phases are consequently applied for a defined iteration number. The results are updated if the solution of the objective function is lower than the existing one. Thus, the convergence of the optimum results is provided.

3. Numerical Example

In the study, RC columns with different length are optimized. The external loads are taken as 2000 kN, 50 kNm and 50 kN for axial force, flexural moment and shear force, respectively. The optimum results are given in Table 2. Table 2 also contains the results of HS (Bekdaş and Nigdeli, 2014) and BA (Bekdaş and Nigdeli, 2016).

4. Conclusions

The optimum values of RC column are investigated for different length of RC columns. Thus, the slenderness effect can be seen from the optimum results. In all length cases, the external forces are taken as the same but the increase of the total cost does not show a linear increase for long columns. The difference of cost is resulting from the increase of the dimensions and quality of reinforcements. By the increase of the cross-sectional dimensions, a possible reduction of quantity of shear reinforcements can be also seen from the results.

The employed metaheuristic algorithm called TLBO is effective to find the same optimum results with BA. TLBO method has no user defined parameters. The only user defined parameters is the population of the class. The effectiveness of BA is depended to the algorithm parameters. In that case, TLBO is a suitable algorithm in use of methodologies for RC design.

Table 2. Design constant and range.

	HS			BA			TLBO		
Length of the column (l)	3m	4m	5m	3m	4m	5m	3m	4m	5m
Breadth of the column (b_w) (mm)	400	300	300	400	300	300	400	300	300
Height of the column (h) (mm)	400	550	600	400	550	600	400	550	600
Bars in each face	1Φ20+1Φ18	2Φ16	2Φ16	3Φ16	2Φ16	2Φ16	3Φ16	2Φ16	2Φ16
Web reinforcement in each face	1Φ18	1Φ16+1Φ18	2Φ18	1Φ16	1Φ16+1Φ18	2Φ18	1Φ16	1Φ16+1Φ18	2Φ18
Shear reinforcement diameter (mm)	Φ8	Φ8	Φ8	Φ8	Φ8	Φ8	Φ8	Φ8	Φ8
Shear reinforcement distance (mm)	170	240	270	170	240	270	170	240	270
Optimum cost ($)	38.58	52.27	69.97	38.22	52.27	69.97	38.22	52.27	69.97

References

ACI 318M-05 (2005). *Building code requirements for structural concrete and commentary*. American Concrete Institute.

Ahmadkhanlou F, Adeli H (2005). Optimum cost design of reinforced concrete slabs using neural dynamics model. *Engineering Applications of Artificial Intelligence*, 18(1), 65-72.

Akin A, Saka MP (2010). Optimum detailed design of reinforced concrete continuous beams using the harmony search algorithm. In: Topping BHV, Adam JM, Pallarés FJ, Bru R, Romero ML, eds. *Proceedings of the Tenth International Conference on Computational Structures Technology*, Paper 131, Civil-Comp Press, Stirlingshire, UK.

Akin A, Saka MP (2012). Optimum detailing design of reinforced concrete plane frames to ACI 318-05 using the harmony search algorithm. In: Topping BHV, ed. *Proceedings of the Eleventh International Conference on Computational Structures Technology*, Paper 72, Civil-Comp Press, Stirlingshire, UK.

Balling R, Yao X (1997). Optimization of reinforced concrete frames. *Journal of Structural Engineering-ASCE*, 123(2), 193-202.

Barros MHFM, Martins RAF, Barros AFM (2005). Cost optimization of singly and doubly reinforced concrete beams with EC2-2001. *Structural and Multidisciplinary Optimization*, 30(3), 236-242.

Barros AFM, Barros MHFM, Ferreira CC (2012). Optimal design of rectangular RC sections for ultimate bending strength. *Structural and Multidisciplinary Optimization*, 45(6), 845-860.

Bekdaş G, Nigdeli SM (2012). Cost optimization of t-shaped reinforced concrete beams under flexural effect according to ACI 318. *3rd European Conference of Civil Engineering*, Paris, France.

Bekdaş G, Nigdeli SM (2016). Bat algorithm for optimization of reinforced concrete columns. *Joint Annual Meeting of GAMM and DMV*, Braunschweig, Germany.

Bekdaş G, Nigdeli SM (2014). Optimization of slender reinforced concrete columns. *85th Annual Meeting of the International Association of Applied Mathematics and Mechanics*, Erlangen, Germany.

Camp CV, Pezeshk S, Hansson H (2003). Flexural design of reinforced concrete frames using a genetic algorithm. *Journal of Structural Engineering-ASCE*, 129(1), 105-11.

Camp CV, Akin A (2012). Design of retaining walls using big bang–big crunch optimization. *Journal of Structural Engineering-ASCE*, 138(3), 438-448.

Camp CV, Huq F (2013). CO_2 and cost optimization of reinforced concrete frames using a big bang-big crunch algorithm. *Engineering Structures*, 48, 363-372.

Ceranic B, Freyer C, Baines RW (2001). An application of simulated annealing to the optimum design reinfroced concrete retaining structure. *Computers and Structures*, 79(17), 1569-1581.

Coello CC, Hernandez FS, Farrera FA (1997). Optimal design of reinforced concrete beams using genetic algorithms. *Expert Systems with Applications*, 12(1), 101-108.

Fedghouche F, Tiliouine B (2012). Minimum cost design of reinforced concrete T-beams at ultimate loads using Eurocode2. *Engineering Structures,* 42, 43-50.

Ferreira CC, Barros MHFM, Barros AFM (2003). Optimal design of reinforced concrete T-sections in bending. *Engineering Structures*, 25(7), 951-964.

Geem ZW, Kim JH, Loganathan GV (2001). A new heuristic optimization algorithm: harmony search. *Simulation*, 76, 60–68.

Gil-Martin LM, Hernandez-Montes E, Aschheim M (2010). Optimal reinforcement of RC columns for biaxial bending. *Materials and Structures*, 43(9), 1245-1256.

Govindaraj V, Ramasamy JV (2005). Optimum detailed design of reinforced concrete continuous beams using genetic algorithms. *Computers and Structures*, 84(1-2), 34-48.

Govindaraj V, Ramasamy JV (2007). Optimum detailed design of reinforced concrete frames using genetic algorithms. *Engineering Optimization*, 39(4), 471-494.

Guerra A, Kiousis PD (2006). Design optimization of reinforced concrete structures. *Computers and Concrete*, 3(5), 313-334.

Kaveh A, Abadi ASM (2011). Harmony search based algorithms for the optimum cost design of reinforced concrete cantilever retaining walls. *International Journal of Civil Engineering*, 9(1), 1-8.

Kaveh A, Sabzi O (2012). Optimal design of reinforced concrete frames using big bang-big crunch algorithm. *International Journal of Civil Engineering*, 10(3), 189-200.

Lee C, Ahn J (2003). Flexural design of reinforced concrete frames by genetic algorithm. *Journal of Structural Engineering-ASCE*, 129(6), 762-774.

Leps M, Sejnoha M (2003). New approach to optimization of reinforced concrete beams. *Computers and Structures*, 81(18-19), 1957-1966.

Mathworks (2010) MATLAB R2010a. The MathWorks Inc., Natick, MA, USA.

Nigdeli SM, Bekdaş G, Kim S, Geem ZW (2015). A novel harmony search based optimization of reinforced concrete biaxially loaded columns. *Structural Engineering and Mechanics*, 54(6), 1097-1109

Paya I, Yepes V, Gonzalez-Vidosa F, Hospitaler A (2008). Multi objective optimization of concrete frames by simulated annealing. *Computer-Aided Civil and Infrastructure Engineering*, 23, 596-610.

Paya-Zaforteza I, Yepes V, Hospitaler A, Gonzalez-Vidosa F (2009). CO_2-optimization of reinforced concrete frames by simulated annealing. *Engineering Structures*, 31(7), 150-1508.

Perea C, Alcala J, Yepes V, Gonzalez-Vidosa F, Hospitaler A (2008). Design of reinforced concrete bridge frames by heuristic optimization. *Advances in Engineering Software*, 39(8), 676–688.

Rafiq MY, Southcombe C (1998). Genetic algorithms in optimal design and detailing of reinforced concrete biaxial columns supported by a declarative approach for capacity checking. *Computers and Structures*, 69(4), 443-457.

Rajeev S, Krishnamoorthy CS (1998). Genetic algorithm–based methodology for design optimization of reinforced concrete frames. *Computer-Aided Civil and Infrastructure Engineering*, 13, 63-74.

Rama Mohan Rao AR, Shyju PP (2010). A meta-heuristic algorithm for multi-objective optimal design of hybrid laminate composite structures. *Computer-Aided Civil and Infrastructure Engineering*, 25(3), 149-170.

Rao RV, Savsani VJ, Vakharia DP (2011). Teaching–learning-based optimization: a novel method for constrained mechanical design optimization problems. *Computer-Aided Design*, 43(3), 303-315.

Rath DP, Ahlawat AS, Ramaswamy A (1999). Shape optimization of RC flexural members. *Journal of Structural Engineering-ASCE*, 125, 1439-1446.

Sahab MG, Ashour AF, Toropov VV (2005). Cost optimisation of reinforced concrete flat slab buildings. *Engineering Structures*, 27(3), 313-322.

Sirca JG, and Adeli H (2005). Cost optimization of prestressed concrete bridges. *Journal of Structural Engineering-ASCE*, 131(3), 380-388.

Yepes V, Alcala J, Perea C, Gonzalez-Vidosa F (2008). A parametric study of optimum earth-retaining walls by simulated annealing. *Engineering Structures*, 30(3), 821-830.

.

Challenge Journal of Structural Mechanics

Nonlinear finite element analysis of cold-formed steel plain angle columns

Mustafa Durmaz [a,*], Ayşe Daloğlu [b]

[a] *Department of Civil Engineering, Gümüşhane University, 29100 Gümüşhane, Turkey*
[b] *Department of Civil Engineering, Karadeniz Technical University, 61080 Trabzon, Turkey*

ABSTRACT

The main objective of this paper is to provide an efficient and accurate finite element model to understand the behavior of cold-formed steel plain angle columns. The effects of initial local and overall geometric imperfections have been taken into consideration in the analysis. The material nonlinearities of flat and corner portions of the angle sections were incorporated in the model. Failure loads and buckling modes as well as load-shortening curves of plain angle columns were investigated in this study. The nonlinear finite element model was verified against experimental results. The finite element analysis was performed on plain angles compressed between fixed ends over different column lengths, and column curves were obtained.

ARTICLE INFO

Article history:
Received 17 October 2016
Accepted 25 November 2016

Keywords:
Cold-formed steel angles
Columns
Buckling
Nonlinear finite element analysis

1. Introduction

Cold-formed steel structures have many advantages in terms of their superior strength-to-self-weight ratio, ease of construction, and economic design. In recent years, developed manufacture techniques and increased strength of materials gave the edge to cold-formed steel over traditional hot rolled steel in the construction of a wide range of structures (Ellobody and Young, 2005).

Some researchers carried out experimental investigation to study the behavior of cold-formed steel angle columns. Madugula et al. (1983) carried out 16 tests on single equal-leg angles 45x45x3 mm and 65x65x4 mm with hinged end conditions. The nominal slenderness ratios of the test specimens varied from 90 to 250 and comparison of test results with design strengths predicted from different codes of practice was investigated. Popovic et al. (1999) presented the results of 12 fixed-ended and 18 pin-ended compression tests performed on cold-formed plain angle columns. The nominal sizes of angles were 50x50x2.5, 50x50x4, and 50x50x5 with b/t ratios (flat flange width-to-thickness ratio) of 20.6, 12.2, and 9.6, respectively. Young (2004) conducted a series of tests on cold-formed steel plain angle columns compressed between fixed ends. The angle sections were brake-pressed from high strength structural steel sheets and had a b/t ratio ranging from 35.8 to 57.9. The test results were compared with design strengths obtained from the AISI Specification (1996) and AS/NZS standard (1996) for cold-formed steel structures. It is concluded that the design strengths are generally very conservative for all column lengths. Hence design equations for cold-formed steel plain angle columns were proposed.

The behavior of cold-formed steel columns is affected by initial geometric imperfections and residual stresses. Weng and Pekoz (1990) carried out a detailed experimental study of residual stresses effect on the strength of cold-formed steel members. It is found that the residual stress distribution in cold-formed steel sections is different from that in hot-rolled steel sections. Jiao and Zhao (2003) investigated the effect of initial geometric imperfections, residual stresses, and yield slenderness limit on the behavior of very high strength circular steel tubes.

An accurate finite element model is needed to predict the complex behavior of thin-walled structures. It can be quite costly and time consuming for experimental investigation. A detailed finite element study was carried out by Young and Yan (2002) for the analysis and design of fixed-ended plain channel columns. A finite element program ABAQUS was used in the analysis. The four-

* *Corresponding author*. Tel.: +90-456-2331000 ; Fax: +90-456-2337427 ; E-mail address: mustafadurmaz@gumushane.edu.tr (M. Durmaz)
ISSN: 2149-8024 / DOI: http://dx.doi.org/10.20528/cjsmec.2016.11.033

node doubly curved shell element with reduced integration and hourglass control (S4R5) was used in the model. The element has five degrees of freedom per node. The results of the finite element analysis were compared with the results of experimental investigation. Durmaz and Daloğlu (2007, 2009) provided a nonlinear finite element model to investigate the behavior of hot-rolled steel angles subjected to concentric and eccentric axial loads. It was found that the finite element model generally provided good predictions of the experimental failure loads.

The main objective of this paper is to simulate the behavior of cold-formed steel plain angle columns using the finite element method. The finite element program ABAQUS 6.13 (2013) was used in the analysis. The results obtained from the model are verified against test results carried out by Young (2004).

2. Experimental Investigation

2.1. General

The experimental investigation of cold-formed steel plain angle columns performed by Young (2004) provided the experimental ultimate loads and failure modes of columns compressed between fixed ends. The test specimens were brake-pressed from high strength zinc-coated grades G500 and G450 structural steel sheets having nominal yield stresses of 500 and 450 MPa, respectively. Each specimen was cut to a specified length of 250, 1000, 1500,

2000, 2500, 3000 and 3500 mm. Three series of plain angles were tested, having a nominal flange width of 70 mm. The nominal plate thicknesses were 1.2, 1.5, and 1.9 mm. The three series were labeled P1.2, P1.5, and P1.9 according to their nominal thickness. The measured inside corner radius was 2.6 mm for all specimens. The measured cross-section dimensions of the test specimens are detailed in Young (2004).

The Young's modulus (E) was measured as 208, 207, and 208 GPa for Series P1.2, P1.5, and P1.9, respectively. The measured static 0.2% proof stress ($\sigma_{0.2}$) was 550, 530, and 500 MPa for Series P1.2, P1.5, and P1.9, respectively. The initial overall geometric imperfections of the specimens were measured prior to testing. The maximum overall imperfections at mid length were 1/2950, 1/2150, and 1/1970 of the specimen length for Series P1.2, P1.5, and P1.9, respectively. A servo controlled hydraulic testing machine was used to apply compressive axial force to the specimen. The fixed-ended bearings were designed to restrain against the minor and major axis rotations as well as twist rotations and warping.

The initial local geometric imperfections, residual stresses, and corner material properties of the tested plain angle specimens were not reported by Young (2004). However, the values of these measurements are important for finite element analysis. Hence the initial local imperfections, residual stresses, and corner material properties of the angle specimens belonging to the same batch as the column test specimens were measured by Ellobody and Young (2005) and used in this paper.

2.2. Initial local geometric imperfections

Measurements of initial local imperfections were carried out by Ellobody and Young (2005) by using the coordinate measuring machine. A plain angle test specimen of 300 mm in length for Series P1.5 was used for the measurement of local imperfections. The measurements were taken at the middle and quarter lengths of the specimen. Readings were taken at regular intervals and maximum magnitude of local plate imperfection was 0.0021 mm, which is equal to 0.14% of the angle thickness. The same factor was used to predict the initial local geometric imperfections for Series P1.2 and P1.9.

2.3. Residual stresses

The same plain angle specimen used in measuring the initial local geometric imperfections was used by Ellobody and Young (2005) in measuring the residual stresses. The common method to determine the residual stresses is the method of sectioning that requires cutting the plain angle into strips to release the internal residual stresses. By measuring the strains before and after cutting, consequently residual stresses can be determined. The angle specimen was marked into strips of 10 mm width as shown in Fig. 1.

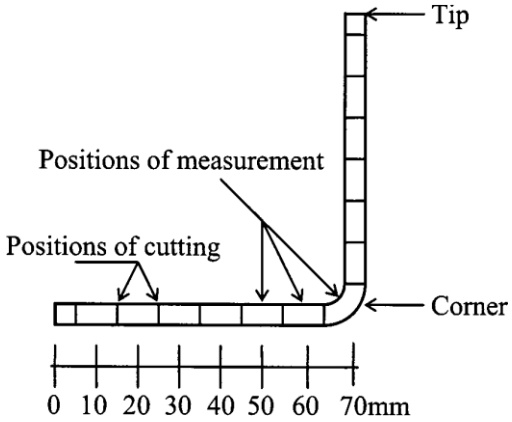

Fig. 1. Positions of wire cutting and measurements for the determination of residual stresses.

Residual stresses are calculated by multiplying residual strains by Young's modulus of the test specimen of Series P1.5. Table 1 summarizes the membrane and bending residual strains at the measurement sections with reference to the plain angle tip. The distribution of membrane and bending residual stresses in the cross section of the test specimen is shown in Fig. 2.

2.4. Material properties

The material properties in the corner of the angle section were determined for Series P1.5 by Ellobody and Young (2005) by carrying out a tensile coupon test. The corner coupon specimen was taken from the corner strip after the wire cutting of the specimen used to measure the residual stresses. The corner coupon specimen was curved before testing, and the effect of bending residual

stresses is included in the stress-strain curve of the corner tensile coupon test. The material properties of the corners of Series P1.2 and P1.9 were extrapolated from the material properties of the Series P1.5 according to the measured 0.2% tensile proof stress ($\sigma_{0.2}$) in the flat portions of each series. The measured and predicted material properties of the corner coupons can be summarized as follows: Young's modulus (E) of 203 GPa for the three series. The static 0.2% proof stress ($\sigma_{0.2}$) was 635, 610, and 575 MPa for Series P1.2, P1.5, and P1.9, respectively. The tensile strain after fracture (ε_u) was 3% for the three tests series.

Table 1. Measured membrane and bending residual strains for series P1.5.

Distance from tip (mm)	Membrane strain (μstrain)	Bending strain (μstrain)
10	75	125
20	115	235
30	260	420
40	300	520
50	210	540
60	75	395
70 (corner)	-460	-940

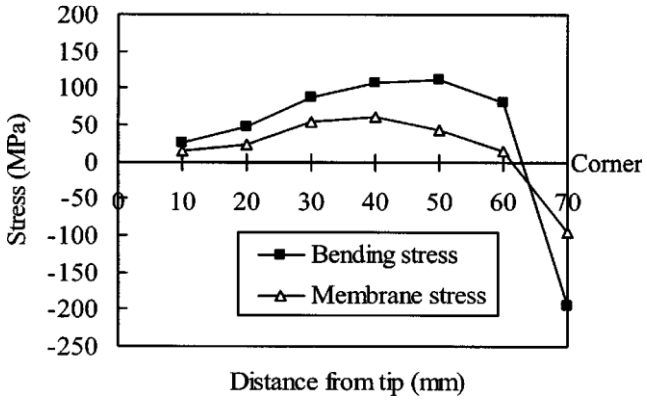

Fig. 2. Distribution of membrane and bending residual stresses along the cross section of Series P1.5.

3. Finite Element Modeling

3.1. General

In this study, the finite element program (ABAQUS, 2013) was used in the analysis of plain angle columns tested by Young (2004). The model used the nominal sizes, initial local and overall geometric imperfections, residual stresses, and material properties. Finite element analysis for buckling requires two types of analyses. The first is known as eigenvalue analysis that estimates the buckling modes and loads. Such an analysis is a linear elastic analysis performed using the (*BUCKLE) procedure available in the ABAQUS library with the live load applied within the step. The buckling analysis provides the factor by which the live load must be multiplied to reach the buckling load. For practical purposes, only the lowest buckling mode predicted from the eigenvalue analysis is used. The second is called load-displacement nonlinear analysis and follows the eigenvalue prediction. It is necessary to consider whether the post buckling response is stable or unstable.

3.2. Finite element type and mesh

It is mentioned in the ABAQUS manual that the four-noded doubly curved shell element with reduced integration S4R is suitable for complex buckling behavior (ABAQUS, 2013; Nandula, 1998; Young, 2004). The S4R element has six degrees of freedom per node and provides accurate solutions to most applications. The element also accounts for finite strain and is suitable for large strain analysis. Since buckling of plain angle columns is very sensitive to large strains, the S4R element was used in this study to ensure the accuracy of the results. In order to choose the finite element mesh that provides accurate results with minimum computational time, convergence studies were conducted. It is found that a 10 mm x 10 mm (length by width) ratio provides adequate accuracy in modeling the angles.

3.3. Boundary conditions and load application

Following the testing procedures for Series P1.2, P1.5, and P1.9, the ends of the columns were fixed against all degrees of freedom except for the displacement at the loaded end in the direction of the applied load. The nodes other than the two ends were free to translate and rotate in any direction. The load was applied in increments using the modified RIKS method available in the ABAQUS library. The RIKS method is generally used to predict unstable and nonlinear collapse of a structure such as post buckling analysis. It uses the load magnitude as an additional unknown and solves simultaneously for loads and displacements. The load was applied as static uniform loads at each node of the loaded end which is identical to the experimental investigation. The nonlinear geometry parameter (*NLGEOM) was included to deal with the large displacement analysis.

3.4. Material modeling

The measured stress-strain curves for flat portions of Series P1.2, P1.5, and P1.9 were used in the analysis. In addition, the measured and predicted stress-strain curves of the corner coupons for the same series were used. The material behavior provided by ABAQUS allows for a multilinear stress-strain curve to be used. The first part of the multilinear curve represents the elastic part up to the proportional limit stress with measured Young's modulus and Poisson's ratio equal to 0.3. Since the analysis of post buckling involves large inelastic strains, the nominal (engineering) static stress-strain curve was converted to a true stress and logarithmic plastic strain curve. The true stress (σ_{true}) and plastic true strain ($\varepsilon^{pl}{}_{true}$) were calculated using Eqs. (1) and (2).

$$\sigma_{true} = \sigma(1+\varepsilon)\,, \tag{1}$$

$$\varepsilon^{pl}_{true} = \ln(1+\varepsilon) - \sigma_{true}/E\,, \tag{2}$$

where E is Young's modulus while σ and ε are measured nominal (engineering) stress and strain values.

3.5. Modeling of initial local and overall geometric imperfections

Cold-formed steel plain angle columns with very high b/t ratio are likely to fail by pure local buckling. On the other hand, columns with very low b/t ratio are likely to fail by overall buckling. Both initial local and overall geometric imperfections are found in columns as a result of the fabrication process. Hence superposition of local buckling mode as well as overall buckling mode with measured magnitudes is recommended for accurate finite element analysis (Ellobody and Young, 2005). These buckling modes can be obtained by carrying eigenvalue analysis of the column with very high b/t ratio and very low b/t ratio to ensure local and overall buckling occurs, respectively. Only the lowest buckling mode (eigenmode 1) is used in the eigenvalue analysis. This technique is used in this study to model the initial local and overall imperfections of the columns. Since all buckling modes predicted by ABAQUS eigenvalue analysis are generalized to 1.0, the buckling modes are factored by the measured magnitudes of the initial local and overall geometric imperfections (Young and Yan, 2002).

3.6. Modeling of residual stresses

To ensure accurate modeling of the behavior of plain angle columns, the residual stresses were included in the finite element model although their effect on the ultimate capacity is considered to be small (Schafer and Pekoz, 1998; Gardner, 2002). Measured residual stresses are implemented in the finite element model by using the ABAQUS (*INITIAL CONDITIONS, TYPE=STRESS) parameter. Only the membrane residual stresses were modeled in this study.

4. Results and Discussion

In the verification of the finite element model, a total of 21 cold-formed steel plain angle columns were analyzed. A comparison between the experimental results and the results of the finite element model is carried out. The main objective of this comparison is to verify and check the accuracy of the finite element model. The comparison of the ultimate loads P_{test} and P_{FEM} are shown in Table 2. Fig. 3 plotted the relationship between the ultimate load and the column effective length $L_{eff}=L/2$ for angles reported by Young (2004), where L actual column length. The column curves show the experimental ultimate loads together with that obtained by the finite element method. It can be seen that good agreement has been achieved between both results for most of the columns.

Table 2. Comparison between test and FE results.

Specimen	P_{test} (kN)	P_{FEM} (kN)	P_{test}/P_{FEM}
P1.2L250	23.80	30.30	0.79
P1.2L1000	18.70	22.62	0.83
P1.2L1500	15.20	16.86	0.90
P1.2L2000	12.60	12.11	1.04
P1.2L2500	11.60	10.83	1.07
P1.2L3000	8.00	8.40	0.95
P1.2L3500	5.80	5.91	0.98
Mean			0.937
COV			0.011
P1.5L250	39.60	44.29	0.89
P1.5L1000	31.00	34.32	0.90
P1.5L1500	25.20	25.80	0.98
P1.5L2000	17.50	18.61	0.94
P1.5L2500	15.70	15.63	1.00
P1.5L3000	13.10	13.01	1.01
P1.5L3500	11.50	11.41	1.01
Mean			0.962
COV			0.002
P1.9L250	57.70	62.86	0.92
P1.9L1000	47.80	53.37	0.90
P1.9L1500	35.60	37.10	0.96
P1.9L2000	27.10	29.38	0.92
P1.9L2500	22.40	24.49	0.91
P1.9L3000	14.80	20.04	0.74
P1.9L3500	14.40	16.16	0.89
Mean			0.891
COV			0.005

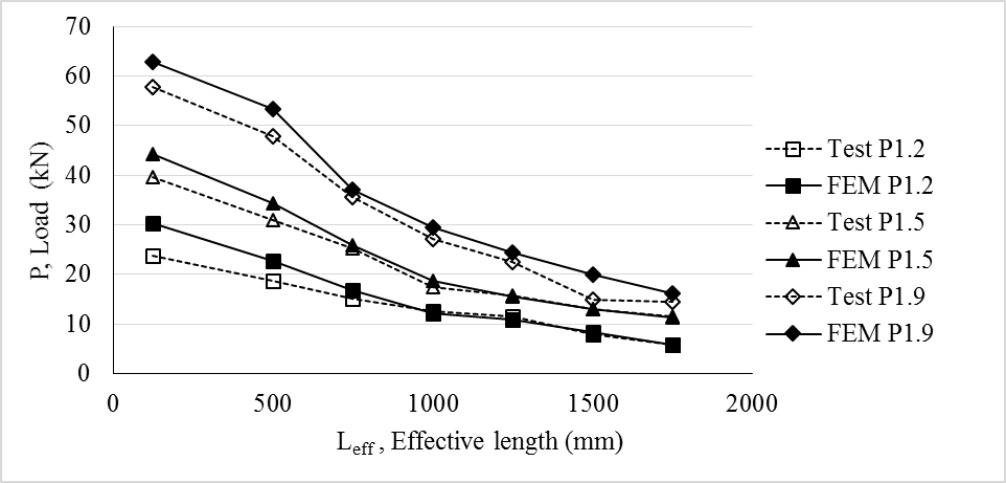

Fig. 3. Ultimate loads of plain angle columns for Series P1.2, P1.5, and P1.9.

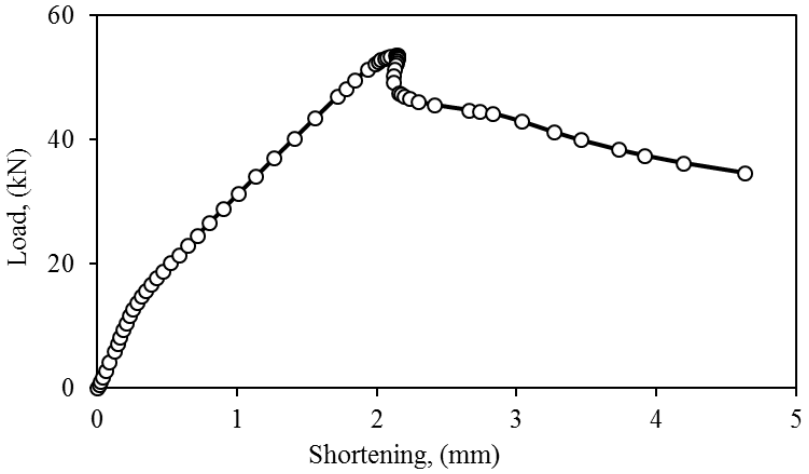

Fig. 4. Load-axial shortening curve for P1.9L1000.

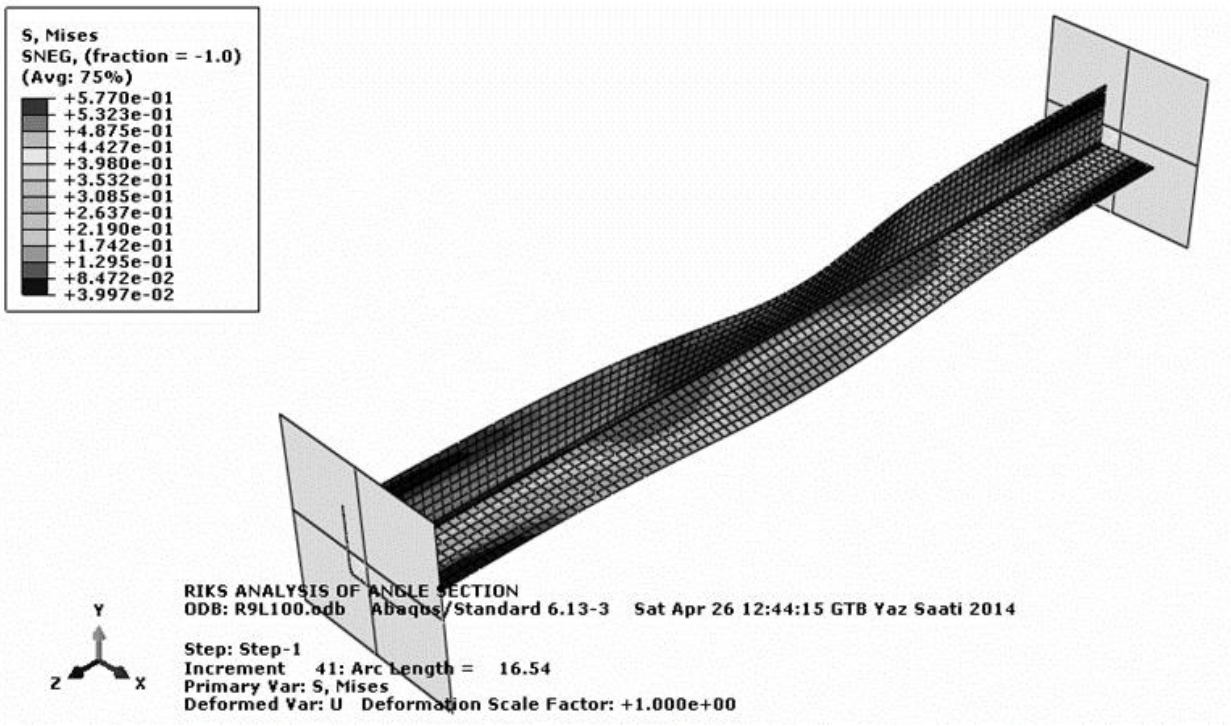

Fig. 5. Failure mode of column P1.9L1000.

5. Conclusions

This paper provides an efficient finite element model for the analysis of cold-formed steel plain angle columns. The initial local imperfections, residual stresses, and corner material properties of the cold-formed steel angle test specimens have been measured and reported in this paper. The finite element model includes initial local and overall geometric imperfections and residual stresses. Nonlinear material properties of flat and corner portions of plain angle columns are also considered in the analysis. The comparison between the finite element results and the experimental investigation of 21 columns with different geometric dimensions showed good agreement in predicting the columns behavior. The column strengths, load-shortening behavior, and failure modes have been predicted using the finite element model and compared well with the experimental results.

Acknowledgements

The work described in this paper was supported by the Research Foundation of Gümüşhane University. The authors would like to gratefully acknowledge this support. (Project No. 13.F5110.02.06)

References

ABAQUS (2013). Standard User's Manual. Hibbit, Karlsson and Sorensen, Inc., Vols. 1, 2 and 3, Version 6.13.

American Iron and Steel Institute (AISI) (1996). Specification for the Design of Cold-Formed Steel Structural Members, Washington, D.C.

Australian/New Zealand Standard (AS/NZS) (1996). Cold-Formed Steel Structures, AS/NZS 4600:1996, Standards Australia, Sydney, Australia.

Durmaz M, Daloğlu A (2007). Merkezi yüklü korniyerlerin yük taşıma kapasiteleri. *2nd Steel Structures Symposium*, TMMOB Chamber of Civil Engineers, Eskişehir. (in Turkish)

Durmaz M, Daloğlu A (2009). Eksantrik yüklü korniyerlerin yük tasıma kapasiteleri. *3th Steel Structures Symposium*, TMMOB Chamber of Civil Engineers, Gaziantep. (in Turkish)

Ellobody E, Young B (2005). Behavior of cold formed steel plain angle columns. *Journal of Structural Engineering*, 131(3), 457-466.

Gardner L (2002). A New Approach to Structural Stainless Steel Design, *Ph.D. Thesis*, Department of Civil and Environmental Engineering, Imperial College of Science, Technology and Medicine, London.

Jiao H, Zhao XL (2003). Imperfections, residual stress and yield slenderness limit of very high strength (VHS) circular steel tubes. *Journal of Constructional Steel Research*, 59, 233–249.

Madugula MKS, Prabhu TS, Temple MC (1983). Ultimate strength of concentrically loaded cold-formed angles. *Canadian Journal of Civil Engineering*, 10, 60–68.

Nandula R (1998). Finite Element Analysis of Eccentrically Loaded Angles, *M.Sc. Thesis*, University of Windsor, Windsor, Ontario, Canada.

Popovic D, Hancock GJ, Rasmussen KJR (1999). Axial compression tests of cold-formed angles. *Journal of Structural Engineering*, 125(5), 515–523.

Schafer BW, Pekoz T (1998). Computational modeling of cold formed steel: Characterizing geometric imperfections and residual stresses. *Journal of Constructional Steel Research*, 47, 193–210.

Weng CC, Pekoz T (1990). Residual stresses in cold-formed steel members. *Journal of Structural Engineering*, 116(6), 1611–1625.

Young B (2004). Tests and design of fixed-ended cold-formed steel plain angle columns. *Journal of Structural Engineering*, 130(12), 1931–1940.

Young B, Yan J (2002). Finite element analysis and design of fixed-ended plain channel columns. *Finite Element Analysis and Design*, 38, 549–566.

Challenge Journal of Structural Mechanics

Wind loads for stadium lighting towers according to Eurocode 1

Zeki Karaca [a], Hasan Tahsin Öztürk [b], Erdem Türkeli [c,*]

[a] *Department of Civil Engineering, Ondokuz Mayıs University, 55139 Samsun, Turkey*
[b] *Department of Civil Engineering, Of Technology Faculty, Karadeniz Technical University, 61830 Trabzon, Turkey*
[c] *Ordu Provincial Organization of Ministry of Environment and Urban Planning, 52100 Ordu, Turkey*

ABSTRACT

The determination of actions on structures is an important step of in the design process. In nature, so many outer and inner actions are acting on structures continuously. The two most important ones of those actions are the earthquake and wind actions. For some structures, i.e. towers, high chimneys or lighting towers, the priority of these two severe actions can change. Wind forces can become a governing force on the design of these structures. Therefore, the determination of wind forces for these tall, slender and wind-sensitive structures becomes very important. Also, these tall and slender structures have a high ratio of height to least diameter that makes them more slender and wind-sensitive than any other structures. In this study, the determination of wind loads for a selected and modeled stadium lighting tower was given according to Eurocode 1 which is an international well-known standard. This study showed that it is difficult to calculate wind loads of stadium lighting towers according to Eurocode 1 because of the complexity of the document, insufficient explanation of some formulas like resonant response factor and unclear graph sections for the reader. This study is believed to enlighten the way of the users of Eurocode 1.

ARTICLE INFO

Article history:
Received 18 October 2016
Accepted 4 December 2016

Keywords:
Stadium
Lighting
Tower
Eurocode 1
Wind

1. Introduction

Stadium lighting towers are generally used for lighting of the sport stages at dark during sport events. Four stadium lighting towers lighting a stadium during a football match were shown in Fig. 1.

The characteristic natural properties of these structures are: lightweight when compared to other structures, easily erectable, high cost efficiency, high aspect ratio (ratio of total length to least diameter), slender and wind sensitive (Chien and Jang, 2010). Also, it was stated by Abdullah (2011) that tall, slender and flexible structures such as towers, chimneys, masts are prone to wind action. In recent years, several failures of HMS towers have brought to light the need for a better understanding of the complex behavior of these structures (Warpinski et al., 2010). Collapse of these tall steel cantilever structures showed the importance of the right determination of wind loads acting to them. In Fig. 2, the base of a collapsed lighting tower due to wind loads was shown (Repetto and Solari, 2010).

Structural properties i.e. total height of the lighting tower, the strength of materials used for the construction, number of lighting bulbs used are different for different stadiums in different countries of the world. Lighting bulbs are mounted on top of the tower. Angle of lighting bulbs with the vertical, number and brightness of lighting bulbs are determined according to the needs of the stadium.

The objective of this paper is to determine the along-wind loads for stadium lighting towers according to Eurocode 1. For this purpose, a stadium lighting tower that has 20 meters height (Fig. 3) was modeled in SAP2000 (Wilson, 2000) and wind loads acting to this structure were calculated.

2. Calculation of Along-Wind Forces according to Eurocode 1 (CEN, 2004)

Eurocode 1 (CEN, 2004) deals with buildings and civil engineering works with heights up to 200 m. There are

* *Corresponding author*. Tel.: +90-452-2339588 ; Fax: +90-452-2332508 ; E-mail address: erdem18turkeli@hotmail.com (E. Türkeli)
ISSN: 2149-8024 / DOI: http://dx.doi.org/10.20528/cjsmec.2016.12.035

so many tables, formulas and figures in the wind load calculation procedure for the use of people using this standard in their calculations. Moreover, mean wind speed is not taken from a table or a chart. It is calculated from the basic wind velocity and the fundamental value of the basic wind velocity.

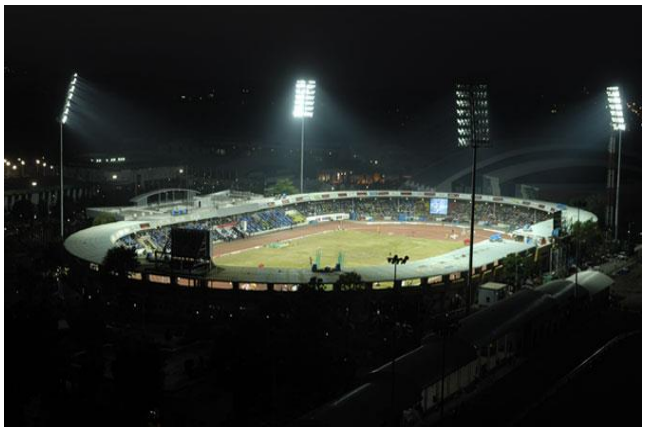

Fig. 1. Four stadium lighting towers (Bajaj Electricals, 2013).

Fig. 2. Base of collapsed steel lighting tower (Repetto and Solari, 2010).

In this part of the study, it is aimed to give only brief information about the procedure used in the calculation of along-wind loads according to Eurocode 1. The across-wind forces are not in the scope of this paper. Eurocode 1 is open to the use of the public. Therefore, there is no need to give detailed calculation procedures of the standard for the purpose of the volume limitation of the study.

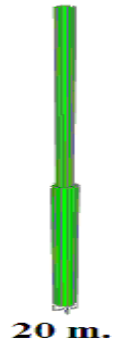

Fig. 3. SAP2000 model of 20 meters high stadium lighting tower (Wilson, 2000).

Total wind load which is shown in Eq. (1) is the combination of structural factor, the force coefficient, peak velocity pressure and the reference area for the structure. This standard also deals with the turbulence intensity in the calculation of peak velocity pressure. The most difficult parameter to calculate in the wind load formula is the structural factor because it contains the resonant part and the resonant part has so many parameters in it. Another difference used in this standard is the use of Reynolds number in the determination of force parameter. Moreover, tables and figures are used for the selection of relevant information.

$$F_w = c_s c_d \cdot c_f \cdot q_p(Z_e) \cdot A_{ref} \,. \tag{1}$$

The detailed procedure for calculating the structural factor $c_s c_d$ is given in Eq. (2);

$$C_s C_d = \frac{1+2 \cdot k_p \cdot I_v(z_e) \cdot \sqrt{B^2+R^2}}{1+7 \cdot I_v(z_e)} . \tag{2}$$

In Eq. (2), z_e is expressing the reference height, k_p is expressing the peak factor defined as the ratio of the maximum value of the fluctuating part of the response to its standard deviation, I_v is expressing the turbulence intensity, B^2 is expressing the background factor and R^2 is expressing the resonance response factor (Handa, 2006) given in Eq. (3). It is on the safe side to use B^2 =1.

$$R^2 = \frac{2 \cdot \pi . F . \varphi_b \cdot \varphi_h}{\delta_s + \delta_a} . \tag{3}$$

In Eq. (3), F is expressing Wind Energy Spectrum, $\emptyset_b$ is expressing the size effect (breadth of the building), $\emptyset_h$ is expressing size effect (height of the building), δ_s is expressing the structural damping expressed by the logarithmic decrement and δ_a is expressing aerodynamic damping. The force coefficient c_f for a finite circular cylinder should be determined from Eq. (4);

$$c_f = c_{f,0} \cdot \psi_\lambda \,. \tag{4}$$

In Eq. (4), $c_{f,0}$ is expressing the force coefficient of cylinders without free-end flow and ψ_λ is expressing end-effect factor. The parameter $c_{f,0}$ given in Eq.(4) can be found by using the graph given in Eurocode 1. Also, peak velocity pressure $q_p(z)$ can be calculated by using Eq. (5);

$$q_p(z) = [1 + 7 \cdot I_V(z)] \cdot \frac{1}{2} \cdot p \cdot V_m^2(z)\,. \quad (5)$$

ρ, $V_m(z)$ and $I_v(z)$ are impending air density, mean wind velocity and turbulence intensity, respectively.

3. General Structural and Mechanical Information about the Stadium Lighting Tower

A 20 meters high stadium lighting tower was constituted from 10 meters high pole sections with section splices. The finite element model (FEM) of the tower (Fig. 3) was created in Structural Analysis Program SAP2000. By using the structural information given in Table 1, two dimensional linear dynamic analyses were carried out.

The FEM model of 20 meters high stadium lighting tower was developed from non-prismatic circle sectioned steel bars. Steel has unit mass, unit weight, the module of elasticity and Poisson ratio, 7.849 kN.s^2/m^4, 76.973 kN/m^3, 200,000 MPa and 0.3 respectively. During SAP2000 dynamic analyses, some assumptions were made: all splice points have three degree of freedoms namely 2 translational and 1 rotational, base was fixed to the ground, effect of earthquakes and lighting bulbs and relevant equipment ignored, tower was constructed on sea or coastal area exposed to open sea, no effect of other structures to the direction of wind, no holes on outer or inner surfaces of the tower.

Table 1. Structural information of 20 meters high stadium lighting tower.

Section No	Section No	Outside Diameter (mm)	Wall Thickness (mm)	Inside Diameter (mm)
	Height (m)	20	20	20
0	0	1200	5	1190
1	10	800	5	790
2	20	400	4	392

4. Calculation of Along-Wind Loads for 20 meters high Stadium Lighting Tower according to Eurocode 1

The fundamental value of the basic wind velocity according to logarithmic law for 20 meters high tower was given in Table 2.

In Table 2, the fundamental value of the basic wind velocity was selected as 36.00 m/s. The value of basic wind velocity was given in Table 3. In Table 3, directional & seasonal factors were given as 1.0.

The terrain factor used in the calculation of roughness factor was given in Table 4. In Table 4, according to Eurocode 1, z_0 and $z_{0,11}$ values were selected as 0.003 and 0.050, respectively. Also, in Table 5, the roughness factor was calculated depending on the terrain factor.

After calculation of basic wind velocity and the roughness factor, the mean wind velocity was calculated in Table 6.

The turbulence intensity was calculated in Table 7. Also, the size effects for breadth and height of the 20 meters high lighting tower were given in Table 8 and 9, respectively.

The value of the non-dimensional frequency was given in Table 10 and the value of the wind-energy spectrum according to non-dimensional frequency was given as Table 11. The value of peak velocity pressure was calculated and given in Table 12.

Table 2. The fundamental value of the basic wind velocity according to logarithmic law.

Section No	Height from Ground (m)	H_0 (m)	z_0 (m)	$\ln(H/z_0)$	$\ln(H_0/z_0)$	$\frac{\ln(H/z_0)}{\ln(H_0/z_0)}$	V_0 (m/s)	$V_{b,0}$ (m/s)
0	0	10.000	0.003	0.000	8.112	0.000	36.000	0.000
1	10	10.000	0.003	8.112	8.112	1.000	36.000	36.000
2	20	10.000	0.003	8.805	8.112	1.085	36.000	39.076

Table 3. The value of the basic wind velocity.

Section No	Height from Ground (m)	$V_{b,0}$ (m/s)	C_{dir}	C_{season}	V_b (m/s)
0	0	0.000	1.000	1.000	0.000
1	10	36.000	1.000	1.000	36.000
2	20	39.076	1.000	1.000	39.076

Table 4. The terrain factor.

z_0 (m)	$z_{0,11}$ (m)	$0{,}19*(z_0/z_{0,11})^{0{,}07}$	k_r
0.003	0.050	0.156	0.156

Table 5. The roughness factor.

Section No	Height from Ground (m)	z_0 (m)	$\ln(z/z_0)$	k_r	$C_r(z)$
0	0	0.003	5.809	0.156	0.906
1	10	0.003	8.112	0.156	1.266
2	20	0.003	8.805	0.156	1.374

Table 6. The mean wind velocity.

Section No	Height from Ground (m)	$C_r(z)$	$C_0(z)$	V_b (m/s)	$V_m(z)$ (m/s)
0	0	0.906	1.000	0.000	0.000
1	10	1.266	1.000	36.000	45.566
2	20	1.374	1.000	39.076	53.686

Table 7. The turbulence intensity.

Section No	Height from Ground (m)	k_l	$C_0(z)$	$\ln(z/z_0)$	$I_v(z)$
0	0	1.000	1.000	5.809	0.172
1	10	1.000	1.000	8.112	0.123
2	20	1.000	1.000	8.805	0.114

Table 8. The size effect for breadth of the structure.

Outer Diameter at top of the Tower (m)	First Mode Natural Frequency (Hz)	Mean Wind Speed at top (m/s)	$Ø_b$
0.400	2.618007	53.686	0.941

Table 9. The size effect for height of the structure.

Height of the Lighting Tower (m)	First Mode Natural Frequency (Hz)	Mean Wind Speed at top (m/s)	$Ø_h$
20.000	2.618007	53.686	0.339

Table 10. The value of non-dimensional frequency.

Section No	Height From Ground (m)	Reference Length Scale (m)	Reference Height (m)	α	Turbulence Length Scale (m)	First Mode Natural Frequency (Hz)	Mean Wind Speed at top (m/s)	C
0	0	300	200	0.380	40.159	2.618	53.686	1.958
1	10	300	200	0.380	96.233	2.618	53.686	4.693
2	20	300	200	0.380	125.193	2.618	53.686	6.105

Table 11. The wind-energy spectrum.

Section No	Height from Ground (m)	C	F
0	0	1.958	0.073
1	10	4.693	0.041
2	20	6.105	0.034

Table 12. Peak velocity pressure.

Section No	Height from Ground (m)	$I_v(z)$	ρ (kg/m^3)	$V_m(z)$ (m/s)	$q_p(z)$ (kg/m.s^2)
0	0	0.172	1.250	0.000	0.000
1	10	0.123	1.250	45.566	2417.469
2	20	0.114	1.250	53.686	3233.459

The value of peak velocity pressure in Table 12 was dependent on turbulence intensity given in Table 7, density of air (taken as 1.25 kg/m^3) and mean wind velocity given in Table 6. Also, the Reynolds number for circular cylinders was given in Table 13. In Table 13, z_e is the reference height which is 60% of the total height given in Eurocode 1. Also, the kinematic viscosity in Eurocode 1 was given as 0.000015 m^2/s.

The force coefficient dependent on Reynolds number and k/b ratio was given in Table 14. Also, end-effect factor can be selected from the figure given in Eurocode 1 by using solidity ratio and effective slenderness. The end-effect factor was given in Table 15.

In Table 15, the effective slenderness from the interpolation was found as 40. Also, the solidity ratio for the steel cantilever structure was found as 1.00 because there is no spacing on the body of the structure. The force coefficient dependent on the force coefficient of cylinders without free-end flow given in Table 14 and end-effect factor given in Table 15 was calculated in Table 16.

The equivalent mass per unit length for the upper third of the 20 meters high stadium lighting tower was given in Table 17. From the definition m_e, it may be approximated by the average value of m over the upper third of the structure.

By using the equivalent mass per unit length given in Table 17, the logarithmic decrement of aerodynamic damping was given in Table 18. Also, the resonant response part was calculated in Table 19. Structural damping was given as 0.05 for steel structures. Also, the up-crossing frequency for peak factor and the peak factor dependent on up-crossing frequency was given in Table 20 and 21, respectively.

Peak factor, k_p was selected as the greater of the values given in grey color in Table 21. Also, the structural factor was given in Table 22. In Table 22, the background factor B^2 is recommended to use as 1.0.

The total along-wind loading per unit length on 20 meters high HMS lighting tower was calculated in Table 23. The reference areas were calculated as the projection of the areas swept by the wind. This area is a trapezoid.

Table 13. Reynolds number for circular cylinders.

Section No	Height from Ground (m)	Diameter of the Section (m)	$V_m(z_e)$ (m/s)	N (m^2/s)	Re
0	0	1.200	46.590	0.000015	3.7*10^6
1	10	0.800	46.590	0.000015	2.4*10^6
2	20	0.400	46.590	0.000015	1.2*10^6

Table 14. The force coefficient of cylinders without free-end flow.

Section No	Height from Ground (m)	Diameter of the Section (m)	Equivalent Roughness (mm)	k/b	Re	$C_{f,0}$
0	0	1.200	0.200	0.0001666667	3.7*10^6	*0.000*
1	10	0.800	0.200	0.0002500000	2.4*10^6	*0.796*
2	20	0.400	0.200	0.0005000000	1.2*10^6	*0.801*

Table 15. The end-effect factor.

Section No	Height From Ground (m)	l	b	$0{,}7*l/b$	λ	$\lambda_{interpolation}$	A	A_c	$\varphi=A/A_c$	ψ_λ
0	0	20.000	0.400	35.000	70.000	40.000	...	...	0.000	0.000
1	10	20.000	0.400	35.000	70.000	40.000	10.000	10.000	1.000	0.830
2	20	20.000	0.400	35.000	70.000	40.000	6.000	6.000	1.000	0.830

Table 16. The force coefficient.

Section No	Height from Ground (m)	$C_{f,0}$	ψ_λ	C_f
0	0	0.000	0.000	0.000
1	10	0.796	0.830	0.660
2	20	0.801	0.830	0.665

Table 17. The equivalent mass per unit length.

Section No	Height From Ground (m)	Outside Diameter of the Section (m)	Inside Diameter of the Section (m)	Wall Thickness of the Section (mm)	Volume of the Section (m^3)	Mass Per Unit Volume (kg/m^3) (steel)	Mass of the Section (kg)	m_e (kg/m)
0	0	1.200	1.190	5.000	...	800.000	0.000	...
1	14	0.640	0.630	5.000	...	800.000	0.000	...
2	20	0.400	0.392	4.000	0.044	800.000	35.570	5.928

Table 18. The logarithmic decrement of aerodynamic damping.

Section No	Height From Ground (m)	C_f	ρ (kg/m^3)	Top Mean Wind Speed (m/s)	Outer Diameter at top (m)	m_e (kg/m)	1st Mode Natural Frequency (Hz)	δ_a
0	0	0.000	1.250	53.686	0.400	5.928	2.618007	0.000
1	10	0.660	1.250	53.686	0.400	5.928	2.618007	1.142
2	20	0.665	1.250	53.686	0.400	5.928	2.618007	1.150

Table 19. The resonant response part.

Section No	Height From Ground (m)	F	$\emptyset_b$	$\emptyset_h$	δ_s	δ_a	R^2
0	0	0.073	0.941	0.339	0.050	0.000	...
1	10	0.041	0.941	0.339	0.050	1.142	0.069
2	20	0.034	0.941	0.339	0.050	1.150	0.057

Table 20. The up-crossing frequency.

Section No	Height from Ground (m)	B^2	R^2	First Mode Natural Frequency (Hz)	ν
0	0	1.000	...	2.618007	...
1	10	1.000	0.069	2.618007	0.664
2	20	1.000	0.057	2.618007	0.610

Table 21. The peak factor.

Section No	Height from Ground (m)	ν	k_p	k_p
0	0	...	3.000	...
1	10	0.664	3.000	3.628
2	20	0.610	3.000	3.605

Table 22. The structural factor.

Section No	Height from Ground (m)	k_p	$I_v(z_e)$	R^2	B^2	$c_s c_d$
0	0	...	0.118	...	1.000	...
1	10	3.628	0.118	0.069	1.000	1.032
2	20	3.605	0.118	0.057	1.000	1.027

Table 23. The total along-wind load on 20 meters high stadium lighting tower.

Section No	Height from Ground (m)	$c_s c_d$	C_f	$q_p(z)$	A_{ref}	F_w (kN/m)
0	0	...	0.000	0.000	...	0.000
1	10	1.032	0.660	2417.469	10.000	1.648
2	20	1.027	0.665	3233.459	6.000	1.324

5. Conclusions

In this study, along-wind forces acting on 20 meters high stadium lighting tower according to Eurocode 1 were calculated. The FEM of 20 meters high stadium lighting tower was developed in SAP2000 and the wind loading calculations were performed step by step in tabular form. Due to the fact that Eurocode 1 is open to the use of public and the volume limitation of this study, there is no need to provide all detailed along-wind calculation procedures given in Eurocode 1. Therefore, only the relevant equations were given in the preceding parts of the study. Some of the results, discussions and suggestions deducted from the study were given as follows:

From Table 23, it can be clearly seen that although wind speed increases with height, the wind loading on the stadium lighting tower is not increasing with the increase in height due to decreasing wind affected area because of their trapezoidal (projection) geometry. The calculation of resonant response factor in Eurocode 1 is so complex and difficult. Therefore, in this study, an explanatory additional equation was provided for resonant response factor. In Eurocode 1, the calculation of force coefficient is dependent on a graph (not given in this study due to the volume limitation) which is constructed from two different equations. It is very difficult and time consuming for the users to directly select the value from the graph due to illegible closer values. Also, directly usage of these two different equations is time consuming. Therefore, the graph for the calculation of force coefficient should be enhanced and clarified for the users. Moreover, end-effect factor given in Table 15 was determined by using the graph (not given in this study due to the volume limitation) in Eurocode 1. There is no scale or any other provided intermediate values on this graph. Therefore, the obtained values for end-effect factor are depending on the ability of the user. Even for the same values of solidity ratio and effective slenderness, different users can find different values of end-effect factor. This phenomenon leads wind loads to differ from each other. A research study can be made to clarify the use of this graph.

This study is only dealt with the along-wind loading calculation of a 20 meters high stadium lighting tower according to Eurocode 1. The effect of earthquakes, across-wind forces (wind induced forces), divergence or flutter, galloping, wake buffeting are not considered and not taken into account. In the design of stadium lighting towers, it is advised to determine all of governing forces in order to design and construct safer stadium lighting towers.

References

Abdullah RM (2011). Wind load effects on concrete tower during construction. *European Journal of Scientific Research*, 54(3), 339-346.

Bajaj Electricals (2013). Stadium Lighting. Bajaj Electricals Ltd., http://www.bajajelectricals.com/stadium-lighting.aspx. Downloaded on 02-07-2013.

CEN TC 250 (2004). prEN 1991-1-4, *Eurocode 1: Actions on Structures-General Actions- Part1-4: Wind Actions*.

Chien CW, Jang JJ, Li YC (2010). Wind-Resistant design of high mast structures. *Journal of the Chinese Institute of Engineers*, 33(4), 597-615.

Handa K (2006). European Standard for Wind Loads Notes (Eurocode EN 1991-1-4 WIND ACTIONS).

Repetto MP, Solari G (2010). Wind-induced fatigue collapse of real slender structures. *Engineering Structures*, 32, 3888-3898.

Warpinski MK, Connor RJ and Hodgson IC (2010). Influence of flexibility on the fatigue performance of the base plate connection in high-mast lighting towers. *Journal of Structural Engineering,* 136(3), 324-329.

Wilson EL (2000). SAP2000: Integrated finite element analysis and design of structures. *Computers and Structures*, Berkeley, CA.

Challenge Journal of Structural Mechanics

Soft-story effects on the behaviour of seismically isolated buildings under near and far-fault earthquakes

Savaş Erdem *, Khalid Saifullah

Department of Civil Engineering, İstanbul University, 34320 Istanbul, Turkey

ABSTRACT

In this study, the effects of soft-story on the seismic behaviour of 3-story and 8-story isolated buildings under near and far-fault earthquakes were investigated. Four different structural models with two different 1st story height were designed: One with 1st story height of 3m and 2nd with 1st story height of 4.5m to capture soft story effect. The prototype fixed base buildings were converted to seismically isolated buildings by introducing rubber isolators at base level. Analyses were conducted by using two different isolation systems (QW7.5Tb3 and QW7.5Tb4). The modelling of conventional fixed base prototype seismically isolated buildings and their modal analyses were conducted on finite-element program SAP2000, whereas, modelling of seismically isolated buildings and nonlinear time-history analyses were conducted using 3D-BASIS program. The four accelerations records has been used for the time-history analysis. Floor accelerations, story shears and inter-story drift ratios were the key structural responses considered. The analysis results showed seismic isolations can be used as a viable mitigation method for the buildings with soft-stories under near and far-fault earthquakes. Based on the results obtained, it is interesting to note that all types of buildings whether with soft story or with typical story height show the same acceleration trend and close values (except top floor) for all types of isolation systems and earthquakes considered. In addition, both 3 and 8-story buildings suffered increase in interstory drifts beyond the limits defined UBC 97 under earthquakes containing long period pulses.

ARTICLE INFO

Article history:
Received 10 November 2016
Accepted 23 December 2016

Keywords:
Soft-story
Seismic response
Seismic isolation
Near and far-fault earthquakes

1. Introduction

A soft story known as weak story can be defined as a story in a building that has open parking or commercial space and substantially less resistance or stiffness or inadequate ductility (energy absorption capacity) than the stories above or below it (Hejazil et al., 2016). In such buildings, the dynamic ductility demand during probable earthquake gets intense in the soft stories and the upper stories tend to remain elastic, and thus the whole building down with them (Setia and Sharma, 2012). Many studies have been conducted on the dynamic behaviour and seismic vulnerability of reinforced concrete structures with soft stories (Alekar et al., 1997; Kanitkar and Kanitkar, 2004; Lee and Ko, 2007; Mastrandrea and Piluso, 2009).

It has been observed from previous research (Pinarbasi and Konstantinidis, 2007; Ribakov, 2010; Komur, 2016) that a popular earthquake resistant design concept is the use of base-isolation devices that are placed between the superstructure and the substructure. The base isolation possess high lateral flexibility and high axial rigidity, reduces substantially the absorption of the earthquake's energy by the superstructure and shift the fundamental period of the structure toward higher values (Berton et al., 2008). Although base isolation reduces the possibility of damage (less inter-story drifts, shear forces and floor accelerations) of a building, it causes to large displacements in the structure relative to the ground. This, in turn, increases the potential of impact or pounding of a building with adjacent structures (Pant and Wijeyewickrema, 2012).

* *Corresponding author*. Tel.: +90-212-4737070 ; Fax: +90-212-4737180 ; E-mail address: savas.erdem@istanbul.edu.tr (S. Erdem)
ISSN: 2149-8024 / DOI: http://dx.doi.org/10.20528/cjsmec.2016.12.038

One of the important factor that affects evaluation of the seismic performance of a building is the type of earthquake ground motion. Compared to far-fault (FF) ground records, near fault (NF) ground motions often possess distinct characteristics such as producing high input energy at the beginning of the earthquake and have strong influences on the structural dynamic response, especially for long-period structures. In addition, for structures subjected to NF ground motions, the isolator displacements tend to be considerable while the isolators experience acceptable deformations under FF ground motions (Providakis, 2008; Bayraktar et al., 2009; Li et al., 2016). In the literature review, a number of research studies have been performed for investigating the influence of concrete strength on the structural performance. A recent work by Tavakoli et al. (2015) demonstrated the NF motion induces noticeable base shear so that reduction in base shear values was very low after utilizing lead-rubber isolating bearing in high-rise and intermediate structure models in comparison with FF motion. In another study, Chopra and Chintanapakdee (2001) compared certain aspect of the response of single degree freedom systems to NF ground motions with their response to FF ground motions in the context of the acceleration, velocity and displacement sensitive regions of the response spectrum. It was found that for the same ductility factor, NF ground motions impose a larger strength demand in their acceleration-sensitive region compared to FF motions.

A review of the literature indicates that in contrast to seismic behaviour of seismically isolated reinforced concrete buildings, no study has been conducted so far to investigate the effect of soft story on the seismic response of a seismically isolated building under near and far fault earthquakes. In this study, three story and eight story isolated buildings with 1st story height of 3m and 2nd with 1st story height of 4.5m were employed to capture soft story effect on the seismic response of seismically isolated buildings under near and far fault earthquakes. Analyses were conducted by using two different isolation systems (QW7.5Tb3 and QW7.5Tb4) and the four accelerations records. Floor accelerations, story shears and inter-story drift ratios were the key structural responses considered.

2. Methodology

In this study, the effects of soft-story on the behaviour of 3-story and 8-story isolated buildings under near and far-fault earthquakes were investigated. The superstructure and isolation system were designed according to TEC 2007 and UBC 97, respectively.

2.1. Design of the superstructures

3-story and 8-story isolated buildings with 5 bays in each orthogonal direction have been used in this study. These structures are intended to represent typical residential low-rise and high-rise reinforced concrete buildings in urban areas. Two different 1st story height was used: One with 1st story height of 3m and 2nd with 1st story height of 4.5m to capture soft story effect. The buildings are symmetrical about both principal axes and have typical column-beam sections without any shear walls. Typical plan of 3 and 8-story buildings, and 3D views of the buildings are shown in Fig. 1, Fig. 2 and Fig. 3, respectively. It was assumed that the building importance factor was 1, and that the soil type according to UBC 97 was Class C. Materials properties are assumed to be 30 MPa for the concrete compressive strength and 420 MPa for the yield strength of both longitudinal and transverse reinforcement. The height of the slabs is taken to be 14 cm.

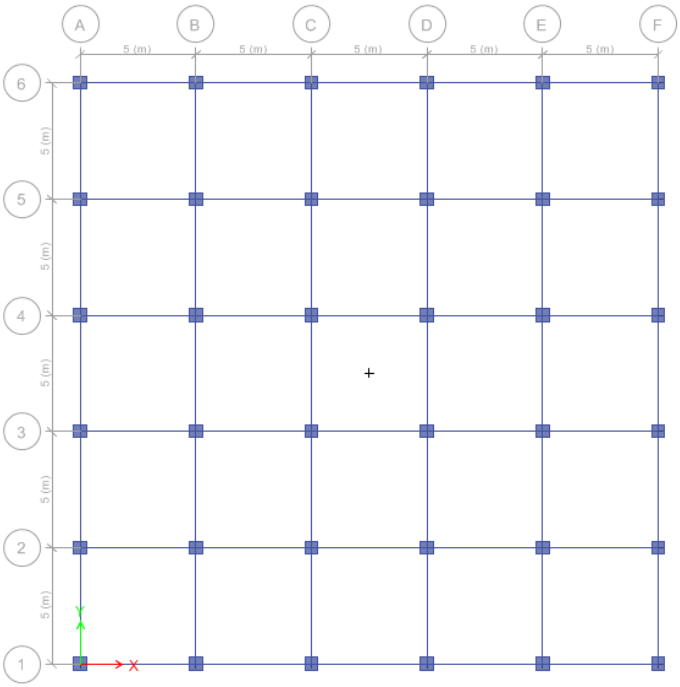

Fig. 1. Typical floor plan of 3 and 8-story buildings.

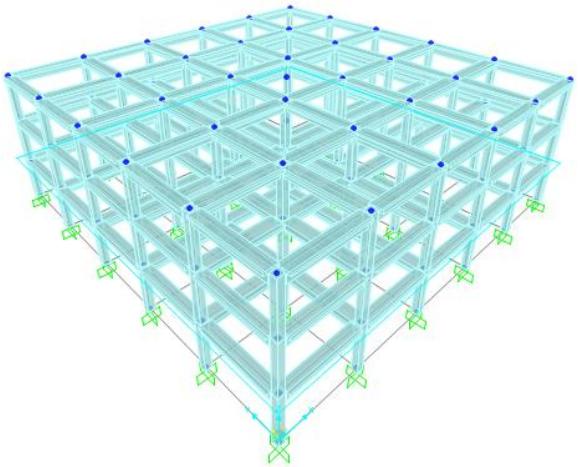

Fig. 2. 3D view of prototype 3-story building.

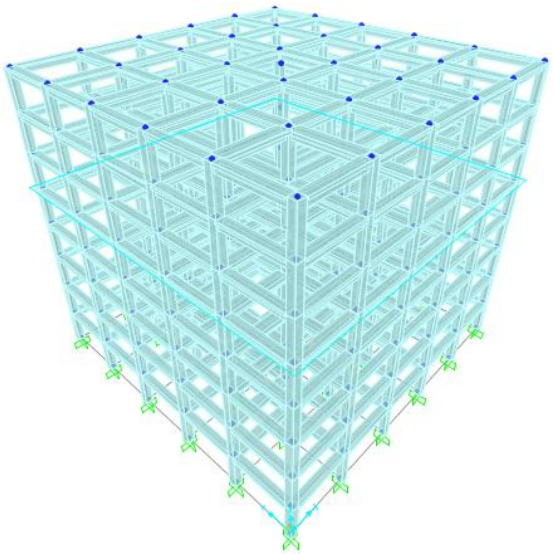

Fig. 3. 3D view of prototype 8-story building.

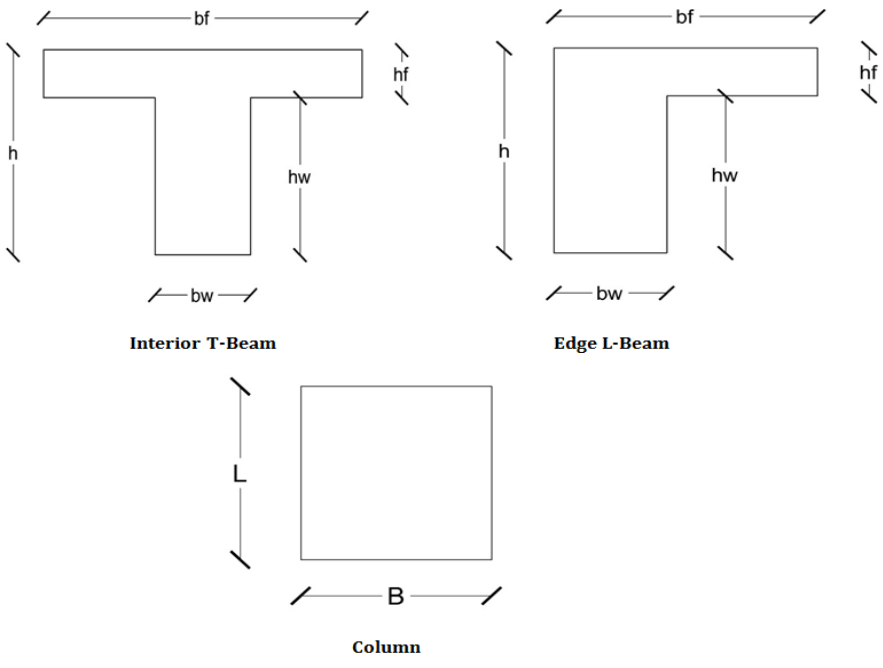

Fig. 4. Details of the frame section the buildings.

Regarding loading on the buildings, story masses were usually used which are lumped at centre of gravity (at master joint). Figure of frame sections of the buildings is shown Fig. 4. Details of the column and beam sections are also tabulated in Table 1. The prototype fixed base buildings were converted to seismically isolated buildings by introducing rubber isolators at base level (also called base isolation). A translational mass of 500 kNs^2/m was assumed to be lumped at the centre of mass of each floor.

Each floor had 3 degrees of freedom i.e. 2 translations and 1 rotation. Rigid diaphragm was introduced at each floor level to distribute the lateral forces to structural elements of the frame.

Table 1. Section size of the members.

X - section	Symbol	Dimensions for 3-story building (mm)	Dimensions for 8-story building (mm)
T - beam	h	600	600
	h_w	460	460
	b_w	300	300
	b_f	1000	1000
	h_f	140	140
L - Beam	h	600	600
	h_w	460	460
	b_w	300	300
	b_f	700	700
	h_f	140	140
Column	L	400	550
	B	400	550

2.2. Design of the isolation systems

Analyses were realized by using two different isolation systems (QW7.5Tb3 and QW7.5Tb4). Here, in QW7.5Tb3 isolation system QW7.5Tb4 indicates characteristic strength of isolation system normalized with weight of the building (W) to be 7.5% and T_{b3} indicates isolation period to be 3 seconds. It is worth-mentioning that characteristic strength of the isolation system is a measure of level of damping in the isolation system. The parameters concerning isolation systems were summarized in Table 2. To calculate parameters for each isolator, Q (characteristic strength), K_1 (pre-yield stiffness), K_2 (post-yield stiffness), and F_y (Yield force) should be divided by total number of isolators used in the isolation system. In Table 2, α is post-yield to pre-yield stiffness ratio and D_y is yield displacement of isolation system. A constant value of 0.015 m was adopted for both the isolation systems.

Table 2. Parameters related to modelling of nonlinear isolation system.

Super-structure	Isolation System	T_b (s)	Q (kN)	α	K_2 (kN/m)	K_1 (kN/m)	D_y (m)	F_y (kN)
3-story	QW7.5Tb3	3	1471.5	0.082	8772.982	106873.0	0.015	1603.09
	QW7.5Tb4	4	1471.5	0.048	4934.802	103034.8	0.015	1545.52
8-story	QW7.5Tb3	3	3310.875	0.082	19739.209	240464.2	0.015	3606.96
	QW7.5Tb4	4	3310.875	0.048	11103.305	231828.3	0.015	3477.42

2.3. Seismic ground motions

The modelling of conventional fixed base prototype seismically isolated buildings and their modal analyses were conducted on finite-element program SAP2000, whereas, modelling of seismically isolated buildings and nonlinear time-history analyses were conducted using 3D-BASIS program which has been particularly developed, by Nagarajaiah et al. (1991), for nonlinear dynamic analysis of three dimensional base isolated structures. The four accelerations records has been used for the time-history analysis. The properties of these acceleration records are shown in Table 3.

The fundamental/first mode periods of the buildings with different 1^{st} story heights were obtained through modal analyses and are presented in Table 4.

Analyses were done by using bidirectional earthquake input with strong component of earthquake along one main axis (X-axis) and weak component of earthquake along other orthogonal main axis (Y-axis) of the buildings. The scaled spectrum record for acceleration used in the analysis are shown in Fig. 5. It should not be forgotten that the spectrum shows the responses of a single degree freedom system. As the buildings were a multi degree of freedom system, the response will vary.

Table 3. Parameters related to modelling of nonlinear isolation system.

Historical earthquakes	Date of occurrence	Recording station	Magnitude	Strong component (g)	Weak component (g)
Duzce (Far-Fault)	12/11/1999	IRIGM 498	7.14	0.396	0.337
Landers (Far-Fault)	28/06/1992	Coolwater CLW	7.28	0.412	0.282
Northridge (Pulse-like Near-Fault)	17/01/1994	Rinaldi Receiving Station RRS	6.69	0.825	0.487
Tabas (Pulse-like Near-Fault)	16/09/1978	Tabas Tab	7.4	0.854	0.767

Table 4. Fundamental/First mode period of the buildings.

Building superstructure	Fixed-base natural period (s)
3-story with 1st story of height 3m	0.357
3-story with 1st story of height 4.5m	0.512
8-story with 1st story of height 3m	0.638
8-story with 1st story of height 4.5m	0.727

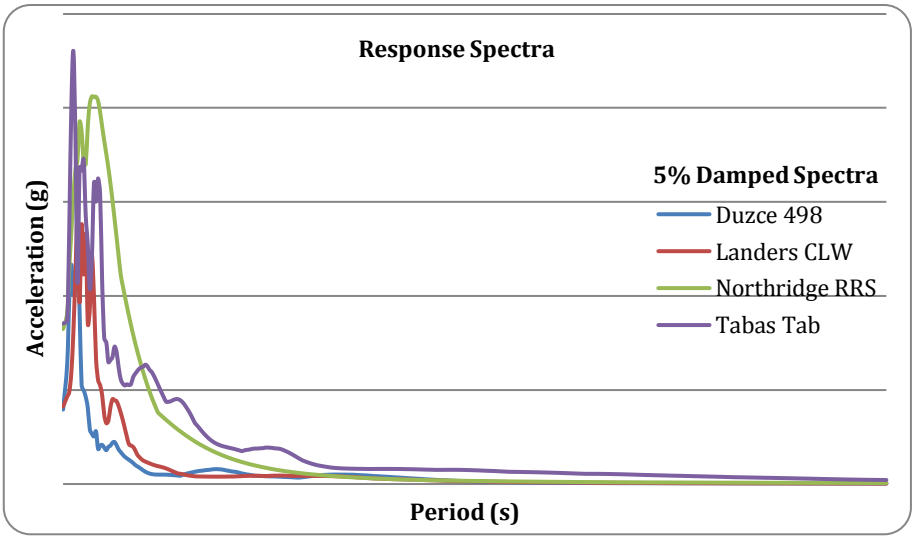

Fig. 5. The scaled record spectra used.

3. Results and Discussion

As the seismically isolated buildings in this study are subjected to bi-directional near and far-fault earthquake excitations, the structural responses in both global X and Y direction have been considered for performance comparison. It is important to mention that the building models used in this study are symmetrical so the results obtained would be same if the axes are reversed. Moreover, the displacements at the isolation level or the base displacements obtained from the analyses of all the building models with similar isolation parameters are almost same so the main focus of attention for this study is the superstructure responses. Floor accelerations, story shears and inter-story drift ratios are the key structural responses considered.

3.1. Floor accelerations

Considering FF earthquakes, for 3-story buildings with isolation system QW7.5Tb3, the accelerations are normally less at 1st floor for building with soft story as compared to building with typical story height at 1st floor (i.e. 3m). However, the accelerations are more at 2nd floor for soft story building (see Fig. 6). It is interesting to note that soft story building shows almost a linearly increasing pattern of accelerations towards top floor, while, the building with typical 1st story height shows about same acceleration at 1st and 2nd floor but accelerations increasing for 3rd floor (i.e. top floor). And, the accelerations at top floor level are generally less for building with typical 1st story than building with soft story at first floor. Under Northridge RRS pulse-like earthquake, floor acceleration increases towards top floor for both of the buildings i.e. building with 3m 1st floor and building with 4.5m 1st floor but the difference of floor accelerations between aforementioned buildings increases towards top floor with soft story building showing more acceleration at top floor level than the other. Tabas Tab NF earthquake bring about a slightly different response with floor acceleration almost same at 1st floor level for both type of buildings under consideration and the difference of floor accelerations between two buildings highest at 2nd floor level. Buildings with isolation system QW7.5Tb4 follow the same trend as described for buildings with isolation system QW7.5Tb3 but typically the floor accelerations are less for building with QW7.5Tb4, as compared to their QW7.5Tb3 counterparts, due to more flexibility at the isolation level.

The response in other orthogonal direction is a bit different as FF earthquakes show less increase in acceleration from 1st to 2nd floor for soft story building as compared to other principal direction X (Fig. 7). For NF earthquakes, the response is also slightly different for Y-direction as compared to X-direction. Nevertheless, this slight difference is not so significant.

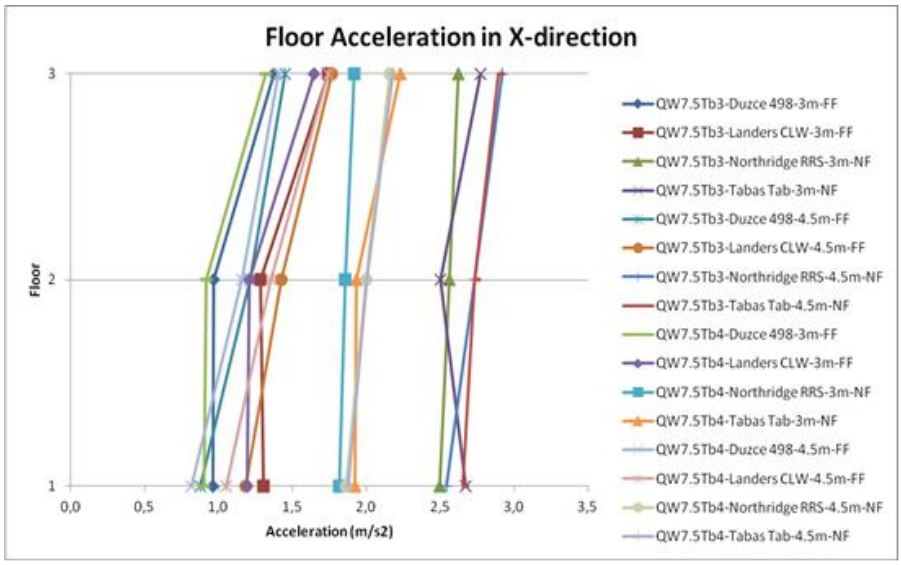

Fig. 6. Floor acceleration in X-direction for 3-story building.

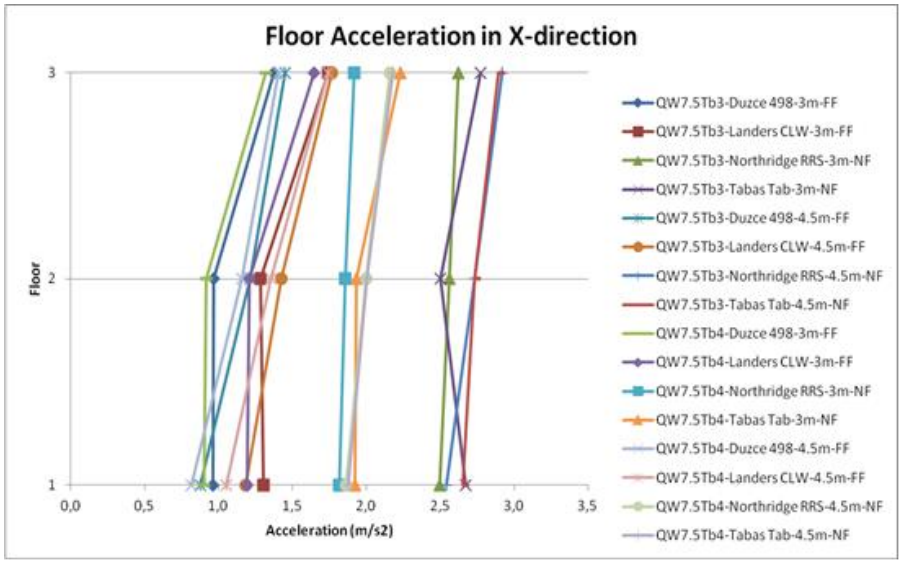

Fig. 7. Floor acceleration in Y-direction for 3-story building.

8-story seismically isolated buildings show different trend in comparison to 3-story building, as evident from Fig. 8. For all types of buildings, floor accelerations are generally more for lower floors with accelerations decreasing towards middle floor levels and then again increases towards top floor, thus, reaching the highest value at top floor level. The only exception to this behavior is Tabas Tab pulse-like earthquake which shows relatively complex floor acceleration trend (see Fig. 8). One important thing to be noticed here that all types of buildings whether with soft story or with typical story height show the same acceleration trend and close values (except top floor where a slight deviation is noted for some earthquakes), for all types of isolation systems and earthquakes considered.

The floor acceleration response in other orthogonal direction is essentially the same (Fig. 9). It can be concluded that 8-story buildings whether having 1st story of height 4.5m or 3m show different response as compared to corresponding 3-story buildings. As flexibility of superstructure increases, the acceleration trend changes and effect of soft story on floor accelerations becomes less distinct.

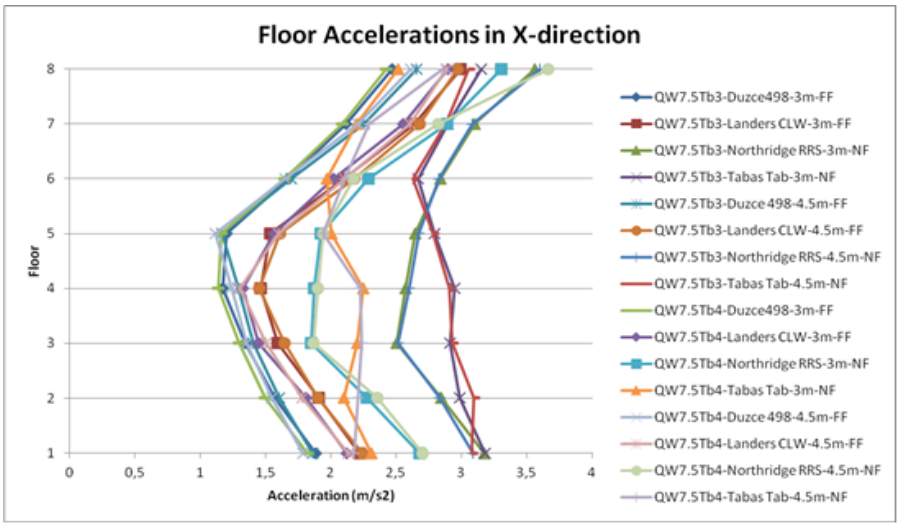

Fig. 8. Floor acceleration in X-direction for 8-story building.

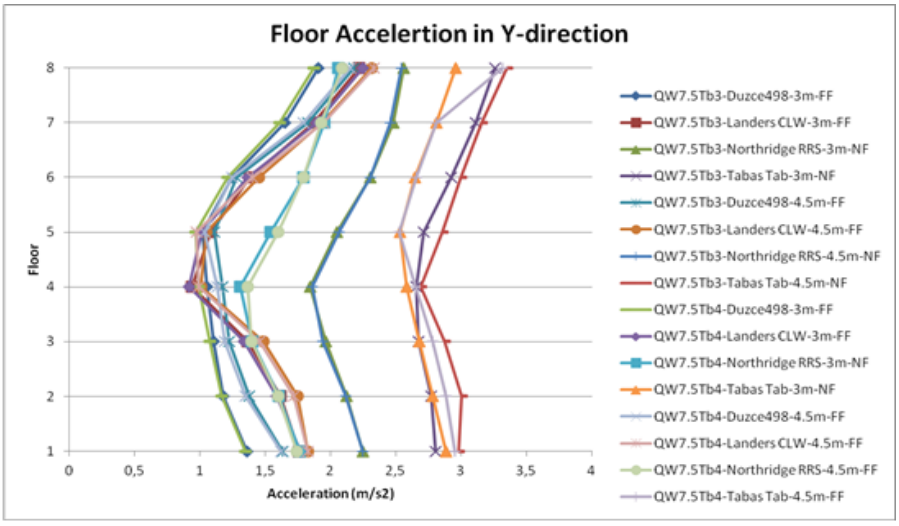

Fig. 9. Floor acceleration in Y-direction for 8-story building.

3.2. Story shears

In 3-story building, the story shear distribution trend is almost same for all earthquakes i.e. FF and NF earthquakes, in similar type of buildings. However, more story shears are observed at 1st and 2nd floor for buildings with soft story but the base shear and shear at top floors are almost same as building with typical 3m story height (see Fig. 10). For NF Earthquakes, comparing buildings with QW7.5Tb3 against the buildings with QW7.5Tb4 isolation system, the difference in story shears and base shears are quite large as compared to the same seismically isolated buildings subjected to FF earthquakes. Overall, for every type of building and earthquake, the shears are more for QW7.5Tb3 as compared to isolation system QW7.5Tb4 which may be down to its flexibility.

Same trend is observed for other orthogonal direction but difference in shears between building with 3m 1st story height and building with 4.5m 1st story height is very small (Fig. 11).

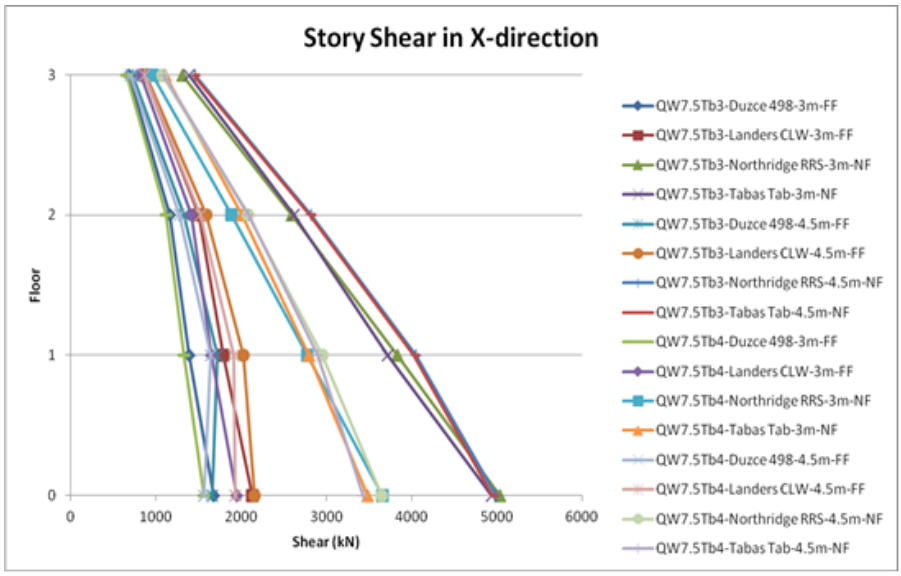

Fig. 10. Story shears in X-direction for 3-story building.

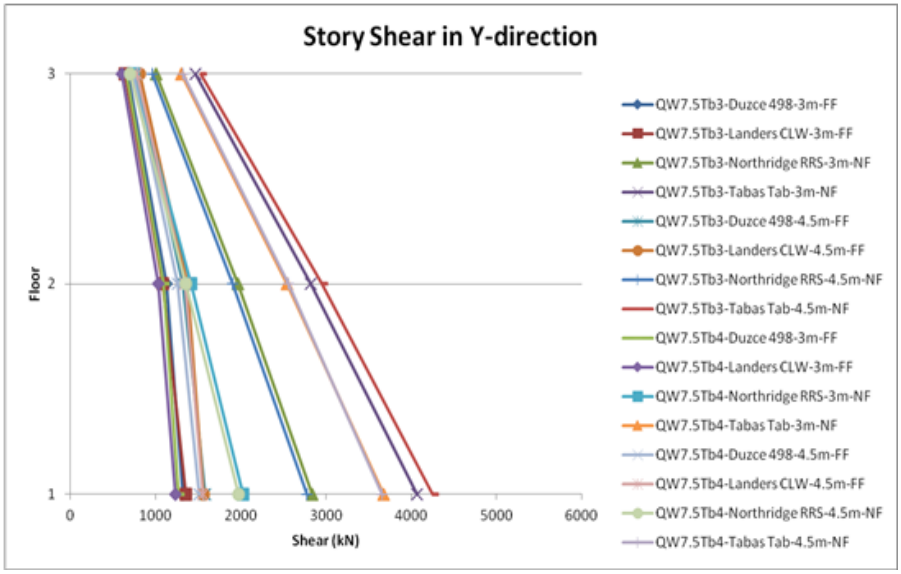

Fig. 11. Story shears in Y-direction for 3-story building.

For 8-story building, the story shears and base shears are more or less same for 3m 1st story building and 4.5m 1st story building. The shear distribution along the height is not as linear as in the case of 3-story buildings. The difference of story shears between all types of buildings becomes less apparent on upper floors with very close values of top floor shear for every type of building, isolation system and earthquake (Fig. 12). Likewise 3-story building, the difference of shears at each floor level, between buildings with QW7.5Tb3 and QW7.5Tb4 subjected to NF earthquakes, is quite large in lower and middle floors as compared to the situation if they are excited by FF earthquakes. Same trend is observed for other principal direction i.e. along Y-axis (Fig. 13).

3.3. Inter-story drift ratios

In 3-story seismically isolated building with isolation system QW7.5Tb3, for (FF) earthquakes i.e. Duzce 498 and Landers CLW, the inter-story drift ratios at each floor level are more for isolated building with 1st story of height 4.5m as compared to the building with 1st story of height 3m. The soft story at 1st floor induces an increase in inter-story drifts at floors above it but this difference decreases from the soft story towards the top floor with the lowest difference in inter-story drift ratios observed at top floor level. In the building with the same isolation system, under pulse like (NF) earthquakes i.e. Northridge RRS and Tabas Tab, overall the inter-story drift ratios are more as compared to that of FF earthquakes (Fig. 14). In this case, the soft story at 1st floor induces more increase in inter-story drift ratios at every floor level as compared to FF earthquakes but the trend observed is same i.e. decrease in difference of inter-story drift ratios towards top floor level.

As the isolation period is increased from 3s to 4s (QW7.5Tb4), an overall decrease of inter-story drift ratios at each floor level is observed as compared to

building with isolation system QW7.5Tb3 but the difference of inter-story drift ratios (between a building with 1st story of height 3m and a building with soft story effect 1st story of height 4.5m) remains essentially the same. The same decreasing trend of difference of inter-story drift ratio is observed from soft story towards top floor as was observed for QW7.5Tb3. Likewise QW7.5Tb3, Pulse-like NF earthquake induces more difference in inter-story drift ratios as compared to FF earthquakes (Fig. 14).

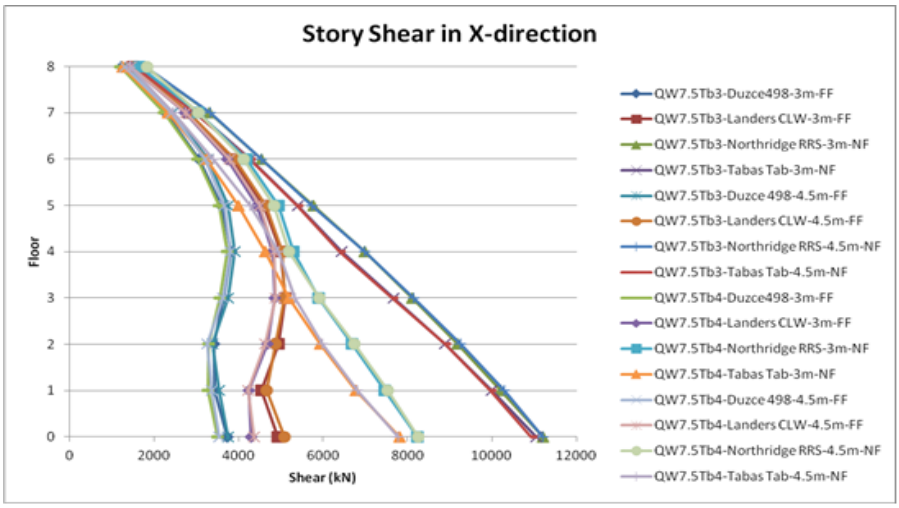

Fig. 12. Story shears in X-direction for 8-story building.

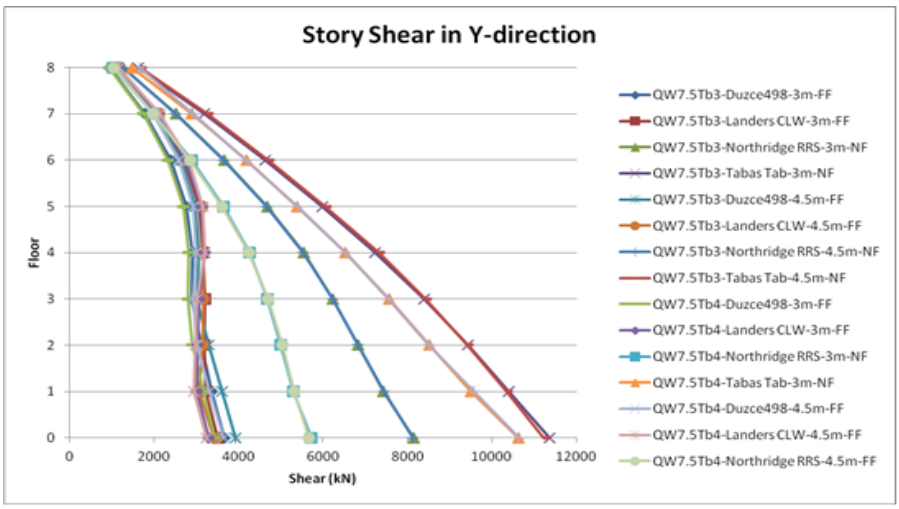

Fig. 13. Story shears in Y-direction for 8-story building.

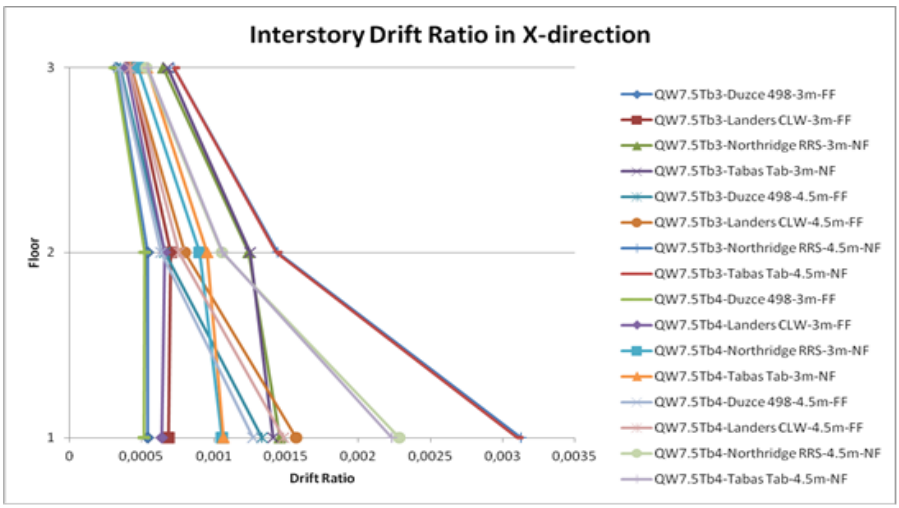

Fig. 14. Inter-story drifts in X-direction for 3-story building.

For 3-story building, in orthogonal Y-direction the inter-story drift ratios follow the same trend as observed in main orthogonal X-direction (Fig. 15). The only exception being the NF earthquake Northridge RRS where a sharp decrease, in difference between inter-story drifts of building with soft 1st story and normal 1st story, is observed from 2nd to 3rd floor for both isolation systems QW7.5Tb3 and QW7.5Tb4.

For 8-story buildings with isolation system QW7.5Tb3, under FF earthquakes i.e. Duzce 498 and Landers CLW, an increase in inter-story drift ratios is observed for building having soft 1st story (4.5m height) as compared to building with normal first story (3m height) with the greatest difference between inter-story drift ratios at 1st floor level but difference becomes very small from 3rd floor towards Top floor level (as evident in Fig. 16). For NF earthquakes Northridge RRS and Tabas Tab, inter-story drift ratios are greatest at 2nd floor level and decreases towards top floor with the least value of inter-story drift ratios seen at the top floor. The difference of inter-story drift ratios, between building with 1st story of height 3m and building with 1st story of height 4.5m, is greatest at 1st floor level but the difference becomes very small from 3rd floor onwards towards top floor level.

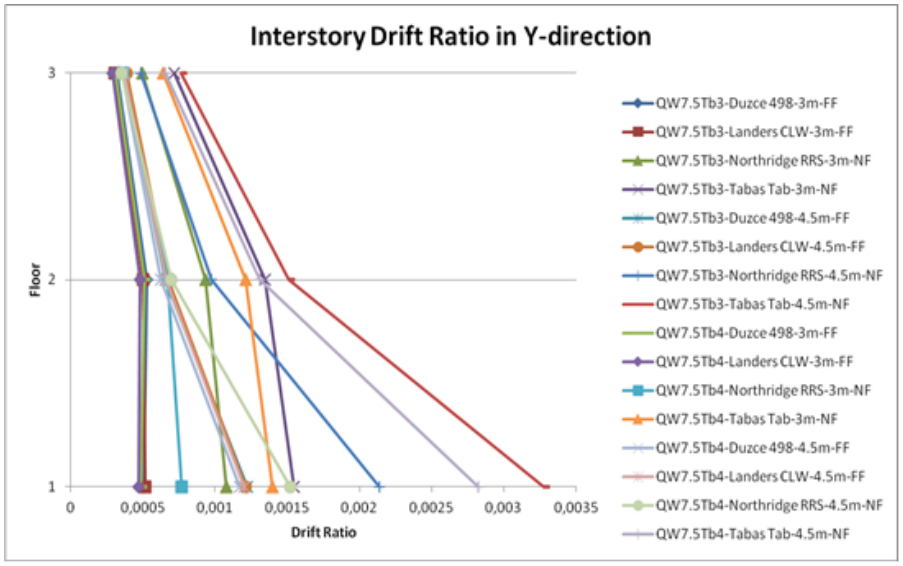

Fig. 15. Story shears in Y-direction for 3-story building.

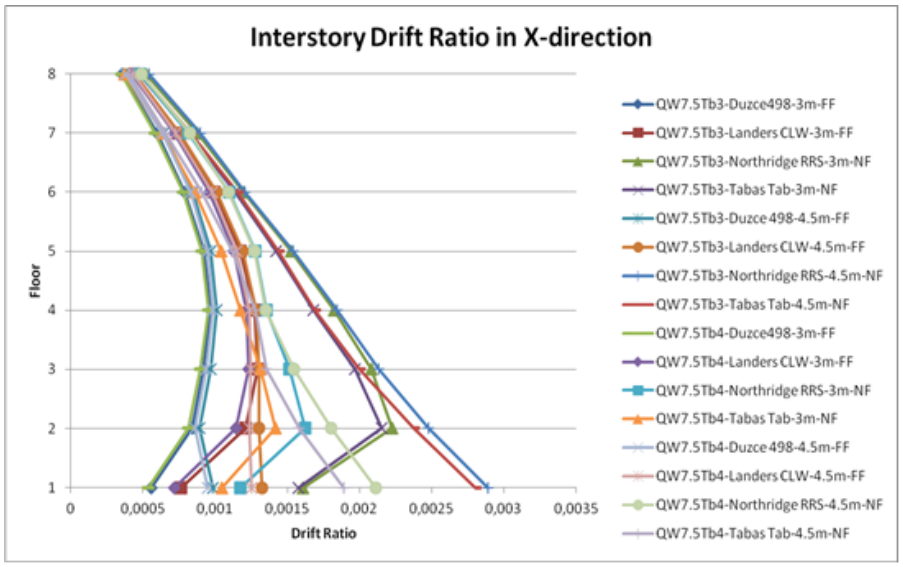

Fig. 16. Inter-story drifts in X-direction for 8-story building.

For the same buildings with isolation system QW7.5Tb4, under FF earthquakes, inter-story drift ratios are overall slightly less than that of building with isolation system QW7.5Tb3. Far-Fault earthquakes induce maximum inter-story drifts at 4th floor level for both QW7.5Tb3 and QW7.5Tb4, while, this value is greatest at 2nd floor level (see Fig. 16). For NF earthquakes, in the building with QW7.5Tb4, the difference of inter-story drifts between building with 3m 1st floor height and building with 4.5m height is highest at 1st floor level with the difference very small from 3rd floor onwards to top floor. An exception to that is Tabas Tab earthquake,

where the difference is less at 3rd floor followed by an increase and then decrease towards top floor with the least value of difference observed at top floor level. However, unlike FF earthquakes, for pulse-like earthquakes the difference in inter-story drift ratios at each floor level is quite large between QW7.5Tb3 building with 3m 1st story and QW7.5Tb4 building with 3m 1st story and same trend is observed for buildings with 1st story of 4.5m height. In comparison to 3-story buildings, generally the difference in inter-story drift ratios becomes very small after 3rd story towards 8th story (top level) so a decreasing trend is not so obvious. Similar results are seen on the other orthogonal direction i.e. along Y-axis of the buildings (as obvious from Fig. 17). It can be concluded that soft story influences the inter-story drifts of stories just above it and becomes less pronounced at upper floors.

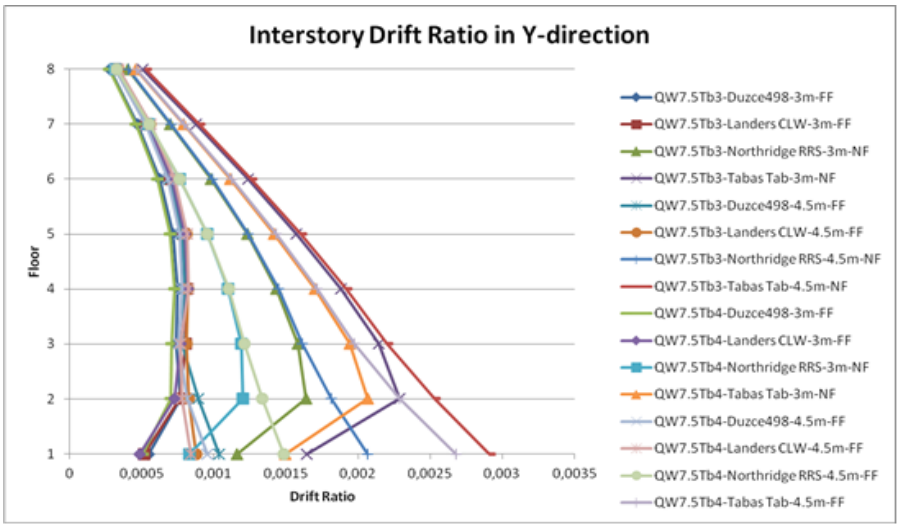

Fig. 17. Inter-story drifts in Y-direction for 8-story building.

In general for all the cases considered, max inter-story drift ratio limit, defined in UBC97, for seismically isolated building is $0.02/R_I$ (if calculated by time-history analysis). Where, R_I is 2 for concrete moment resisting frames. It is important to mention that both 3 and 8-story buildings suffered increase in inter-story drifts beyond this limit, under earthquakes containing long period pulses. Inter-story drifts beyond a certain level may be dangerous for the integrity of the building.

4. Conclusions

Sudden changes in lateral stiffness and strength is one of the most important factors on the structural response of seismically isolated buildings under near and far fault earthquakes.

In general, the results demonstrate that seismic isolations can be used as a viable mitigation method for the buildings with soft-stories under near and far-fault earthquakes. In addition, it can be concluded that soft story influences the inter-story drifts of stories just above it and becomes less pronounced at upper floors. However, both 3 and 8-story buildings suffered increase in inter-story drifts beyond the limits which is defined in UBC97, under earthquakes containing long period pulses. Thus, interstory drifts beyond a certain level may be dangerous for the integrity of the building.

In a future research study, the efficiency of hybrid isolation system with friction sliders and viscous damper for protection of seismically isolated buildings with soft story against near fault earthquakes would be studied.

References

Alekar JN, Jain S, Murty CVR (1997). Seismic response of RC frame buildings with soft first storeys. *Proceedings of Central Building Research Institute Golden Jubilee Year Conference on Natural Hazard in the Urban Habitat*, New Dehli, India, 13-24.

Bayraktar A, Altunisik AC, Sevim B, Kartal ME, Turker T, Bilici Y (2009). Comparison of near-and far-fault ground motion effect on the nonlinear response of dam-resorvoir-foundation systems. *Nonlinear Dynamics*, 58, 655-673.

Berton S, Bolander JE, Pasian A (2008). Bi-directional response of base isolated structures subjected to near-fault ground motions. *Proceedings of the 14th World Conference on Earthquake Engineering*, Beijing, China.

Chopra AK, Chintanapakdee C (2001). Comparing response of SDF systems to near-fault and far-fault earthquake motions in the context of spectral regions. *Earthquake Engineering and Structural Dynamics,* 30, 1769–1789.

Hejazi F, Jilani S, Noorzaei J, Chieng CY, Jaafar MS, Ali AAA (2011). Effect of soft story on structural response of high rise buildings. *IOP Conference Series: Material Science Engineering,* 17(1), 012034.

Kanitkar R, Kanitkar V (2004). Seismic performance of conventional multi-story building with open ground floors for vehicular parking. *The Indian Concrete Journal*, 78, 99-104.

Komur MA (2015). Soft-story effects on the behaviour of fixed base and LRB base-isolated reinforced concrete buildings. *Arabian Journal for Science and Engineering*, 41 (2), 381-391.

Lee HS, Ko DW (2007). Seismic response characteristics of high-rise RC wall buildings having different irregularities in lower stories. *Journal of Engineering Structures*, 29 (11), 3149– 3167.

Li S, Zhang F, Wang J, Alam MS, Zhang J (2016). Effects of near-fault motions and artifical pulse-type ground motions on super-span cable-stayed bridge systems. *Journal of Bridge Engineering*, (in press).

Mastrandrea L, Piluso V (2009). Plastic design of eccentrically braced frames, II: Failure mode control. *Journal of Constructional Steel Research*, 65 (5), 1015-1028.

Pant DR, Wijeyewickrema AC (2012). Structural performance of a base-isolated reinforced concrete building subjected to seismic pounding. *Earthquake Engineering and Structural Dynamics*, 1709-1716.

Pinarbasi S, Konstantinidis D (2007). Seismic isolation for soft storey buildings. *10th World Conference on Seismic Isolation, Energy Dissipation and Active Vibrations Control of Structures*, İstanbul, Turkey.

Providakis CP (2012). Effect of supplemental damping on LRB and FPS seismic isolators under near-fault ground motions. *Soil Dynamics and Earthquake Engineering*, 29(1), 80-90.

Ribakov Y (2010). Reduction of structural response to near fault earthquakes by seismic isolation columns and variable friction dampers. *Earthquake Engineering and Engineering Vibration*, 9(1), 113–122.

Setia S, Sharma V (2012). Seismic response of R.C.C building with soft storey. *International Journal of Applied Energy*, 7 (11), 1335-1339.

Tavakoli HR, Naghavi F, Goltabar AR (2014). Dynamic response of the base-fixed and isolated building frames under far- and near-fault earthquakes. *Arabian Journal for Science and Engineering*, 39(4), 2573-2585.

Challenge Journal of Structural Mechanics

Short Communication

Thermoelastic stress analysis for detecting wrinkles and associated resin pockets in polymer composites

Rani Elhajjar [a,*], Rami Haj-Ali [b]

[a] *Department of Civil & Environmental Engineering, University of Wisconsin Milwaukee, Milwaukee, WI 53201-0784, USA*
[b] *School of Mechanical Engineering, Tel-Aviv University, Ramat-Aviv 6997801, Israel*

ABSTRACT

A thermos elastic stress analysis method is proposed consisting of an array of infrared measurement sensors used for evaluation the wrinkling defects and associated resin pockets in a fiber reinforced polymer (FRP) composite structure. Wrinkling or fiber waviness defects results when out of plane distortions occur in some or all of the composite layers of the laminate. The wrinkles result in significant reductions of mechanical properties in the composite structure. The method involves instrumentation and device for application of internal energy in the material such as transient or cyclic mechanical excitations. These external excitations are induced in a prescribed or measurable cyclic or transient function of time. Infrared measurements from the surface of the composite are synchronized with the applied excitation energy. The results are used to provide for a map detailing the inner wrinkle defects and associated resin pockets in the laminated composite structure.

ARTICLE INFO

Article history:
Received 24 August 2016
Accepted 1 November 2016

Keywords:
Thermoelasticity
Experimental stress analysis
Effects of defects
Composites

1. Introduction

Advances in the mass manufacturing of composites have made it possible to consider composites as a viable construction material for large structural components and assemblies. Recent examples include the composite fuselage and wing sections of the 787 Dreamliner or the Airbus A350, which will be the first Airbus aircraft with the fuselage and wing structures, made primarily of carbon fiber-reinforced composites. The challenge in manufacturing large composite structures results in the near impossibility to achieve parts with no manufacturing defects.

Fiber waviness is considered one of the most common types of defects that reduce the load carrying capability in composite structures (El-Hajjar and Petersen, 2011). Pre-cure and post-cure optical and ultrasonic techniques have been proposed for characterization with limited success. Ultrasonic methods are not reliable for detection of wrinkles due to the reliance on reflection and attenuation mechanisms that are not always significantly evident in the presence of the wrinkle defect. The waviness is not usually associated with impedance changes as compared with porosity which is more readily identified with the ultrasonic methods due to the large differences in impedance values between the resin, fibers and air voids. Industrial computed tomography scanners can be used to image internal flaws in composite structures but these currently have severe object size limitations.

In this study, we investigate the use of the thermos elastic stress analysis (TSA) approach (Rauch and Rowlands, 1993) for characterization of wrinkle defects in composite structures. In the TSA method, during cyclic loading and the presence of reversible adiabatic conditions, an infrared detector measures an un-calibrated TSA signal that can be correlated to the stress levels in the materials. Composite specimens are fabricated using a quasi-isotropic layup consisting of 32 plies of IM7 carbon fiber/epoxy prepreg and having waviness defects across the specimen width and at multiple locations. Specimens were tested at 5Hz at stress levels well below the failure stress of the material as damage initiation and propagation were not the focus of this study. The applied tensile stresses were maintained under 27 MPa to ensure the specimens remain in elastic range.

* *Corresponding author*. Tel.: +1-414-229-3647 ; Fax: +1-414-229-6958 ; E-mail address: elhajjar@uwm.edu (R. Elhajjar)
ISSN: 2149-8024 / DOI: http://dx.doi.org/10.20528/cjsmec.2016.11.025

2. Results

The contours produced from the TSA were analyzed and compared to the control specimens. Fig. 1 shows the TSA contours observed on the face of the specimen for the different waviness profiles under a mean tension stress (Elhajjar et al., 2014). Note that the observations were made on the side that is usually available for non-destructive evaluation. In these experiments, the width of the specimen is the field of view of the infrared camera. The results show a clear spike in the TSA signal near the waviness zones in all locations tested corresponding to the severity of the defect.

Compared to the control specimens, there was a clear incidence in the thermal emissions in the vicinity of the waviness zone. It is believed that the resin rich zone in the waviness profiles is responsible for the clear signatures identifying the waviness profile due to the thermos elastic constant differences between the resin rich areas and the other areas of the structure. While the method provides only indications from the resin pocket, assumptions on the underlying defect can be made. For example, a conservative assumption that all layers below the surface have the same aspect ratio as the resin pocket is one way to handle the subsurface anomaly.

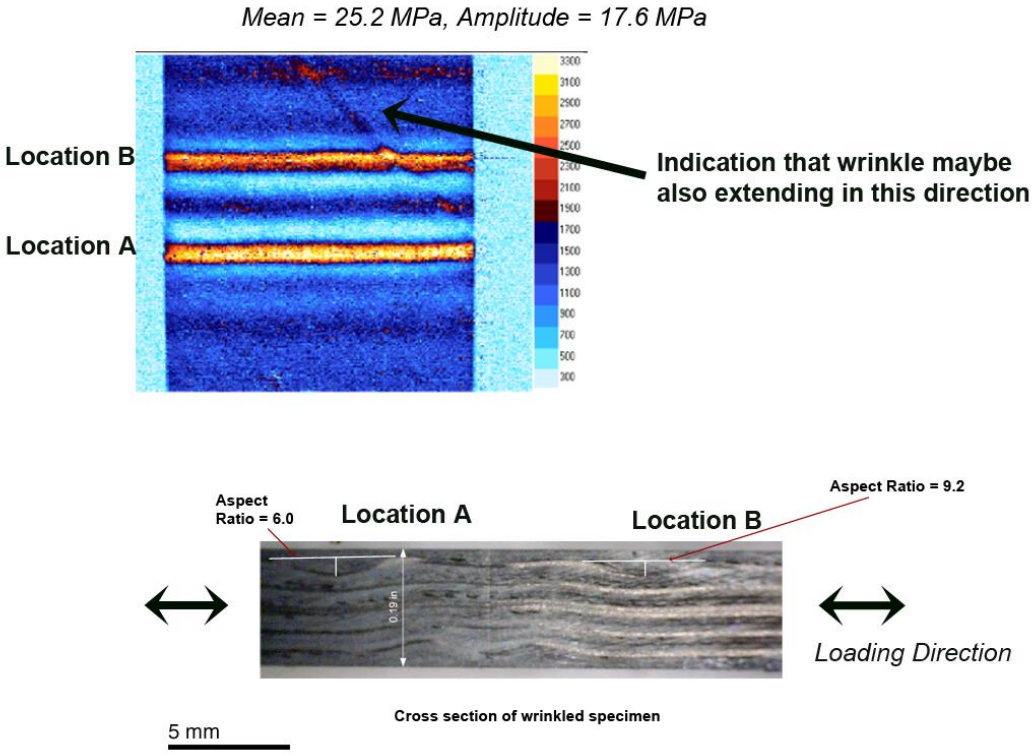

Fig. 1. TSA response on the surface of the specimen with respective cross-section.

3. Conclusions

The TSA approach proposed is linked to the excitation energy or stress state in the material. The TSA approach can provide indicators of structural integrity when wrinkle defects are involved. It does not require application of infrared radiation rather the system relies on relating the emitted IR to the structure's strain energy response under cyclic loading. Our demonstrations show that the present system is able to detect sub surface wrinkle and associated resin pockets. The system is capable of detecting wrinkles and associated resin pockets to an accuracy of the L/D ratio of less than 20 where L/D is the aspect ratio, defined as the length to depth ratio of the wrinkle wave. This range covers most wrinkles and associated resin pockets known to cause a degradation of load carrying capacity in composite structures.

References

El-Hajjar RF, Petersen DR (2011). Gaussian function characterization of unnotched tension behavior in a carbon/epoxy composite containing localized fiber waviness. *Composite Structures*, 93(9), 2400-2408.

Elhajjar R, Haj-Ali R, Wei B (2014). An infrared thermoelastic stress analysis ınvestigation for detecting fiber waviness in composite structures. *Polymer-Plastics Technology and Engineering*, 53, 1251–1258.

Rauch BJ, Rowlands RE (1993). Thermoelastic Stress Analysis in Handbook on Experimental Mechanics. Kobayashi AS, ed., SEM.